Doctoral Dissertation

Electrochemical Oxidation of Ascorbic Acid by Hierarchical Catalysts

Md Mahmudul HASAN

Supervisor: Dr. Yuki NAGAO

Graduate School of Advanced Science and Technology

Japan Advanced Institute of Science and Technology

[Doctor of Science (Materials Science)]

March 2022

General Abstract

The research is mainly focused on the preparation of metal catalysts having hierarchical structures for ascorbic acid (AA) oxidation. I have synthesized non-Pt-based electrocatalysts. The improvement in the AA electrooxidation leads to the construct of a direct alkaline AA-based liquid fuel cell (DAAFC) system. The DAAFC can solve two problems at a time. I could reuse waste materials (citrus fruits and Vitamin C contains vegetables) to extract AA and generate clean electricity from it. The DAAFC does not release any toxic chemicals or gases. So DAAFC system could help us in achieving sustainable development goals. In this study, I have explored potential anode catalysts for the improvement of AA electrooxidation. I have also constructed a DAAFC system to generate electricity.

I have developed unique hierarchical metal catalysts to improve AA electrooxidation. The well-growth Ag dendrite structures are prepared by a simple electroless deposition technique and applied for AA electrooxidation for the first time. The Ag catalyst is applied for the kinetic study of the AA electrooxidation because the Ag could prevent the electrode fouling during AA electrooxidation. The kinetic study helped us to understand the two electrons transfer process during AA electrooxidation. To improve the performance of the AA electrooxidation I have applied Pd-based catalysts.

A controlled electrodeposition technique is further developed for the preparation of unique Christmas-tree-shaped Pd nanostructures. The many sharp edges of these nanostructures provide more active sites for electrocatalysis. The unique Christmas-tree-shaped Pd nanostructures are applied for the AA electrooxidation in the alkaline condition. The AA electrooxidation is enhanced by these unique structures of Pd metal. The greater improvement in the AA oxidation leads us to choose Pd-based anode catalysts for DAAFC.

For the practical use of Pd-based catalyst for the DAAFC system, I have further developed Pd nanoparticles incorporating reduced graphene oxide (rGO) and multiwall carbon nanotube (MWCNT) composite by the chemical reduction process. The Pd/rGO/MWCNT catalyst showed excellent AA electrooxidation in the alkaline condition. Next, I have constructed the DAAFC system by using Pd/rGO/MWCNT catalyst. The maximum power output is 9.5 mW/cm^2 at 60 °C. The DAAFC result enlightens us about the use of AA as a fuel to generate clean energy in near future.

Keywords: Hierarchical structures, Ascorbic acid, Ag dendrite, Christmas-tree-shaped Pd nanostructure, rGO, MWCNT, Alkaline fuel cell.

Table of Contents

Page

List of Figures

List of Tables

Table Page

List of Scheme

List of Abbreviations

AA	Ascorbic acid
DHA	Dehydroascorbic acid
GCE	Glassy carbon electrode
rGO	Reduced graphene oxide

MWCNT	Multi-wall carbon nanotubes
NPs	Nanoparticles
I_p	Peak current
CV	Cyclic voltammetry
EIS	Electrochemical impedance spectroscopy
AFC	Alkaline Fuel Cell
AEM	Abion exchange membrane
DLFCs	Direct liquid fuel cells
DAAFC	Direct alkaline Ascorbic Acid fuels cell
FE-SEM	Field-emission scanning electron microscopy
EDX	Energy-dispersive x-ray spectroscopy
XPS	X-ray photoelectron spectroscopy
XRD	X-ray diffractometer
TEM	Transmission electron microscopy
BET	Brunauer−Emmett−Teller
OCV	Open circuit voltage

Chapter 1

General Introduction

1.1 Introduction to Ascorbic Acid

Ascorbic acid (AA), often known as Vitamin C, is a water-soluble vitamin and strong antioxidant found in a wide range of biological systems and foods [1–8]. The chemical formula and molar mass of AA are $C_6H_8O_6$ and 176.14 grams per mol, respectively [9]. The L-enantiomer of ascorbate is vitamin C or AA; the opposite D-enantiomer has no physiological significance. Both forms of the same chemical structure are mirror images of each other. The chemical structure of AA is shown in Figure 1.1. AA has been one of the omnipresent vitamins ever discovered. It cannot be produced by the human body and need to be intake from outside fruits and vegetables [10]. In citrus fruits and vegetables such as lemon, orange, lime, pomelo, tomatoes, black currant, leafy vegetables, green and red peppers, AA is substantially contained [10–16]. In numerous biological processes such as iron adsorption, amino acid metabolism, wound healing, osteogenesis, maintenance of capillaries, bones, and teeth, AA has a direct influence [10,17]. Furthermore, because of its antioxidant characteristics, AA is widely utilized in the

chemical industry, as well as in medical and cosmetic applications [8]. The oxidation of AA releases two electrons and two protons to form dehydroascorbic acid (DHA).

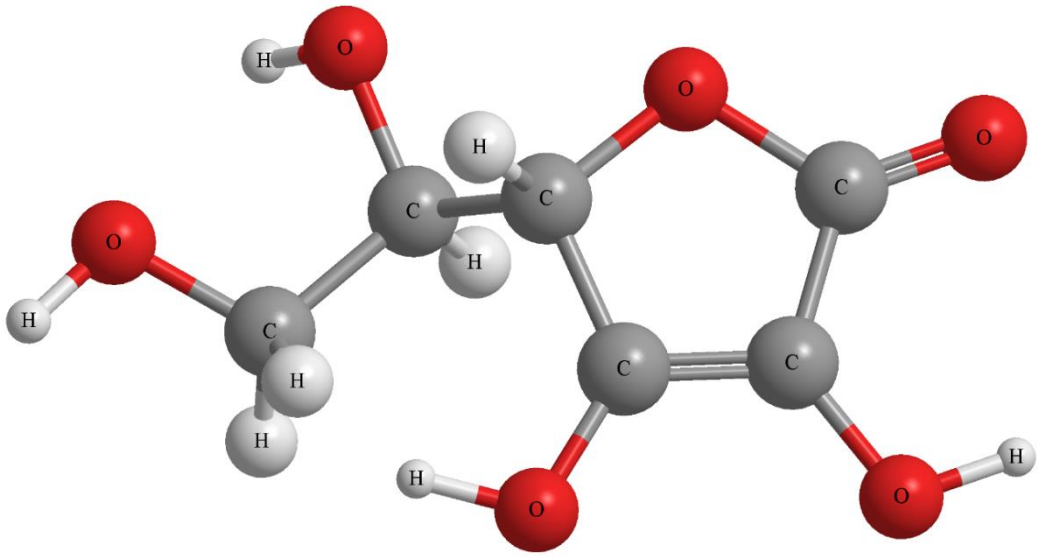

Figure 1.1 Chemical structure of ascorbic acid.

1.1.1 Mechanism of Ascorbic Acid Electrooxidation

The mechanism and kinetics of the electrochemical oxidation of AA on various metallic electrodes have been investigated extensively during the last few decades [18–23]. AA forms with DHA an irreversible redox couple [10] as shown in Figure 1.2.

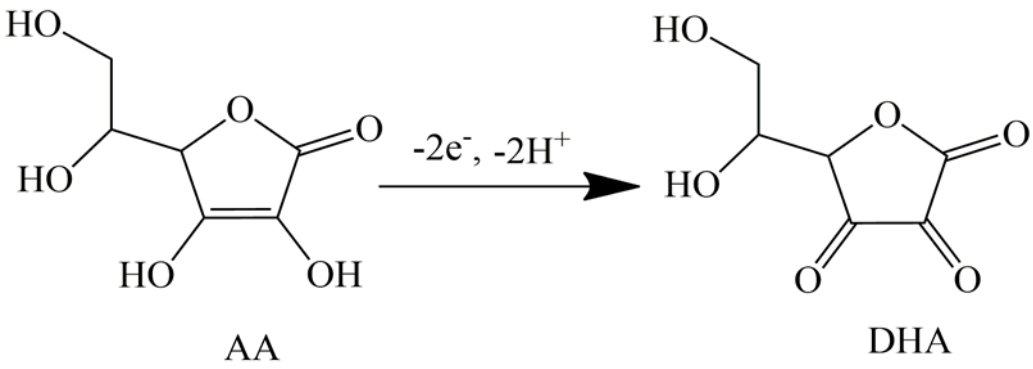

Figure 1.2 Ascorbic acid oxidation to produce dehydroascorbic acid.

Only the anodic oxidation peak is visible during AA electrocatalytic oxidation [10,20,24]. It has been demonstrated that the oxidation wave corresponds to the transfer of two electrons and two protons to produce DHA [21,25]. Figure 1.3 illustrates the reaction mechanism of electrooxidation of AA in acid or neutral solution at Pt, Au, and Hg electrodes [19,21]. This mechanism includes the predissociation of a proton to produce the monoanionic species, followed by the monoanionic species being oxidized by 1 e^-, 1 H^+ to form the radical anion. This radical anion undergoes a second 1 e^- oxidation to DHA.

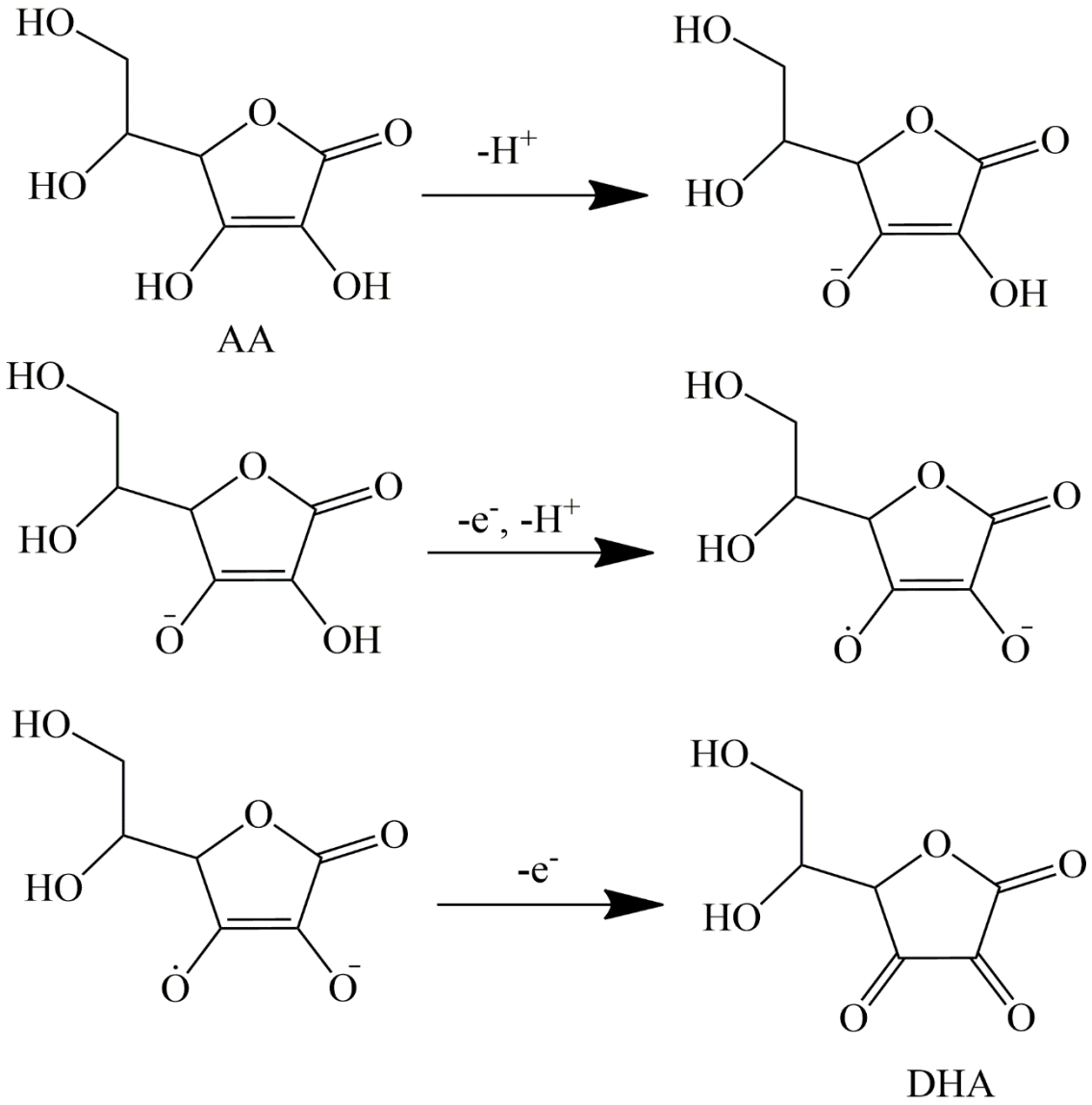

Figure 1.3 Reaction mechanism for the electrooxidation of ascorbic acid.

1.2 Catalysts for Ascorbic Acid Electrooxidation

The progress of nanomaterial technology over the last several decades has resulted in increasing research output in a wide range of application sectors. The use of nanomaterials in electrocatalyst technologies resulted in improved catalysis performance,

including increased sensitivity, selectivity, stability, and repeatability. When compared to other nanoscale systems, the noble metals have superior catalytic activity and biocompatibility, as well as being more stable at ambient temperatures. The development of new catalysis materials for energy-related applications allows for total catalyst miniaturization, increased specificity, storage, and operational stability. Noble metals have already been shown to be an attractive substrate for a variety of applications, including electrocatalysis, environmental monitoring, and biosensing. A variety of nanomaterials including noble metals/metal nanoparticles, transition metals/their oxides and hydroxides, conducting polymers, and carbon nanocomposites have been used for the electrocatalysis of AA [26]. Several noble metal-modified electrodes have been used with a reduced overpotential and excellent specificity for electrocatalysis of AA [23,27–31]. This is because noble metal modified electrochemical interfaces provide a larger electrochemically active surface area, accelerate the electron transfer rate, result in the rapid current response, and reduce the overpotential required for electrochemical reactions. Pt, in particular, has sparked increased attention due to its ability to allow rapid electron transfer while also providing better mass transport properties [4,32,33]. For the electrocatalysis of AA, nanostructured Pt-modified electrodes have been successfully applied [34,35]. The Nanostructured Pt contains a lot of sites for hydrogen adsorption,

AA oxidation, and reversing adsorption or dissociative side-chain adsorption. Due to biocompatibility, high surface-to-volume ratio, electron-rich core, limited range of sizes, and many surface functions, Au has often been widely used in electrocatalysis [36,37]. Several research has reported about the use of Au modified electrode for AA electrooxidation [2,10,29,38–42]. In comparison to other noble metal catalysts, recently Pd-based catalysts have been investigated in electrocatalysis, owing to their high catalytic activity and higher abundance [26]. For AA electrooxidation, several Pd-based catalysts have been reported [2,10,15,18,42–46]. Recently, Ag-based catalysts have been used to investigate the electrooxidation of the AA, due to distinctive electrical, and chemical properties [3,8,18,47–51].

1.2.1 Hierarchical-structured Metal Catalysts

Controlling the form of noble metal nanoparticles has been a significant focus of recent study since it provides another way to tune their physical and chemical characteristics [52]. From one-dimensional nanorods/nanowires to branching nanostructures, and from scattered triangular nanoplates to ordered assemblies with anisotropic orientation, the hierarchical assembly of nanoscale building blocks may be interpreted as ordered superstructures or complex architectures. The superstructure/hierarchical assembly can

show new and collective physical and chemical characteristics that cannot be found at individual nanoparticle levels [53,54]. The success of Bottom-up methods to integrated and functioning nano systems is essential to hierarchical assembly. One example of the hierarchical structure of Pd metal is shown in Figure 1.4. The Pd rod structures exhibited high catalytic performance for methanol electrooxidation [55]. The hierarchical structures provide more active surface sites, which are especially important for the high electrochemically active and stable catalyst development. Several reports have already been published based on different metal-based hierarchical structured like Ag [18], Pt [33], Pd [44,56] for AA electrooxidation. These studies showed a potential way of stable and excellent catalyst preparation for AA electrooxidation.

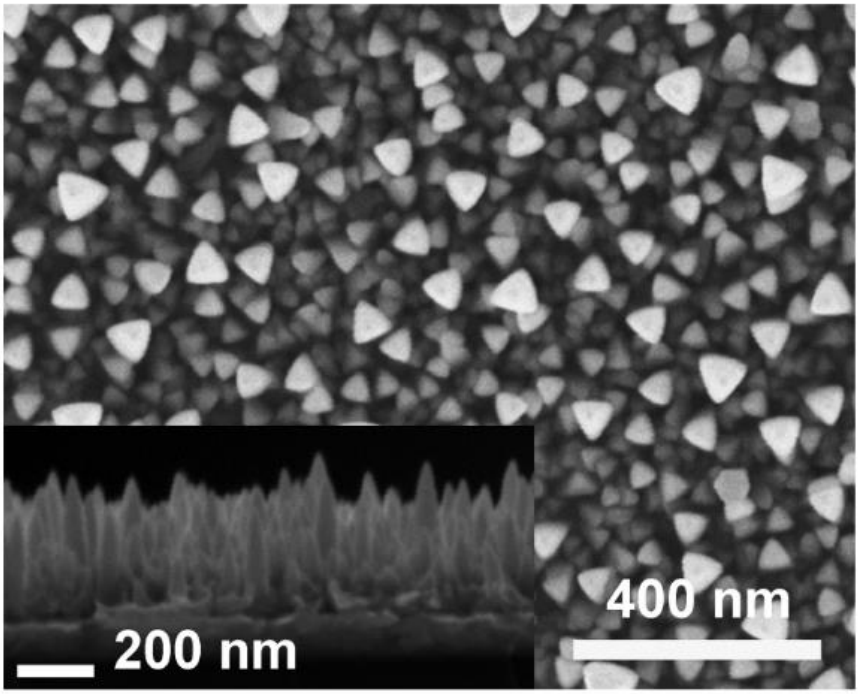

Figure 1.4 SEM picture of Pd triangular rod formations electrodeposited at -0.1 V with a total deposition charge of 0.02 C from 15 mM K_2PdCl_4 + 0.1 M H_2SO_4. A cross sectional SEM picture is shown in the inset [55].

Carbon materials are one of the most widely utilized active materials in electrochemical applications due to their excellent architectures, scalable manufacturing, and remarkable characteristics [57,58]. Single/multiwall carbon nanotubes (SWCNT/MWCNT), carbon nanodots, carbon nanohorns, carbon nanofibers, graphene derivatives, and nitrogen-doped carbon materials have been utilized as electrode materials for various electrocatalytic applications [59]. In addition, considerable effort has been made to promote the prospective uses of carbon nanomaterials and related

composites/hybrids in a variety of applications [60,61]. Carbon nanotubes (CNT) are ideal electrode materials because of their large surface area, high electrical conductivity, high mechanical resistance, changeable surface chemistry, and chemical inertness in most electrolytes [62,63]. The electrocatalysis of AA is successfully carried out using a variety of carbon nanostructures. A carbon paste electrode (CPE) is modified for AA electrooxidation utilizing MWCNT, ionic liquid (IL), and Pd nanoparticles [64]. Due to the increased electroactive surface area and the high conductivity of MWCNT, the modified PdNP/IL-MWCNT electrode exhibited a superior catalytic activity than the CPE and PdNP/CPE. The MWCNT has been used widely for electrocatalysis of AA [30]. Reduced graphene oxide (rGO), another form of carbon, has been used for the electrocatalysis of AA [46]. The rGO is a suitable 2D carbon material having good conductivity and high stability for electrolytes. Figure 1.5 showed the chemical structure of MWCNT and rGO.

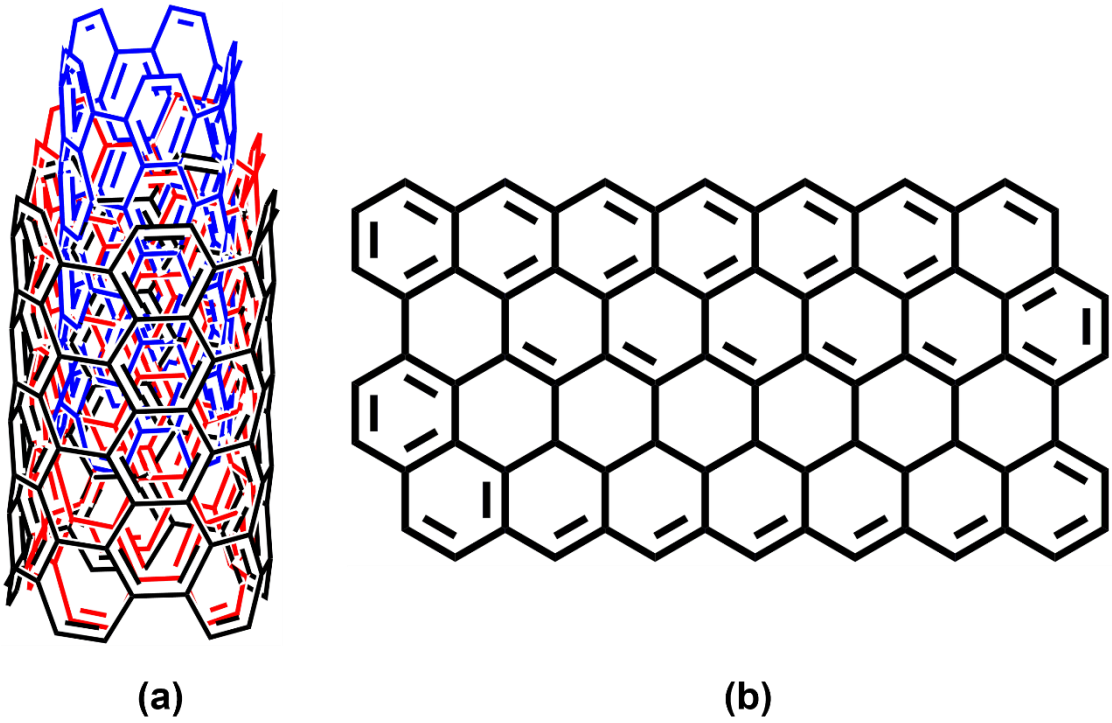

Figure 1.5 Chemical structure of (a) multiwall carbon nanotubes, (b) reduced graphene oxide.

1.3 Preparation Techniques for Metal Nanostructured Catalysts

Researchers have found several novel techniques for producing metal nanostructured catalysts having the optimum size, shape, and composition. Some of the ways for synthesizing the metal nanostructured are:

1.3.1 Thermal and photochemical degradation

In this method, precursors are pyrolyzed in high-temperature boiling solutions. The primary drawback of the method is that the isolation from the reactive phase of the unstable nanocrystal phase becomes very challenging at such high temperatures [65]. In general, because of the high energy demand for bond breakages, the thermal technique is of an endothermic nature. The photochemical technique enables nanoparticles of exceptional size and composition to be isolated and studied.

1.3.2 Sputtering

Sputtering is a technique for ejecting nanoparticles from a target material's surface utilizing outer stimulation with a high level of energy. Nanoparticles are ejected while supplied energy is greater than that provided by normal thermal energies. This technique yields high-purity nanoparticles. Magnetic sputtering, for example, is used to create silicon nanowires. This technique has certain disadvantages, such as a lack of control over particle shape and significant energy consumption for the electron ejection [65]. Because a high temperature is necessary, it might be dangerous, resulting in a variety of skin disorders.

1.3.3 Sol-gel method

Sol and gel are the two words that make up the sol-gel method. A stable colloidal solid particles' dispersion in a liquid is known as a sol. The scattered phase is minimal that there are merely forces of Vander-Waal. The solid level in a gel is greater than the liquid level. The particles or ions produce a continual network during evaporation that leads to the quasi-rigid form. Covalent interactions exist in most gel systems. The sol-gel technique is a mixture of these two network functions. Hydrolysis and condensation are the two major processes in this technique. The sol-gel technique is used to make a variety of bimetallic nanoparticles, including Ag-Au, Pd-Au, and Pt-Au, etc [65].

1.3.4 Chemical precipitation process

Chemical precipitation is the way of transforming a liquid into a solid by making it infusible or over saturating a solution. It entails adding chemical reagents to the solution and then separating the precipitates from it. This technique can be used to make ZnO and ZnS nanoparticles. This is a highly beneficial technology as it is a one-step process that helps to produce nanoparticles on a big scale without impurities. This process also aids in water filtration and is a long-term solution that yields lasting benefits.

1.3.5 Micro-emulsion method

A micro-emulsion is a solution that has no less than three elements: surfactant, polar, and non-polar element. Surfactant is utilized for generating a tier within polar and non-polar components. Even in nature, it is thermodynamically stable and homogenous. Depending on the kind of dispersed and continuous phase, the microemulsion can be categorized as water-in-oil or oil-in-water. Oil in water micro-emulsion can only produce a few organic nanoparticles. Cyclic voltammetric and Chrono amperometry measurements are used to investigate the electrocatalytic activity of these nanoparticles, revealing that they are stable. The microemulsion technique is utilized to create the La/Cd bimetallic nanoparticles, which are then employed to degrade organic contaminants.

1.3.6 Hydrothermal method

Using this method, nanoparticles are manufactured by applying high pressure with high temperatures (approximately 470°C). Components that are typically non-soluble under normal circumstances can be diluted using this technique. The characteristics of the resultant nanoparticles are then determined by the medium pH, temperature, and pressure. This approach might be improved further since it will aid in the monitoring of crystal development. Because of the high yield and purity of the products, this technique is

useful. Furthermore, it creates high-quality crystals and allows us to regulate the physical and chemical characteristics of the resultant nanoparticles [13]. The expensive cost of equipment and the inability to supervise the crystal development process are the disadvantages of this approach [65]. This technique has been used to synthesize zeolites and lead telluride nanoparticles.

1.3.7 Electrochemical reduction

In this approach, the driving force or control force is electricity. The current is transferred between the two electrodes separated by an electrolyte. The electrochemical process is commonly applied for metallic nanoparticles synthesis [44]. The metal salt is dissolved and reduced to form metallic particles. The advantage of electrochemical technology is that of low-cost preparation, good particle purity, particle size control by optimization of current density, and an easy operating manner. This technique is utilized mostly in commercial processes.

1.3.8 Chemical reduction

This technique is used to create metal nanoparticles in a zero-valent condition. Reduction and interaction between polymer with metallic species are the two mechanisms used in

this technique. Sodium borohydride, elemental hydrogen, Tollen's reagent, and ascorbate are the common reducing agents employed in this process. For the production of silver nanoparticles, a chemical reduction is a popular approach [65]. The highly promising way of manufacturing bimetallic core-shell nanoparticles is by successive reduction. It entails the deposition of a metal onto monometallic nanoparticles of other metals that have been produced.

There are various methods for the preparation of metal nanostructures. However, some of the methods need high temperature (Hydrothermal, Sputtering, etc), high pressure (Hydrothermal), more than one step (Sol-gel method), or special types of equipment [5]. One-pot simple synthesis methods at room temperature are highly desirable for the preparation of metal hierarchical nanostructures. So I choose three methods (Electroless deposition, Electrodeposition, Chemical reduction) for the synthesis of hierarchical catalyst by the one-pot process at room temperature without using high pressure.

1.4 Electrochemical Techniques to Evaluate Ascorbic Acid Electrooxidation

Electrochemical methods are based on the application of an electric input through electron-conducting electrodes submerged in an electrochemical cell containing an ion-conducting phase, the electrolyte, to assess the response of the electrochemical cell. A potentiostat linked to electrodes submerged in an electrolyte to control and measure the rate of oxidation and/or reduction reactions (Figure 1.6). The AA electrooxidation will be evaluated by the below techniques:

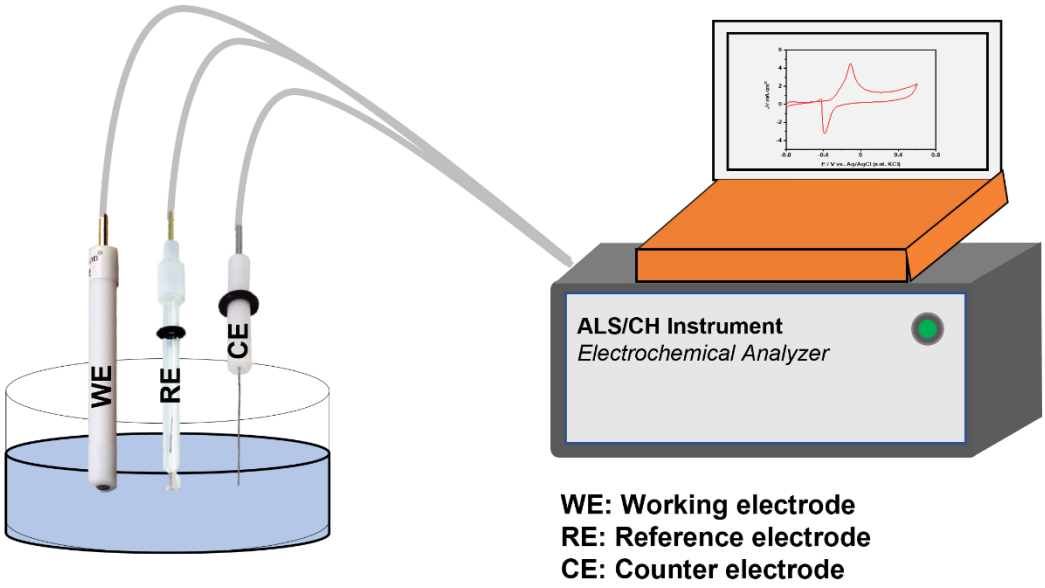

Figure 1.6 Three electrode system potentiostat.

1.4.1 Cyclic Voltammetry

Cyclic voltammetry is the most widely used method for investigating electrochemical reactions. It involves recording the current response of a working electrode as a function of the potential difference established between that electrode and a suitable reference electrode (usually Ag/AgCl). A third electrode (counter electrode) is frequently included in electrochemical devices to reduce the current passing through the working electrode (Figure 1.6). The reason for this is that at the working electrode, electrons are transferred between the species of interest and the electrode, causing changes in the electrolyte composition. These processes are known as faradic processes and should only happen to a small amount to keep the system composition unchanged. Figure 1.7 shows the cyclic voltammogram of AA electrooxidation by Pd modified glassy carbon electrode (Pd/GCE) in 1 M KOH solution. In the forward scan, the oxidation peak is due to oxidation of AA while in the reverse scan the reduction peak is for the PdO reduction peak.

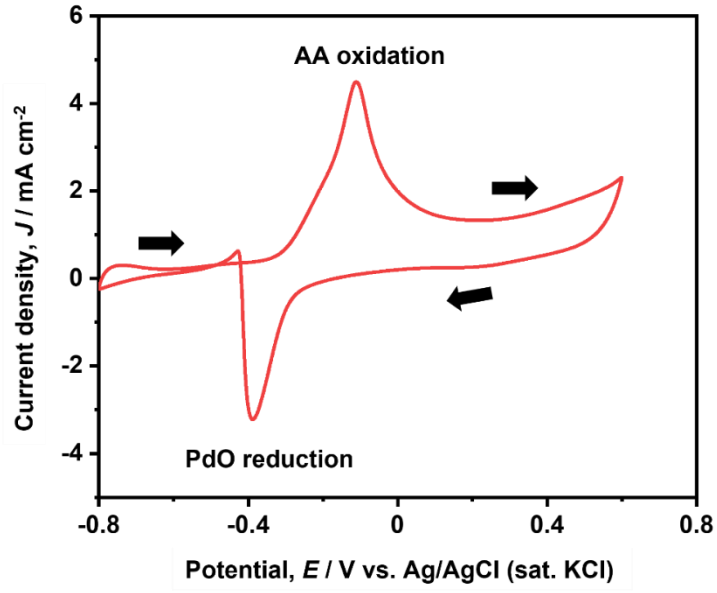

Figure 1.7 Cyclic voltammograms of Pd/GCE in the presence of 5.6 mM ascorbic acid in 1 M KOH solution at 50 mV s^{-1} (reference electrode: Ag/AgCl (sat. KCl)).

1.4.2 Electrochemical Impedance Spectroscopy

Electrochemical impedance spectroscopy (EIS) is a quick, non-destructive, and easily automated method for determining the electric characteristics of a wide range of materials. EIS is a vital electrochemical method that relies on the interfacial response at the electrode surface. The basic Ohm's law cannot explain the complex circuit components that are common in an electrochemical reaction. EIS is therefore utilized to analyze more general and complicated circuit characteristics. The EIS spectrum is usually shown as a complex plane plot, where Z′ represents the real and Z″ represents

the imaginary component of impedance, respectively. The simplified Randle circuit, for an ideal non-polarizable system, consists of a series connection of solution resistance (R_s) with a parallel combination of charge transfer resistance (R_{ct}) and a double layer capacitance (C_{dl}), Warburg element (w) [18,66].

$$T_1 = \frac{R_s R_{ct} C_{dl}}{R_s + R_{ct}} \ldots\ldots\ldots\ldots\ldots\ldots\ldots\ldots\ldots\ldots\ldots\ldots (1)$$

$$T_2 = R_{ct} C_{dl} \ldots\ldots\ldots\ldots\ldots\ldots\ldots\ldots\ldots\ldots\ldots\ldots\ldots (2)$$

Where T_1 and T_2 are the two corresponding breakpoints of time constants in the Bode module. The Cole-Cole plot or Nyquist plot is formed by plotting the real and imaginary portions of impedance on the X and Y axes, respectively. The typical Nyquist plot for bare GCE and silver modified GCE (Ag/GCE) for AA oxidation is seen in Figure 1.8. These resistances include the resistance of electrode materials and the resistance of the catalyst. The semi-circle also has an impact on calculating charge transfer resistance. While the diffusion coefficient controls the impedance at lower frequencies. The ionic and electrical conductivity of the material has a considerable influence on the actual impedance in the left-most region of the Nyquist plot.

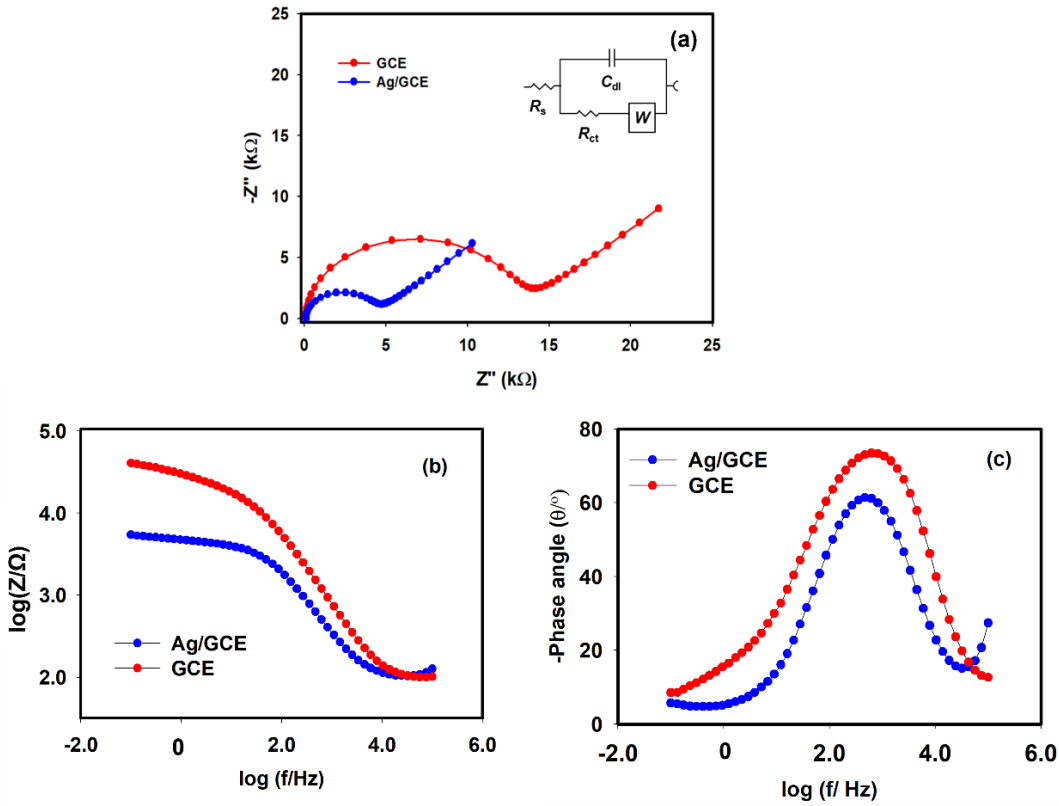

Figure 1.8 EIS spectra in presence of ascorbic acid in neutral pH solution (pH~7.0) at unmodified GCE and Ag/GCE. (a) Nyquist plots (inset: equivalent circuit), (b) bode modulus plots, and (c) bode phase plots.

1.4.3 Chronoamperometry

Chronoamperometry is a time-dependent method that employs a square-wave potential on the working electrode. Because of analyte diffusion from the bulk solution toward the electrode surface, the electrode current changes with time. Therefore, the time dependency of a diffusion-controlled process on an electrode may be quantified using

chronoamperometry. This depends on the concentration of the analyte. Chronoamperometry is a sensitive method and has been used in a variety of investigations, either alone or in conjunction with other electrochemical techniques such as cyclic voltammetry. The electrochemical activity and stability of the electrocatalysts are investigated using chronoamperometry tests. A typical chronoamperometry graph for the Ag/GCE in the presence of AA is shown in Figure 1.9. The flat line after the startup proved that the stability of the Ag/GCE electrode during the AA electrooxidation in the neutral pH solution.

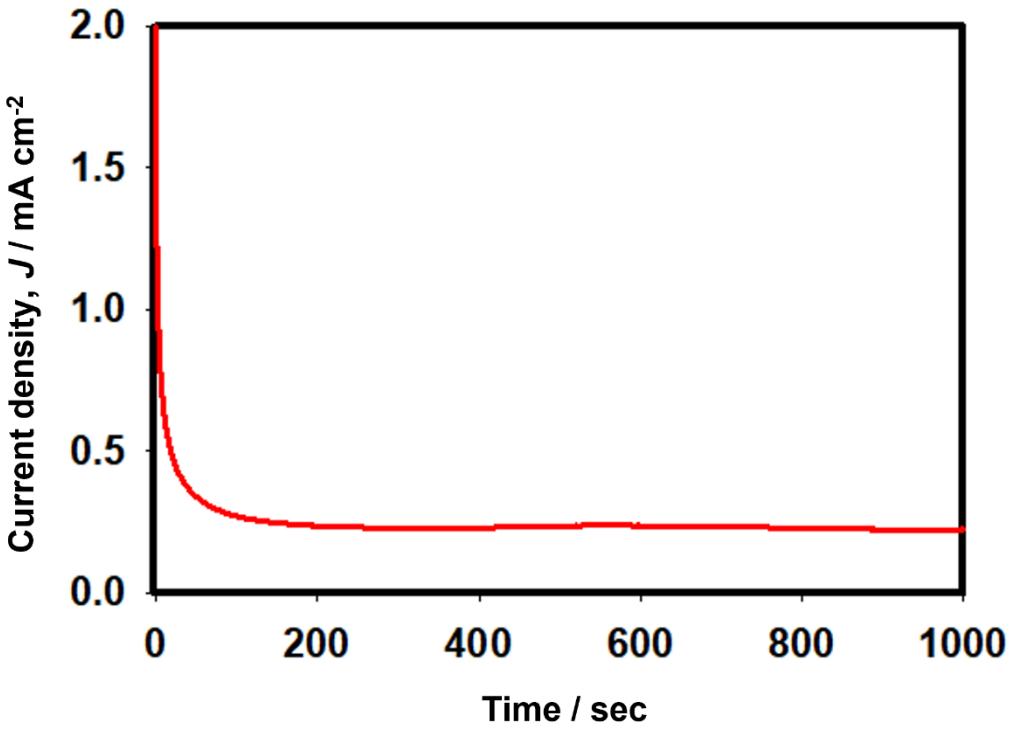

Figure 1.9 Chronoamperometry in presence of ascorbic acid at the Ag/GCE electrode.

1.5 Introduction of Fuel Cell

Fuel cells (FC) are electrochemical devices that transform chemical energy into electrical energy [67–69]. An electrolyte medium is placed between two electrodes in these devices. The anode electrode permits electrochemical oxidation of the fuel while the cathode promotes the electrochemical reduction of the oxidant. The ionically conductive but electrically insulating electrolyte transports ions, produced during oxidation or reduction from one electrode to the other. Between the fuel and the oxidant, the electrolyte acts as a barrier. Electrons produced at the anode during oxidation moved via the external circuit (producing energy) on their way to the cathode, where they complete the reduction reaction. The fuel and oxidant do not combine at any time, and no real combustion occurs. As a result, the fuel cell is not restricted by the Carnot efficiency and, theoretically can achieve 100% efficiency. The electrolyte substance is used to classify fuel cells. The fuel cell operating temperature is also determined by the electrolyte material used. Figure 1.10 exhibited different types of fuel cells and their operating temperature.

1.5.1 Polymer Electrolyte Membrane Fuel Cell

This is commonly known as a proton exchange membrane fuel cell, which has superior energy compared to conventional fuel cells. The electrolyte of PEM (polymer electrolyte Membrane) fuel cells is a solid polymer, and the electrodes are porous carbon with platinum nanoparticles. Hydrogen and humidified oxygen are used to generate power in PEM fuel cells at low temperatures (80°C). Generally, hydrogen is provided from

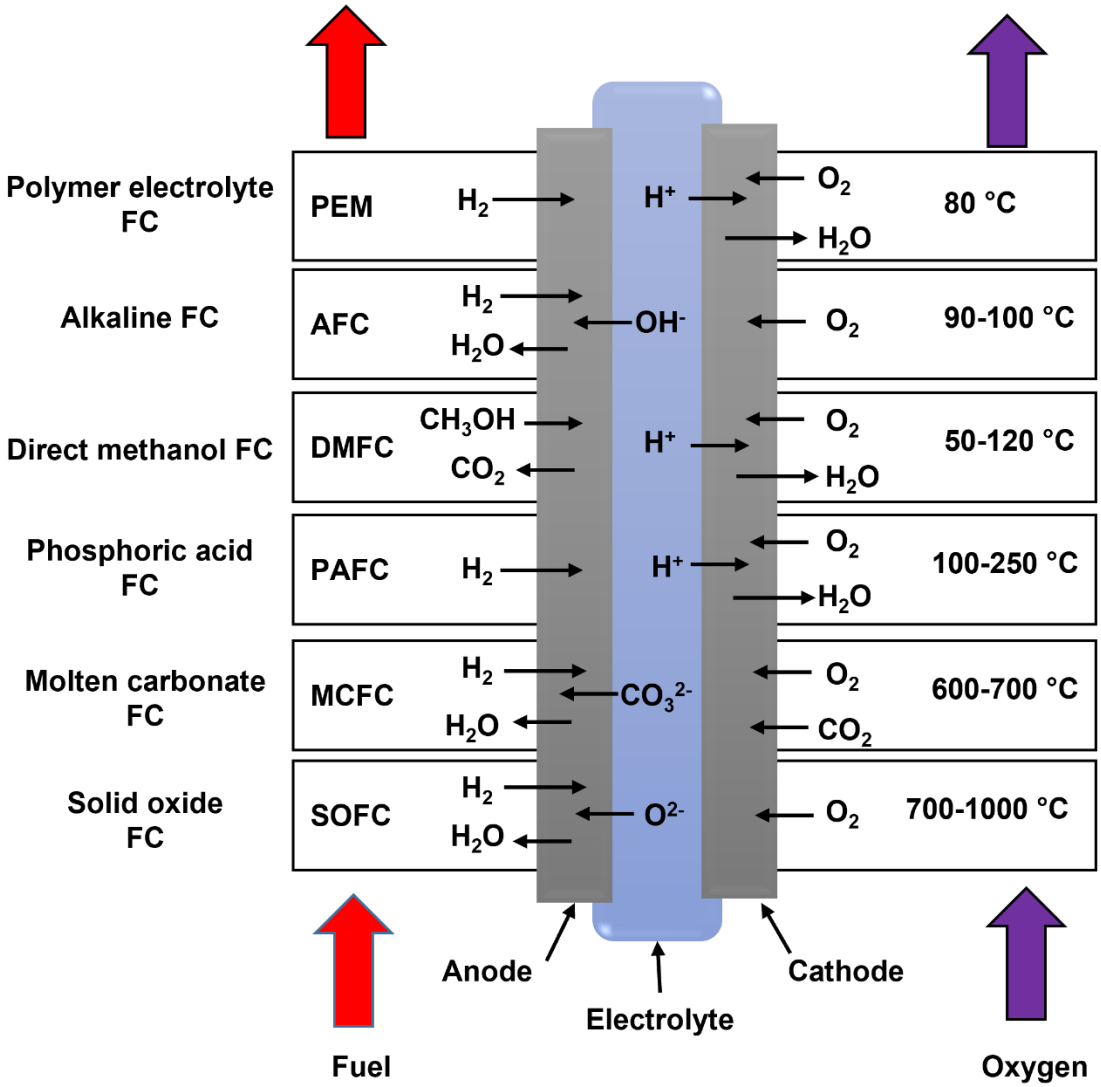

Figure 1.10 Various types of fuel cells and their operating conditions.

cylinders. PEM fuel cells can start faster because of their low-temperature functioning. They also have a long lifespan. However, the necessitated use of a noble metal catalyst like Pt raises the system cost.

1.5.2 Alkaline Fuel Cell

Alkaline fuel cells (AFCs) employ alkaline solution as electrolyte and metal catalysts (non-precious) for anode and cathode reactions. These fuel cells utilize an alkaline membrane (capable of anion exchange). The great efficiency of AFCs is attributed to the fast rate of electrochemical reactions in the cell. One of the most serious issues of AFCs is that they are very sensitive to carbon dioxide. In contrast, due to carbonate formation, even a tiny quantity of CO_2 in the air can have a significant impact on cell performance and durability. Additional issues with liquid electrolyte systems include wettability, increased corrosion, etc.

1.5.3 Phosphoric Acid Fuel Cell

The electrolyte of PAFCs (phosphoric acid fuel cells) is phosphoric acid and the electrodes are Pt-loaded porous carbon catalysts. It is one of the most developed fuel cells to be commercialized. Although PAFCs are generally used for stationary power

production, they have also been utilized for big vehicles like buses. PAFCs have better tolerance of impurities in fossil fuels than PEM fuel cells. When utilized for co-generation of heat and electricity, PAFCs are higher than 85% efficient; however, they become less efficient when used to generate electricity alone (37%–42%).

1.5.4 Molten Carbonate Fuel Cell

MCFCs (molten carbonate fuel cells) are established for power stations, as well as for industrial and utility uses. MCFCs are operated at high temperatures and the electrolyte is a molten carbonate salt combination floating in a chemically inert porous ceramic lithium aluminum oxide matrix. Non-precious metals catalyst can be employed at both sides of the fuel cell since they function at high temperatures of 650 °C. Methane, as well as hydrocarbons, could be transformed to hydrogen inside MCFCs (internal reforming) at high temperatures which cut costs. The main drawback of present MCFCs technology is its lack of longevity. High temperature along with corrosive electrolyte reducing cell life.

1.5.5 Solid Oxide Fuel Cell

SOFCs (solid oxide fuel cells) need ceramic materials as electrolytes. SOFCs work at extremely high temperatures, up to 1,000°C. The high-temperature process eliminates the requirement for a precious metal catalyst, lowering costs. In SOFCs, fuels can reform internally, allowing them to utilize a wider range of fuels while lowering expenses. There are certain drawbacks to high-temperature operation. It causes a sluggish starting and necessitates a lot of thermal shielding to keep the heat in and protect the workers, which is only applicable for stationary utility applications.

1.5.6 Direct Liquid Fuel Cell

Direct liquid fuel cells (DLFCs) are becoming increasingly popular due to specific benefits over other equivalent fuel cells like PEM fuel cells [70,71]. DLFCs are regarded as ground-breaking prospects for producing electrical power for cars, household uses, high-tech portable gadgets, and so on. Although PEM fuel cells are frequently investigated, commercialization is inadequate owing to hydrogen storage, safety, and supply [72]. Under these conditions, the possibility for simple handling and storage, as well as high power densities, are regarded as acceptable alternative fluids like methanol, ethylene glycol, ethanol [73–75]. Alcohol-based fuel cells (DAFCs) have high efficiency

and power generating capabilities that could be alternatives to PEM fuel cells [70,76]. For example, methanol and ethanol-based fuel cells have been extensively researched, and several state-of-the-art electrocatalysts have been published recently [77–80]. While the alcohol-based DLFC system performance is taken into consideration, alkaline-based fuel cell systems are superior to acidic systems. High concentrations of OH^- ion in alkaline environments have been demonstrated to improve the kinetics of fuel oxidation, thus allowing for improved performance [77,81]. However, on the benchmark Pt-based electrocatalysts, the multielectron alcohol oxidation kinetics is dominated by a parallel route mechanism, with CO severely inhibiting its catalytic regions [82–84]. Second, alcohol crossover becomes a significant problem at high current density and poisoned cathode catalyst [85–87]. As a result, the large amount of precious metal-loaded cathode catalysts is necessary as well as the designing of their catalytic regions for selective oxygen reduction reactions (ORR) [88,89]. All of these factors effectively impede the commercialization of DAFC technology. Despite great attempts to design the catalytic domains to promote selective ORR with intrinsic alcohol inertness, these techniques have yet not been accomplished. Another environmental concern about the use of alcohol-based DLFCs is the CO_2 produced during the oxidation of alcohol. Figure 1.11 showed the alcohol-based DLFCs in both acidic and alkaline conditions. As a result, the

development of alternative environmentally-friendly DLFCs has received a lot of attention recently.

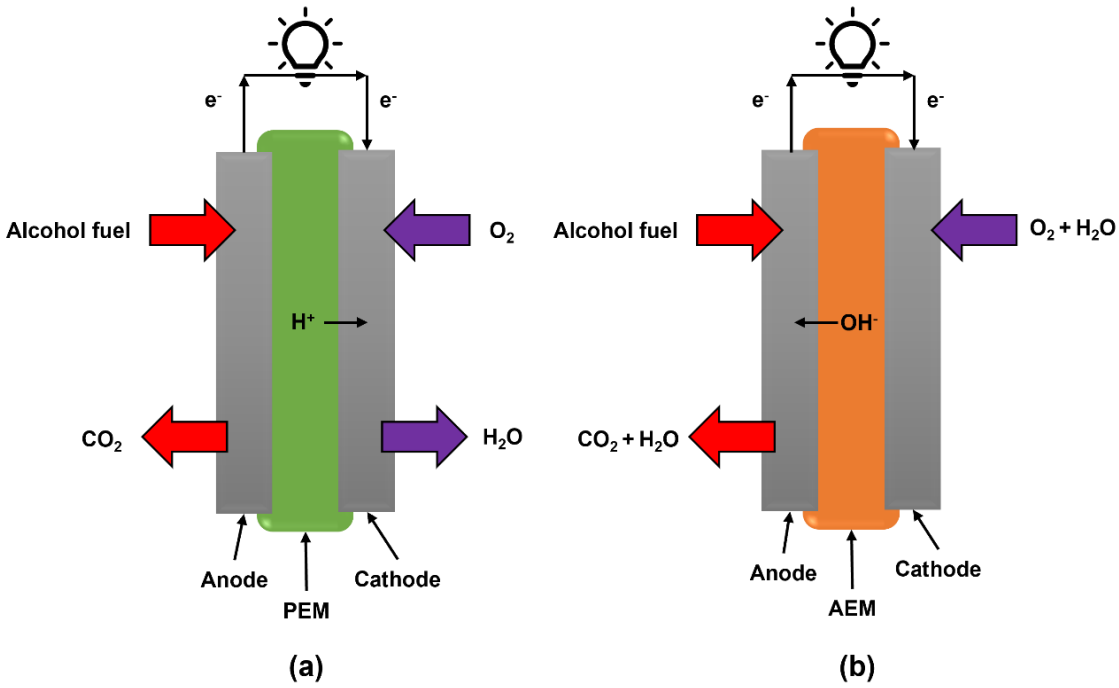

Figure 1.11 Alcohol-based direct liquid fuel cells (a) acidic and (b) alkaline conditions.

1.6 Introduction of Direct Ascorbic Acid Fuel Cell

DLFC is projected to be a potential choice for portable energy sources because of its relatively simple system design and cell operation. However, several barriers, such as poor electrocatalytic activity and low fuel efficiency owing to fuel crossover, continue to hinder their broad commercial implementation [90,91]. Furthermore, the toxicity of the fuel and by-products may create additional significant issues. AA has recently been

explored for fuel cell systems because of its safety and environmentally benign character [7,43,45,92–95].

1.6.1 Direct Acidic Ascorbic Acid Fuel Cell

AA is an ecologically and physiologically friendly, cheap chemical. This is a stable powder that can be kept in the air and is nontoxic and water-soluble. AA is generated through the fermentation or chemical conversion of D-glucose, therefore, it may be classed as biomass-derived fuel and used as a regenerative fuel in a variety of applications [43]. Previous research has shown AA to be a promising candidate for DLFCs as an alternative fuel. The direct acidic AA fuel cell with cation exchange membrane and a range of anode catalyst surfaces including Pt, Ru, Pd, Ir, Rh, PtRu, and carbon black (Vulcan XC72), has been reported by Fujiwara et al. [7,95]. Pd black demonstrated the greatest performance among these precious metal catalysts. However, the highest power density is exhibited between 12-15 mW cm^{-2} using carbon black anode, twice as much as Pd black metal catalyst (7 mW cm^{-2}). The electrochemically active surface area of the electrodes is the result of observed fuel cell performance variations on each anodic catalyst. In addition, AA functions as the Nafion ionomer-like proton conductor, an ionomer utilized in proton exchange for the electrolyte substitution in acid

cells. It has been demonstrated that increasing Nafion ionomer mass or thickness can impede the mass transfer of AA to the electrode surface, therefore decreasing the oxidation rate. Furthermore, Uhm et al. carried out a work that mentioned pouring the electrolyte into the carbon electrodes microstructure to enhance the polar functionality of the electrode surface. This modified carbon electrode generated 18 mW cm^{-2} power at 60 °C [93]. Y. Zeng et al. carried out a study that focused on the mathematical modeling of the direct AA fuel cell and examined the kinetics and mass transfer between the solution and catalyst layers. It is discovered by the model, that the concentration of AA and the cathode reaction are the variables for total fuel cell performance [96]. Mondal et al. also investigated the fuel performance using various PANI loadings. As the voltage reduced from the open-circuit potential (0.5V), an increase in current density occurred. In addition, when the temperature of the fuel cell increased, the open-circuit voltage dropped. However, the performance of fuel cells increased from 27 °C to 70 °C, suggesting that the direct AA fuel cell operates across a large range of temperatures. At a current density of 15 mA cm^{-2}, the highest power density of 4.3 mW cm^{-2} is observed at 70 °C. This also showed that a direct acidic AA fuel cell may be operated with a low-cost anodic catalyst [40].

1.6.2 Direct Alkaline Ascorbic Acid Fuel Cell

For alkaline DLFCs, the alkaline anion exchange membrane (AEM) provides benefits over the cation exchange membrane (e.g., Nafion) [43]. Water is generated at the anode side of alkaline DLFCs; thus water management is negligible, and the cathode has little effect on total fuel cell efficiency. Alkaline fuel cells have a lower activation overpotential, have faster reaction kinetics, and are less toxic and corrosive to the fuel cell components, particularly the metal catalysts. Finally, liquid fuels in the alkaline DLFC can be handled, stored, and transported more easily than hydrogen [97]. Muneeb et al. used an anion exchange membrane to operate the first direct alkaline AA fuel cell (DAAFC). The fuel cell has a maximum power density of 27 mW cm^{-2} at room temperature using a Pd black anode catalyst, which is substantially greater than previously reported acidic AA fuel cell [43]. The highest power density and the current density of this DAAFC at 60°C are 73 mW cm^{-2} and 497 mA cm^{-2}, respectively. Muneeb et al. further showed that PdCu/C (anode) may further increase the maximum fuel cell output to 89 mW cm^{-2} with Pt black at the cathode at 60°C [44]. This entitled us about the use of alkaline direct AA fuel cell design than the acidic one. Figure 1.12 showed a single cell of the DAAFC system.

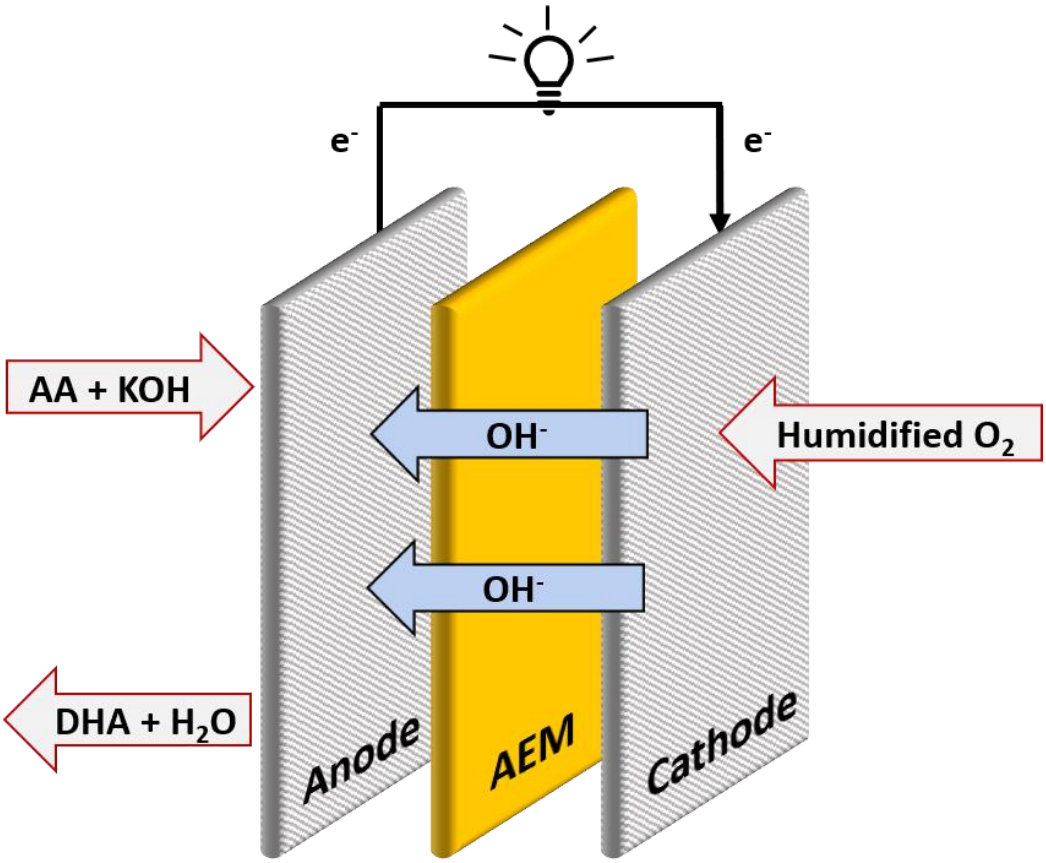

Figure 1.12 A single cell of the direct alkaline ascorbic acid fuel cell.

1.7 Outline of This Thesis

In this thesis, all the chapters are designed with a single objective to establish an easy and cost-effective technique for the preparation of different metal catalysts for AA electrooxidation. The AA is naturally abundant and produces nontoxic by-products during oxidation. For the practical use of the DAAFC system, a suitable anode catalyst has needed for the electrocatalysis enhancement of AA oxidation. For this reason, we are developing metal catalysts for AA electrooxidation. We would like to explore new

approaches for the synthesis of metal catalysts and apply them for AA electrooxidation. In this thesis, unique structures of metal catalysts have been developed for the first time using different fabrications approaches. A simple electroless deposition technique has been developed for hierarchical silver dendrite structures in chapter 2. The detailed electrokinetic study of the AA oxidation process has been studied in the neutral condition using a hierarchical silver dendrite metal catalyst. The kinetic study helped us to understand the electron transfer process. In the third chapter, a controlled electrodeposition technique will be discussed the formation of hierarchical Christmas-tree-shape Pd structures. The electrocatalysis will show that the Pd catalyst has a good catalytic performance and high selectivity for AA electrooxidation in the alkaline condition. A simple chemical reduction technique will be used to create Pd NPs integrated rGO and MWNT composites in the fourth chapter. Further, the DAAFC performance will investigate using this composite catalyst in alkaline conditions. The performance of the AA electrocatalytic system will be fully investigated in this thesis to create a viable DAAFC anode catalyst.

References

[1] V.D. Yadav, R. Jain, P. Dandekar, Influence of sodium hydroxide in enhancing the surface plasmon resonance of silver nanoparticles, Mater. Res. Express. 4 (2017) 085015. https://doi.org/10.1088/2053-1591/aa8088.

[2] W. Pct, Patents Device for permeation of carbon dioxide and method for transport of carbon dioxide, 2012. https://patents.google.com/patent/WO2013089221A1/en.

[3] M. Noroozifar, M. Khorasani-Motlagh, A. Taheri, Preparation of silver hexacyanoferrate nanoparticles and its application for the simultaneous determination of ascorbic acid, dopamine and uric acid, Talanta. 80 (2010) 1657–1664. https://doi.org/10.1016/j.talanta.2009.10.005.

[4] A. Pisoschi, A. Pop, G.P. Negulescu, A. Pisoschi, Determination of Ascorbic Acid Content of Some Fruit Juices and Wine by Voltammetry Performed at Pt and Carbon Paste Electrodes, Molecules. 16 (2011) 1349–1365. https://doi.org/10.3390/molecules16021349.

[5] C.R. Raj, K. Tokuda, T. Ohsaka, Electroanalytical applications of cationic self-assembled monolayers: square-wave voltammetric determination of dopamine and ascorbate, Bioelectrochemistry. 53 (2001) 183–191.

https://doi.org/10.1016/S0302-4598(00)00129-X.

[6] N.A. Sagar, S. Pareek, S. Sharma, E.M. Yahia, M.G. Lobo, Fruit and Vegetable Waste: Bioactive Compounds, Their Extraction, and Possible Utilization, Compr. Rev. Food Sci. Food Saf. 17 (2018) 512–531. https://doi.org/10.1111/1541-4337.12330.

[7] N. Fujiwara, S. Yamazaki, Z. Siroma, T. Ioroi, K. Yasuda, Direct oxidation of l-ascorbic acid on a carbon black electrode in acidic media and polymer electrolyte fuel cells, Electrochem. Commun. 8 (2006) 720–724. https://doi.org/10.1016/j.elecom.2006.02.021.

[8] K. Karaboduk, Electrochemical Determination of Ascorbic Acid Based on AgNPs/PVP-Modified Glassy Carbon Electrode, ChemistrySelect. 4 (2019) 6361–6369. https://doi.org/10.1002/slct.201901102.

[9] R.F. Cathcart, A Unique Function for Ascorbate, Med. Hypotheses. 35 (1991) 32–37.

[10] A.M. Pisoschi, A. Pop, A.I. Serban, C. Fafaneata, Electrochemical methods for ascorbic acid determination, Electrochim. Acta. 121 (2014) 443–460. https://doi.org/10.1016/j.electacta.2013.12.127.

[11] V.L. da Silva, M.R.F. Cerqueira, D. Lowinsohn, M.A.C. Matos, R.C. Matos, Amperometric detection of ascorbic acid in honey using ascorbate oxidase immobilised on amberlite IRA-743, Food Chem. 133 (2012) 1050–1054. https://doi.org/10.1016/j.foodchem.2012.01.066.

[12] A. Rizzolo, A. Brambilla, S. Valsecchi, P. Eccher-Zerbini, Evaluation of sampling and extraction procedures for the analysis of ascorbic acid from pear fruit tissue, Food Chem. 77 (2002) 257–262. https://doi.org/10.1016/S0308-8146(02)00107-3.

[13] M.A. Zahed, S.C. Barman, R.M. Toyabur, M. Sharifuzzaman, X. Xuan, J. Nah, J.Y. Park, Ex Situ Hybridized Hexagonal Cobalt Oxide Nanosheets and RGO@MWCNT Based Nanocomposite for Ultra-Selective Electrochemical Detection of Ascorbic Acid, Dopamine, and Uric Acid, J. Electrochem. Soc. 166 (2019) B304–B311. https://doi.org/10.1149/2.0131906jes.

[14] M. Abu Zahed, S.C. Barman, M. Sharifuzzaman, X. Xuan, J.S. Nah, J.Y. Park, Ex Situ Synthesis of Hexagonal NiO Nanosheets and Carboxyl-Terminated Reduced Graphene Oxide Nanocomposite for Non-Enzymatic Electrochemical Detection of H2O2 and Ascorbic Acid, J. Electrochem. Soc. 165 (2018) B840–B847.

https://doi.org/10.1149/2.0621816jes.

[15] G. Wu, Y. Wu, X. Liu, M. Rong, X. Chen, X. Chen, An electrochemical ascorbic acid sensor based on palladium nanoparticles supported on graphene oxide, Anal. Chim. Acta. 745 (2012) 33–37. https://doi.org/10.1016/j.aca.2012.07.034.

[16] M. Saleh Mohammadnia, E. Marzi Khosrowshahi, E. Naghian, A. Homayoun Keihan, E. Sohouli, M.E. Plonska-Brzezinska, Ali-Sobhani-Nasab, M. Rahimi-Nasrabadi, F. Ahmadi, Application of carbon nanoonion-$NiMoO_4$-$MnWO_4$ nanocomposite for modification of glassy carbon electrode: Electrochemical determination of ascorbic acid, Microchem. J. 159 (2020) 105470. https://doi.org/10.1016/j.microc.2020.105470.

[17] C.S. Erdurak-Kiliç, B. Uslu, B. Dogan, U. Ozgen, S.A. Ozkan, M. Coskun, Anodic voltammetric behavior of ascorbic acid and its selective determination in pharmaceutical dosage forms and some Rosa species of Turkey, J. Anal. Chem. 61 (2006) 1113–1120. https://doi.org/10.1134/S106193480611013X.

[18] M.M. Hasan, R.H. Rakib, M.A. Hasnat, Y. Nagao, Electroless Deposition of Silver Dendrite Nanostructure onto Glassy Carbon Electrode and Its Electrocatalytic Activity for Ascorbic Acid Oxidation, ACS Appl. Energy Mater.

3 (2020) 2907–2915. https://doi.org/10.1021/acsaem.9b02513.

[19] F. Prieto, B.A. Coles, R.G. Compton, Mechanistic Determination Using Arrays of Variable-Sized Channel Microband Electrodes: The Oxidation of Ascorbic Acid in Aqueous Solution, J. Phys. Chem. B. 102 (1998) 7442–7447. https://doi.org/10.1021/jp982080n.

[20] M.R. Deakin, P.M. Kovach, K.J. Stutts, R.M. Wightman, Heterogeneous mechanisms of the oxidation of catechols and ascorbic acid at carbon electrodes, Anal. Chem. 58 (1986) 1474–1480. https://doi.org/10.1021/ac00298a046.

[21] I.F. Hu, T. Kuwana, Oxidative mechanism of ascorbic acid at glassy carbon electrodes, Anal. Chem. 58 (1986) 3235–3239. https://doi.org/10.1021/ac00127a069.

[22] M. Rueda, A. Aldaz, F. Sanchez-Burgos, Oxidation of L-ascorbic acid on a gold electrode, Electrochim. Acta. 23 (1978) 419–424. https://doi.org/10.1016/0013-4686(78)87040-6.

[23] J.J. Ruiz, A. Aldaz, M. Dominguez, Mechanism of L-ascorbic acid oxidation and dehydro- L-ascorbic acid reduction on a mercury electrode. I. Acid medium, Can. J. Chem. 55 (1977) 2799–2806. https://doi.org/10.1139/v77-389.

[24] X.L. Wen, Z.L. Liu, Z.X. Han, A. Rieker, Significant Micellar Effect on the Oxidative Electrochemistry of Ascorbic Acid†, J. Chem. Res. (1997) 108–109. https://doi.org/10.1039/a607061b.

[25] Y.J. Tu, D. Njus, H.B. Schlegel, A theoretical study of ascorbic acid oxidation and HOO˙/O_2˙− radical scavenging, Org. Biomol. Chem. 15 (2017) 4417–4431. https://doi.org/10.1039/C7OB00791D.

[26] K. Dhara, R.M. Debiprosad, Review on nanomaterials-enabled electrochemical sensors for ascorbic acid detection, Anal. Biochem. 586 (2019) 113415. https://doi.org/10.1016/j.ab.2019.113415.

[27] S. Kuss, R.G. Compton, Electrocatalytic detection of ascorbic acid using N,N,N',N'-tetramethyl-para-phenylene-diamine (TMPD) mediated oxidation at unmodified gold electrodes; reaction mechanism and analytical application, Electrochim. Acta. 242 (2017) 19–24. https://doi.org/10.1016/j.electacta.2017.05.003.

[28] X. Zhang, S. Yu, W. He, H. Uyama, Q. Xie, L. Zhang, F. Yang, Electrochemical sensor based on carbon-supported $NiCoO_2$ nanoparticles for selective detection of ascorbic acid, Biosens. Bioelectron. 55 (2014) 446–451.

https://doi.org/10.1016/j.bios.2013.12.046.

[29] L. Xi, D. Ren, J. Luo, Y. Zhu, Electrochemical analysis of ascorbic acid using copper nanoparticles/polyaniline modified glassy carbon electrode, J. Electroanal. Chem. 650 (2010) 127–134. https://doi.org/10.1016/j.jelechem.2010.08.014.

[30] J.B. Raoof, R. Ojani, M. Baghayeri, A selective sensor based on a glassy carbon electrode modified with carbon nanotubes and ruthenium oxide/hexacyanoferrate film for simultaneous determination of ascorbic acid, epinephrine and uric acid, Anal. Methods. 3 (2011) 2367. https://doi.org/10.1039/c1ay05305a.

[31] Y.G. Lee, B.X. Liao, Y.C. Weng, Ruthenium oxide modified nickel electrode for ascorbic acid detection, Chemosphere. 173 (2017) 512–519. https://doi.org/10.1016/j.chemosphere.2017.01.086.

[32] S. Thiagarajan, S. Chen, Preparation and characterization of PtAu hybrid film modified electrodes and their use in simultaneous determination of dopamine, ascorbic acid and uric acid, Talanta. 74 (2007) 212–222. https://doi.org/10.1016/j.talanta.2007.05.049.

[33] D. Zhao, G. Yu, K. Tian, C. Xu, A highly sensitive and stable electrochemical sensor for simultaneous detection towards ascorbic acid, dopamine, and uric acid

based on the hierarchical nanoporous PtTi alloy, Biosens. Bioelectron. 82 (2016) 119–126. https://doi.org/10.1016/j.bios.2016.03.074.

[34] X. Xing, I.T. Bae, M. Shao, C.C. Liu, Electro-oxidation of l-ascorbic acid on platinum in acid solutions: an in-situ FTIRRAS study, J. Electroanal. Chem. 346 (1993) 309–321. https://doi.org/10.1016/0022-0728(93)85021-8.

[35] D.N. Oko, S. Garbarino, J. Zhang, Z. Xu, M. Chaker, D. Ma, D. Guay, A.C. Tavares, Dopamine and ascorbic acid electro-oxidation on Au, AuPt and Pt nanoparticles prepared by pulse laser ablation in water, Electrochim. Acta. 159 (2015) 174–183. https://doi.org/10.1016/j.electacta.2015.01.192.

[36] M.T. Islam, M.M. Hasan, M.F. Shabik, F. Islam, Y. Nagao, M.A. Hasnat, Electroless deposition of gold nanoparticles on a glassy carbon surface to attain methylene blue degradation via oxygen reduction reactions, Electrochim. Acta. 360 (2020) 136966. https://doi.org/10.1016/j.electacta.2020.136966.

[37] N. Elahi, M. Kamali, M.H. Baghersad, Recent biomedical applications of gold nanoparticles: A review, Talanta. 184 (2018) 537–556. https://doi.org/10.1016/j.talanta.2018.02.088.

[38] B.R. Sathe, A scalable and facile synthesis of carbon nanospheres as a metal free

electrocatalyst for oxidation of l -ascorbic acid: Alternate fuel for direct oxidation fuel cells, J. Electroanal. Chem. 799 (2017) 609–616. https://doi.org/10.1016/j.jelechem.2017.03.049.

[39] C. Qiu, H. Chen, H. Liu, Z. Zhai, J. Qin, Y. Lv, Z. Gao, Y. Song, The hydrophilicity of carbon for the performance enhancement of direct ascorbic acid fuel cells, Int. J. Hydrogen Energy. 43 (2018) 21908–21917. https://doi.org/10.1016/j.ijhydene.2018.09.213.

[40] S.K. Mondal, R.K. Raman, A.K. Shukla, N. Munichandraiah, Electrooxidation of ascorbic acid on polyaniline and its implications to fuel cells, J. Power Sources. 145 (2005) 16–20. https://doi.org/10.1016/j.jpowsour.2005.01.001.

[41] S.A. Kumar, P.H. Lo, S.M. Chen, Electrochemical selective determination of ascorbic acid at redox active polymer modified electrode derived from direct blue 71, Biosens. Bioelectron. 24 (2008) 518–523. https://doi.org/10.1016/j.bios.2008.05.007.

[42] W. Pct, Patents Ion conductor , and electrochemical device using same, 2012. https://patents.google.com/patent/WO2014002756A1/en.

[43] O. Muneeb, E. Do, T. Tran, D. Boyd, M. Huynh, G. Ghosn, J.L. Haan, A direct

ascorbate fuel cell with an anion exchange membrane, J. Power Sources. 351 (2017) 74–78. https://doi.org/10.1016/j.jpowsour.2017.03.068.

[44] M.M. Hasan, Y. Nagao, Christmas-Tree-Shaped Palladium Nanostructures Decorated on Glassy Carbon Electrode for Ascorbic Acid Oxidation in Alkaline Condition, ChemistrySelect. 6 (2021) 5885–5892. https://doi.org/10.1002/slct.202100974.

[45] O. Muneeb, E. Do, D. Boyd, J. Perez, J.L. Haan, PdCu/C anode catalysts for the alkaline ascorbate fuel cell, Appl. Energy. 235 (2019) 473–479. https://doi.org/10.1016/j.apenergy.2018.10.073.

[46] J. Jiang, X. Du, Sensitive electrochemical sensors for simultaneous determination of ascorbic acid, dopamine, and uric acid based on Au@Pd-reduced graphene oxide nanocomposites, Nanoscale. 6 (2014) 11303–11309. https://doi.org/10.1039/C4NR01774A.

[47] L. Majari Kasmaee, F. Gobal, A preliminary study of the electro-oxidation of l-ascorbic acid on polycrystalline silver in alkaline solution, J. Power Sources. 195 (2010) 165–169. https://doi.org/10.1016/j.jpowsour.2009.06.095.

[48] M.A. Khalilzadeh, M. Borzoo, Green synthesis of silver nanoparticles using onion

extract and their application for the preparation of a modified electrode for determination of ascorbic acid, J. Food Drug Anal. 24 (2016) 796–803. https://doi.org/10.1016/j.jfda.2016.05.004.

[49] F. Gobal, L. Majari Kasmaee, Silver Selenide as a Potential Electro-catalyst for l-Ascorbic Acid Electro-oxidation in Alkaline Solution, Electrocatalysis. 2 (2011) 331–336. https://doi.org/10.1007/s12678-011-0069-7.

[50] F.A. Harraz, M. Faisal, A.E. Al-Salami, A.M. El-Toni, A.A. Almadiy, S.A. Al-Sayari, M.S. Al-Assiri, Silver nanoparticles decorated stain-etched mesoporous silicon for sensitive, selective detection of ascorbic acid, Mater. Lett. 234 (2019) 96–100. https://doi.org/10.1016/j.matlet.2018.09.076.

[51] J. Tashkhourian, M.R.H. Nezhad, J. Khodavesi, S. Javadi, Silver nanoparticles modified carbon nanotube paste electrode for simultaneous determination of dopamine and ascorbic acid, J. Electroanal. Chem. 633 (2009) 85–91. https://doi.org/10.1016/j.jelechem.2009.04.028.

[52] Y. Han, S. Liu, M. Han, J. Bao, Z. Dai, Fabrication of Hierarchical Nanostructure of Silver via a Surfactant-Free Mixed Solvents Route, Cryst. Growth Des. 9 (2009) 3941–3947. https://doi.org/10.1021/cg900066z.

[53] W.S. Chae, H.O. Lee, E.M. Kim, H. Yu, Molecular Sensing Efficiency of Gold-Silver Alloy Nanowires, Bull. Korean Chem. Soc. 32 (2011) 1346–1348. https://doi.org/10.5012/bkcs.2011.32.4.1346.

[54] X. Wen, Y.T. Xie, W.C. Mak, K.Y. Cheung, X.Y. Li, R. Renneberg, S. Yang, Dendritic Nanostructures of Silver: Facile Synthesis, Structural Characterizations, and Sensing Applications, Langmuir. 22 (2006) 4836–4842. https://doi.org/10.1021/la060267x.

[55] S. Choi, H. Jeong, K. Choi, J.Y. Song, J. Kim, Electrodeposition of Triangular Pd Rod Nanostructures and Their Electrocatalytic and SERS Activities, ACS Appl. Mater. Interfaces. 6 (2014) 3002–3007. https://doi.org/10.1021/am405601g.

[56] H. Meng, F. Xie, J. Chen, P.K. Shen, Electrodeposited palladium nanostructure as novel anode for direct formic acid fuel cell, J. Mater. Chem. 21 (2011) 11352. https://doi.org/10.1039/c1jm10361j.

[57] D. Yu, E. Nagelli, F. Du, L. Dai, Metal-Free Carbon Nanomaterials Become More Active than Metal Catalysts and Last Longer, J. Phys. Chem. Lett. 1 (2010) 2165–2173. https://doi.org/10.1021/jz100533t.

[58] K. Scida, P.W. Stege, G. Haby, G.A. Messina, C.D. García, Recent applications

of carbon-based nanomaterials in analytical chemistry: Critical review, Anal. Chim. Acta. 691 (2011) 6–17. https://doi.org/10.1016/j.aca.2011.02.025.

[59] Dhanjai, A. Sinha, X. Lu, L. Wu, D. Tan, Y. Li, J. Chen, R. Jain, Voltammetric sensing of biomolecules at carbon based electrode interfaces: A review, TrAC Trends Anal. Chem. 98 (2018) 174–189. https://doi.org/10.1016/j.trac.2017.11.010.

[60] S.C. Smith, D.F. Rodrigues, Carbon-based nanomaterials for removal of chemical and biological contaminants from water: A review of mechanisms and applications, Carbon N. Y. 91 (2015) 122–143. https://doi.org/10.1016/j.carbon.2015.04.043.

[61] S. Liu, X. Guo, Carbon nanomaterials field-effect-transistor-based biosensors, NPG Asia Mater. 4 (2012) e23–e23. https://doi.org/10.1038/am.2012.42.

[62] G.G. Wildgoose, C.E. Banks, H.C. Leventis, R.G. Compton, Chemically Modified Carbon Nanotubes for Use in Electroanalysis, Microchim. Acta. 152 (2006) 187–214. https://doi.org/10.1007/s00604-005-0449-x.

[63] M. Valcárcel, S. Cárdenas, B.M. Simonet, Role of Carbon Nanotubes in Analytical Science, Anal. Chem. 79 (2007) 4788–4797.

https://doi.org/10.1021/ac070196m.

[64] A.A. Rafati, A. Afraz, A. Hajian, P. Assari, Simultaneous determination of ascorbic acid, dopamine, and uric acid using a carbon paste electrode modified with multiwalled carbon nanotubes, ionic liquid, and palladium nanoparticles, Microchim. Acta. 181 (2014) 1999–2008. https://doi.org/10.1007/s00604-014-1293-7.

[65] G. Sharma, A. Kumar, S. Sharma, M. Naushad, R. Prakash Dwivedi, Z.A. ALOthman, G.T. Mola, Novel development of nanoparticles to bimetallic nanoparticles and their composites: A review, J. King Saud Univ. - Sci. 31 (2019) 257–269. https://doi.org/10.1016/j.jksus.2017.06.012.

[66] M.A. Hasnat, M.M. Hasan, N. Tanjila, M.M. Alam, M.M. Rahman, pH dependent kinetic insights of electrocatalytic arsenite oxidation reactions at Pt surface, Electrochim. Acta. 225 (2017) 105–113. https://doi.org/10.1016/j.electacta.2016.12.055.

[67] D. Sebastián, A. Serov, K. Artyushkova, J. Gordon, P. Atanassov, A.S. Aricò, V. Baglio, High Performance and Cost-Effective Direct Methanol Fuel Cells: Fe-N-C Methanol-Tolerant Oxygen Reduction Reaction Catalysts, ChemSusChem. 9

(2016) 1986–1995. https://doi.org/10.1002/cssc.201600583.

[68] M.M. Mohideen, Y. Liu, S. Ramakrishna, Recent progress of carbon dots and carbon nanotubes applied in oxygen reduction reaction of fuel cell for transportation, Appl. Energy. 257 (2020) 114027. https://doi.org/10.1016/j.apenergy.2019.114027.

[69] D.K. Ross, Hydrogen storage: The major technological barrier to the development of hydrogen fuel cell cars, Vacuum. 80 (2006) 1084–1089. https://doi.org/10.1016/j.vacuum.2006.03.030.

[70] Z.M. Bhat, R. Thimmappa, M.C. Devendrachari, S.P. Shafi, S. Aralekallu, A.R. Kottaichamy, M. Gautam, M.O. Thotiyl, A Direct Alcohol Fuel Cell Driven by an Outer Sphere Positive Electrode, J. Phys. Chem. Lett. 8 (2017) 3523–3529. https://doi.org/10.1021/acs.jpclett.7b01418.

[71] S. Sankar, N. Watanabe, G.M. Anilkumar, B.N. Nair, S.G. Sivakamiammal, T. Tamaki, T. Yamaguchi, Electro-oxidation competency of palladium nanocatalysts over ceria–carbon composite supports during alkaline ethylene glycol oxidation, Catal. Sci. Technol. 9 (2019) 493–501. https://doi.org/10.1039/C8CY02232A.

[72] E. Katz, I. Willner, J. Wang, Electroanalytical and Bioelectroanalytical Systems

Based on Metal and Semiconductor Nanoparticles, Electroanalysis. 16 (2004) 19–44. https://doi.org/10.1002/elan.200302930.

[73] L. An, T.S. Zhao, Y.S. Li, Carbon-neutral sustainable energy technology: Direct ethanol fuel cells, Renew. Sustain. Energy Rev. 50 (2015) 1462–1468.

[74] E. Antolini, Catalysts for direct ethanol fuel cells, J. Power Sources. 170 (2007) 1–12. https://doi.org/10.1016/j.jpowsour.2007.04.009.

[75] L. An, R. Chen, Recent progress in alkaline direct ethylene glycol fuel cells for sustainable energy production, J. Power Sources. 329 (2016) 484–501.

[76] D. Sebastián, A. Serov, I. Matanovic, K. Artyushkova, P. Atanassov, A.S. Aricò, V. Baglio, Insights on the extraordinary tolerance to alcohols of Fe-N-C cathode catalysts in highly performing direct alcohol fuel cells, Nano Energy. 34 (2017) 195–204. https://doi.org/10.1016/j.nanoen.2017.02.039.

[77] E. Antolini, E.R. Gonzalez, Alkaline direct alcohol fuel cells, J. Power Sources. 195 (2010) 3431–3450. https://doi.org/10.1016/j.jpowsour.2009.11.145.

[78] B.A. Kakade, T. Tamaki, H. Ohashi, T. Yamaguchi, Highly Active Bimetallic PdPt and CoPt Nanocrystals for Methanol Electro-oxidation, J. Phys. Chem. C. 116 (2012) 7464–7470. https://doi.org/10.1021/jp300140s.

[79] M.A.F. Akhairi, S.K. Kamarudin, Catalysts in direct ethanol fuel cell (DEFC): An overview, Int. J. Hydrogen Energy. 41 (2016) 4214–4228.

[80] M.D. Obradović, Z.M. Stančić, U.Č. Lačnjevac, V.V. Radmilović, A. Gavrilović-Wohlmuther, V.R. Radmilović, S.L. Gojković, Electrochemical oxidation of ethanol on palladium-nickel nanocatalyst in alkaline media, Appl. Catal. B Environ. 189 (2016) 110–118. https://doi.org/10.1016/j.apcatb.2016.02.039.

[81] S. Basri, S.K. Kamarudin, W.R.W. Daud, Z. Yaakub, Nanocatalyst for direct methanol fuel cell (DMFC), Int. J. Hydrogen Energy. 35 (2010) 7957–7970.

[82] G. Hou, J. Parrondo, V. Ramani, J. Prakash, Kinetic and Mechanistic Investigation of Methanol Oxidation on a Smooth Polycrystalline Pt Surface, J. Electrochem. Soc. 161 (2014) F252–F258. https://doi.org/10.1149/2.045403jes.

[83] E. Hao Yu, K. Scott, R.W. Reeve, A study of the anodic oxidation of methanol on Pt in alkaline solutions, J. Electroanal. Chem. 547 (2003) 17–24.

[84] X. Zhao, M. Yin, L. Ma, L. Liang, C. Liu, J. Liao, T. Lu, W. Xing, Recent advances in catalysts for direct methanol fuel cells, Energy Environ. Sci. 4 (2011) 2736. https://doi.org/10.1039/c1ee01307f.

[85] Y. Paik, S.S. Kim, O.H. Han, Methanol Behavior in Direct Methanol Fuel Cells,

Angew. Chemie Int. Ed. 47 (2008) 94–96.

[86] B. Gurau, E.S. Smotkin, Methanol crossover in direct methanol fuel cells: a link between power and energy density, J. Power Sources. 112 (2002) 339–352.

[87] S. Eccarius, B.L. Garcia, C. Hebling, J.W. Weidner, Experimental validation of a methanol crossover model in DMFC applications, J. Power Sources. 179 (2008) 723–733. https://doi.org/10.1016/j.jpowsour.2007.11.102.

[88] D. Malko, T. Lopes, E. Symianakis, A.R. Kucernak, The intriguing poison tolerance of non-precious metal oxygen reduction reaction (ORR) catalysts, J. Mater. Chem. A. 4 (2016) 142–152. https://doi.org/10.1039/C5TA05794A.

[89] A.A. Gewirth, M.S. Thorum, Electroreduction of Dioxygen for Fuel-Cell Applications: Materials and Challenges, Inorg. Chem. 49 (2010) 3557–3566.

[90] R. Dillon, S. Srinivasan, A.S. Aricò, V. Antonucci, International activities in DMFC R&D: status of technologies and potential applications, J. Power Sources. 127 (2004) 112–126. https://doi.org/10.1016/j.jpowsour.2003.09.032.

[91] A. Oedegaard, Characterisation of direct methanol fuel cells under near-ambient conditions, J. Power Sources. 157 (2006) 244–252.

[92] O. Muneeb, I. Chino, A. Saenz, J.L. Haan, An ascorbate fuel cell with carbon black nanoparticles as anode and cathode, J. Power Sources. 413 (2019) 216–221.

[93] S. Uhm, J. Choi, S.T. Chung, J. Lee, Electrochemically oxidized carbon anode in direct l-ascorbic acid fuel cells, Electrochim. Acta. 53 (2007) 1731–1736.

[94] A. Keramati, K. Hendrix, D. Nguyen, F. Gonzales, K. Waters, A. Fry-Petit, J.L. Haan, A non-precious metal ascorbate fuel cell, Int. J. Energy Res. 45 (2021) 1–11. https://doi.org/10.1002/er.6565.

[95] N. Fujiwara, S. Yamazaki, Z. Siroma, T. Ioroi, K. Yasuda, l-Ascorbic acid as an alternative fuel for direct oxidation fuel cells, J. Power Sources. 167 (2007) 32–38. https://doi.org/10.1016/j.jpowsour.2007.02.023.

[96] Y. Zeng, N. Fujiwara, S. Yamazaki, K. Tanimoto, P. Wu, Modelling and analysis of a direct ascorbic acid fuel cell, J. Power Sources. 185 (2008) 95–103.

[97] A. Zalineeva, A. Serov, M. Padilla, U. Martinez, K. Artyushkova, S. Baranton, C. Coutanceau, P.B. Atanassov, Self-Supported PdxBi Catalysts for the Electrooxidation of Glycerol in Alkaline Media, J. Am. Chem. Soc. 136 (2014) 3937–3945. https://doi.org/10.1021/ja412429f.

Chapter 2

Synthesis of Silver Dendrite Nanostructures by Electroless Deposition Method for Ascorbic Acid Electrooxidation

2.1 Abstract

An easy and cost-effective synthesis process is highly desirable for the mass production of hierarchical metal nanostructures that have good electrocatalytic activity. A simple wet chemical electroless deposition technique was developed without the use of surfactant, temperature, and pressure to produce well-defined silver dendritic nanostructures on a glassy carbon electrode (GCE) surface. The silver dendrite nanostructures had primary and secondary branches. The silver nanoparticles played a role as a seed for the formation of unique silver dendrite nanostructures. Scanning electron microscopy (SEM), energy-dispersive X-ray spectroscopy (EDX), X-ray photoelectron spectroscopy (XPS), X-ray powder diffraction (XRD), cyclic voltammetry (CV), and electrochemical impedance spectroscopy (EIS) were used to investigate the characteristics of silver dendritic formations. The XPS and XRD results showed that the dendrite structure was made of metallic silver. The ascorbic acid (AA) electrocatalytic oxidation was quite high in presence of silver dendritic modified GCE (Ag/GCE). The kinetic study revealed that at slower scan rates ($\upsilon < 0.15$ V s^{-1}) the AA oxidation process followed a stepwise mechanism and concerted at higher scan rates ($\upsilon > 0.15$ V s^{-1}).

2.2 Introduction

Metallic nanostructures have emerged as a favorite contender for a wide range of applications. They are used in a variety of electrochemical methods because of their strong catalytical ability with high surface area, which is ideal for improving performance [1]. Silver has a variety of electrical, and chemical characteristics making it a good choice for electrocatalysis [2–5]. Hierarchical dendrite structures of silver have been investigated for various electrochemical applications [6,7]. Non-equilibrium growth circumstances allow hierarchical fractal and dendritic structures to form. Diffusion-limited aggregation and an orientated adhesive mechanism can generate fractals and dendrites [8]. The process of growth and structural development has to be understood completely. For the development of dendritic structures, silver nitrate ($AgNO_3$) is commonly employed as a precursor. The silver dendritic structure has been synthesized using a variety of techniques, including photochemistry [9], sonochemistry [10], and electrochemistry [11,12]. The major driving factors are reductants, high temperatures, and surfactants however, certain reductants are hazardous to humans and the environment [13]. Thus it is quite desirable to have a simple environmentally friendly approach for synthesizing silver dendritic structures.

For a sustainable and ecologically friendly future, alternative energy sources are extremely desirable. As an alternate portable source of energy, a direct liquid fuel cell (DLFC) having a simple design and cell operation is adequate. Recently, researchers have focused on ascorbic acid (AA) for fuel of DLFC in particular due to natural abundance and the production of non-toxic by-products [14–16]. Various approaches, including HPLC [17,18], chromatography [19], spectroscopic [20], and electrochemical methods [21] have been used to investigate for the AA oxidation. Electrochemical

techniques are regarded to be among the best possible options because of their great sensitivity, simplicity, and low cost [22]. However, while developing a DLFC, the reaction kinetics should be investigated in detail. Several investigations of the reaction kinetics of AA electrooxidation have been described in this regard [23–25]. AA, a powerful antioxidant, is typically converted to dehydroascorbic acid (DHA) by the release of two electrons [19,23,26,27]. DHA opens its lactone ring during this electrochemical process, forming electro-inactive 2,3-diketogulonic acid which causes electrode fouling [24,25,28–32]. To address this issue, researchers are utilized silver metal as an electrochemical catalyst [33].

According to several reported research, the carbon-based electrode is well suited for AA electrooxidation due to superior mechanical stability and strong corrosion resistivity [34–40]. Glassy carbon (GC) is a kind of carbon that combines glassy and ceramic characteristics of graphite. Chemicals inertness, high-temperature resiliency, and gas-liquid impermeability make GC more interesting to catalytic scientists [41]. In this chapter, we reported for the first time about the formation of silver dendrite on the glassy carbon electrode (GCE) by electroless deposition technique without using a capping agent, current, temperature, pressure, and applied it for AA electrooxidation. The mechanism of the electroless deposition technique is shown in Figure 2.1. The GCE surface is negatively charged in alkaline condition. The silver ions migrate to the surface of GCE and produce silver nanoparticles (AgNPs). These AgNPs have functioned as seeds where quick nucleation and growth of the AgNPs creates the dendrite nanostructure. Under acidic environments, this deposition is not favorable. The silver dendrite nanostructures have fully developed having primary and secondary branches with leaves. This structure showed good stability on the GCE surface and had high

catalytic activity. In this chapter, we have also discussed the reaction mechanism of AA electrooxidation.

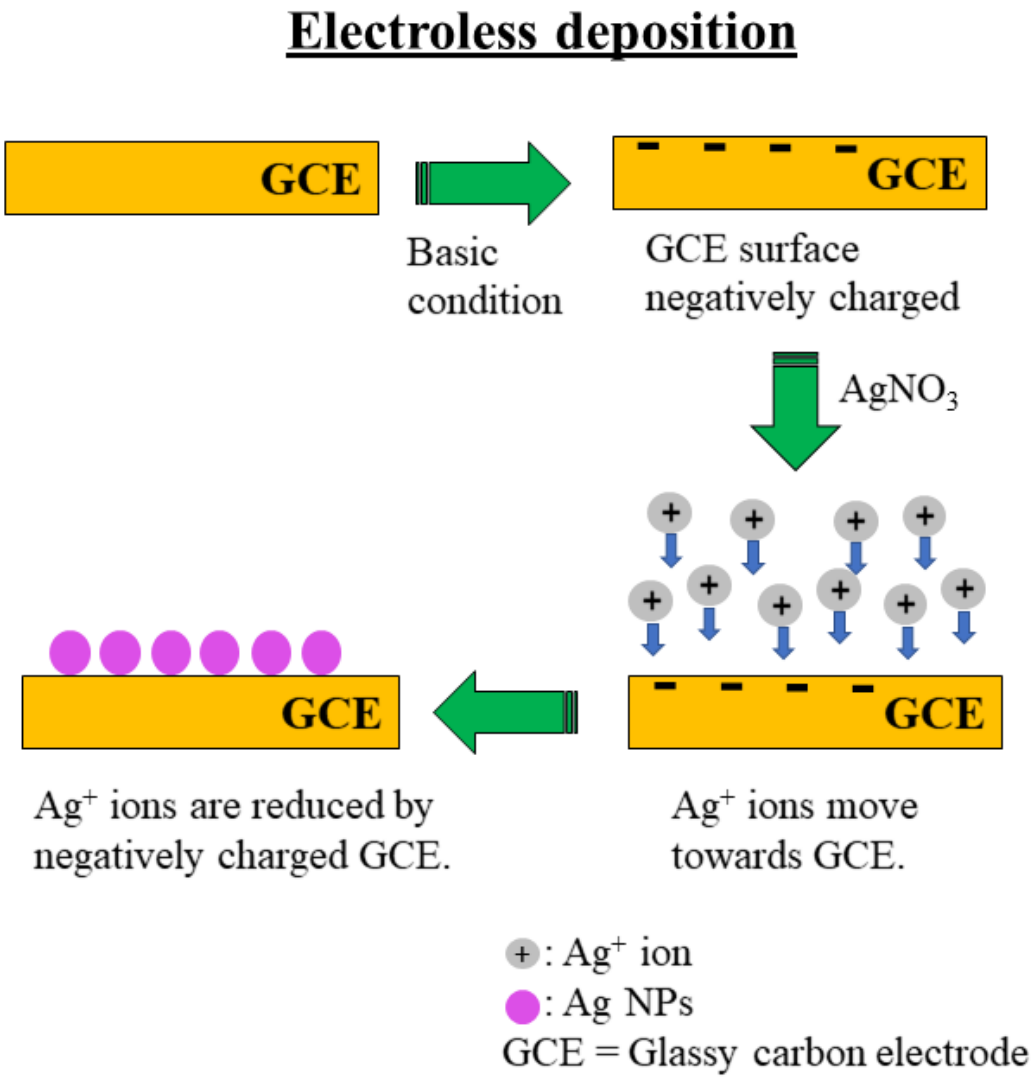

Figure 2.1 Mechanism of silver nanoparticles electroless deposition onto a glassy carbon electrode.

2.3 Experimental

2.3.1 Chemicals and Instruments

The following analytical grade chemicals were purchased from Fujifilm Wako Pure Chemical Corp and used without further purification: sodium chloride (NaCl), AA, disodium hydrogen phosphate (Na_2HPO_4), $AgNO_3$, dipotassium hydrogen phosphate (K_2HPO_4), sodium hydroxide (NaOH), sulfuric acid (H_2SO_4), and hydrochloric acid (HCl). Potassium chloride (KCl) was bought from Kanto Chemical Ltd. All of the required solutions were prepared with Milli-Q water. Every experiment was done in 0.1 M phosphate buffer solution (PBS) having pH 7, deaeration, and room temperature (25°C ± 0.5°C). A combination of KCl (0.1 g), NaCl (4 g), Na_2HPO_4 (0.72 g), and K_2HPO_4 (0.12 g) was dissolved in 500 mL water for PBS solution preparation. HCl_{aq} and $NaOH_{aq}$ have been used to optimize the pH of PBS solution.

2.3.2 Electroless deposition of Silver Dendrite Nanostructures

After mechanical rubbing the GCE surface by 0.05 µm size alumina, ethanol and water were used for sonication separately (10 min). The GCE surface was dried at room temperature after cycling from 0 V to +1.0 V in deaerated H_2SO_4 (0.1 M) solution at 100 mV s^{-1} scan rate. Then, inside a glass cell, equal quantities of $AgNO_3$ (0.1 M), and NaOH (0.1 M) were added. After that, the cleaned GCE (ϕ= 3mm) was kept in the solution with no voltage applied and maintained at room temperature in the dark for 24 hours. As a result, silver particles spontaneously deposited on the GCE surface. Then ethanol and water (1:1, v/v) solution were used to rinse the GCE multiple times.

2.3.3 Characterizations

Scanning electron microscope (SEM) having energy-dispersive x-ray spectroscopy (EDX, TM3030Plus miniscope; Hitachi Ltd.) as well as field-emission scanning electron microscopy were used to examine the silver dendritic structure (FE-SEM, S4100; Hitachi Ltd.). X-ray photoelectron spectroscopy (XPS) measurement was also accomplished by an Al K radiation source (1486.6 eV) with a delay-line detector spectrometer from Kratos Axis-Ultra; Kratos Analytical Ltd. Powder x-ray diffractometer (XRD) was measured as a 2θ range from 20° to 90° on a completely automated horizontal multi-purpose x-ray diffractometer (Rigaku Smartlab; Rigku Corp.). The electrochemical impedance spectra (EIS) and electrochemical data were obtained in a typical three-electrode system by a potentiostat (CHI 701 potentiostat, Autolab PGSTST 128N, Netherlands). The 3 mm diameter GCE, Ag/AgCl (sat. KCl), and a Pt wire were used as working electrode, reference electrode, and counter electrode, respectively.

2.4 Results and Discussion

2.4.1 Morphological and elemental study

FE-SEM images of silver dendrite structure on the GCE surface are shown in Figure 2.2. A dendrite structure is a tree-like structure that has branches. The Ag structure is similar to that so I called it a dendrite structure. Several studies explaining the silver dendrite structure have a morphological pattern with central trunks and secondary branches [29,42]. We have also found a similar structure of silver dendrite [43]. Figure 2.2a displays an overall view of the silver dendritic structure deposited on the GCE. SEM pictures revealed that several branches of the silver dendritic structure are accumulated on the GCE in a well-dispersed manner. The secondary branches of the silver dendrite are visible in Figures 2.2b and 2.2c. Figure 2.2d depicts a section of the fully developed dendrites. With the primary trunk and secondary branches, higher-order branches have appeared as leaves. The primary branch length is around 30 µm (Figure 2.2c), the secondary branch is 4 µm and the leaf is 0.2 µm (Figure 2.2c). The body is nearly straight, having secondary branches growing 60° angle to the primary body. The dendritic structure results from the fast nucleation and subsequent development of AgNPs [3,5,44], as illustrated in Figures 2.2e and 2.2f.

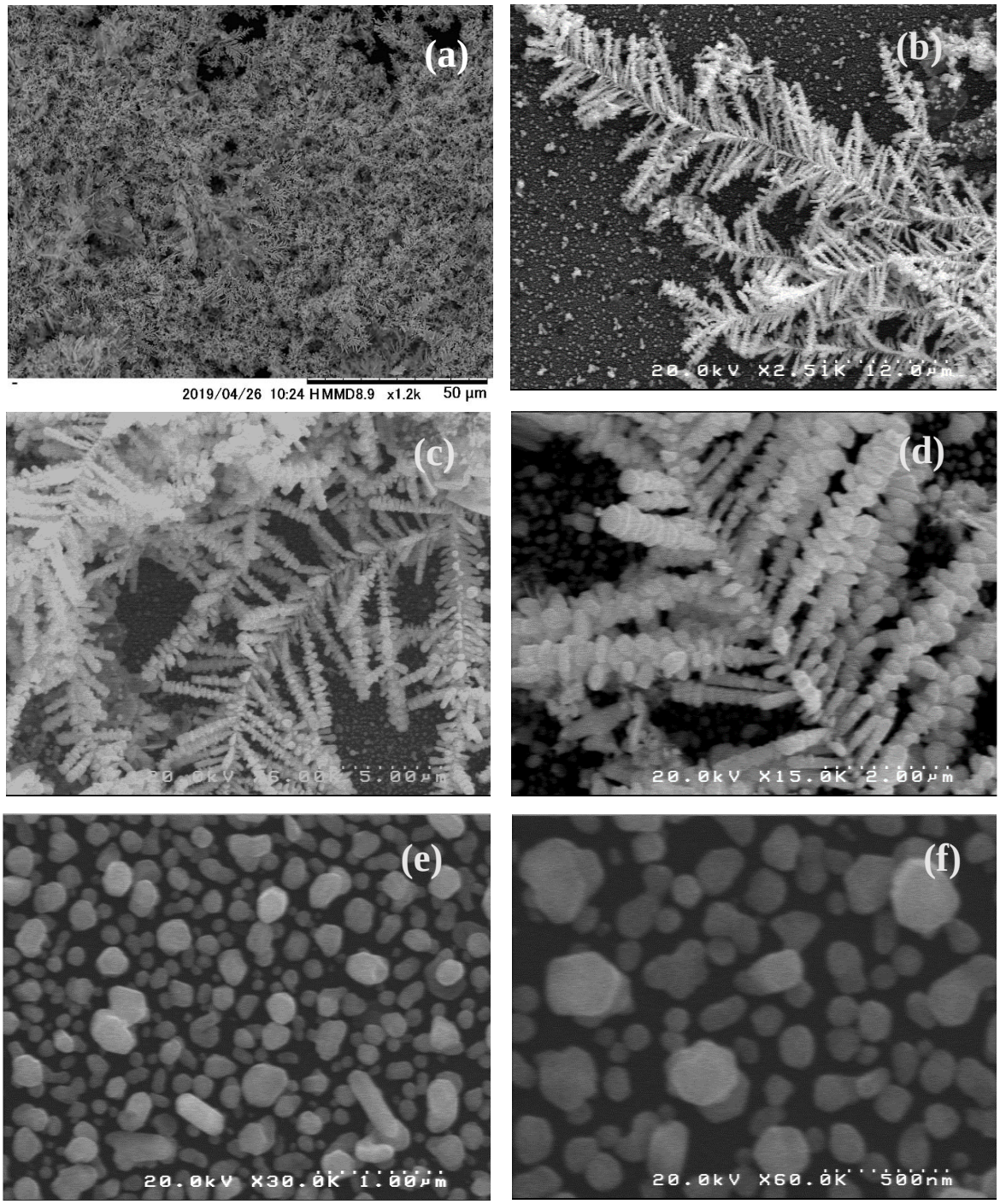

Figure 2.2 FE-SEM images of the (a-d) silver dendrite structure (e,f) deposited silver nanoparticles onto the glassy carbon electrode surface (a-f).

As illustrated in Figure 2.3, the EDX analysis presents the elemental distribution as a 2D map. The EDX result revealed that the dendritic structures have been made up entirely of silver particles. The GCE surface provides the carbon element. A trace quantity of oxygen has been discovered. XPS is an effective method for distinguishing between metallic silver and silver oxide. Silver metal has distinctive characteristics: in the presence of O_2, silver adsorbs oxygen dissociatively rather than producing bulk oxide. Metal oxide has higher binding energy (BE) than the metallic state because of lower valence electron charge density [45]. However, the silver cation shows a negative peak shift in BE as the oxidation state grows [46].

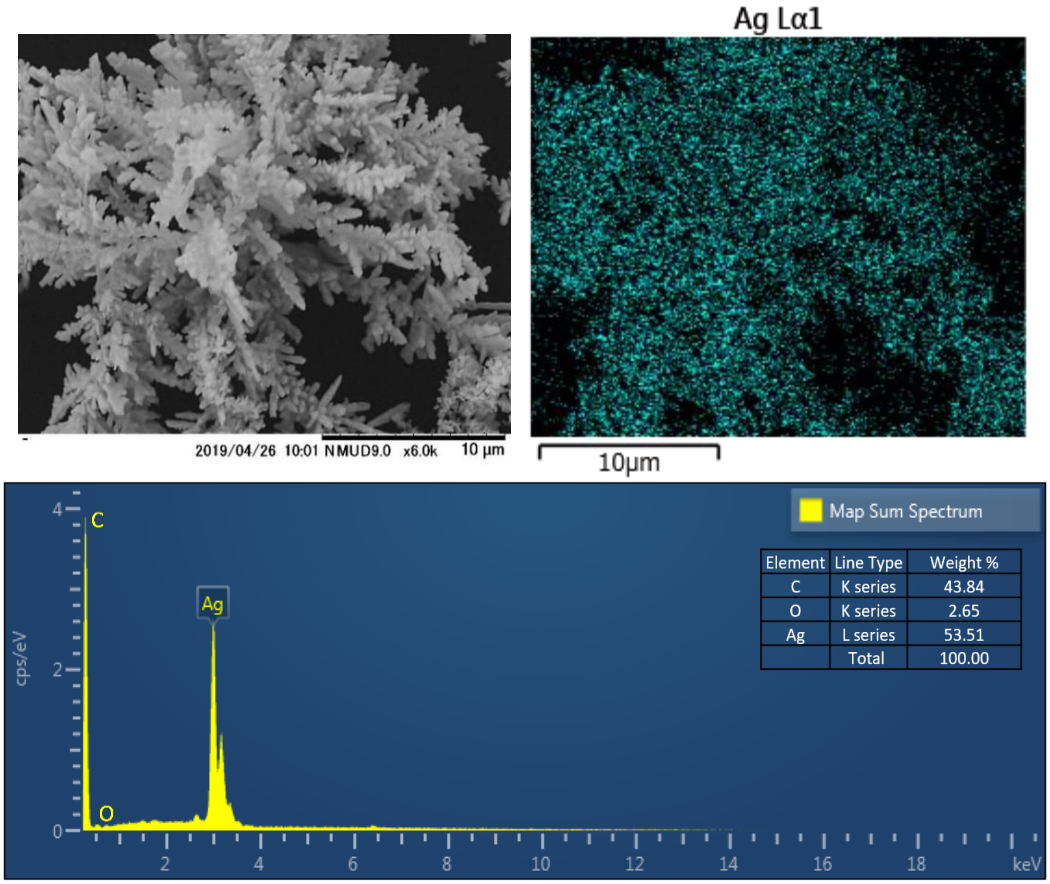

Figure 2.3 EDX elemental analysis of silver dendrite onto the glassy carbon electrode surface.

XPS data of the silver dendrite structure is shown in Figure 2.4a. Two significant peaks are detected at BE of 368.1 eV and 374.1 eV, indicating Ag^0 $3d_{5/2}$ and Ag^0 $3d_{3/2}$, respectively. The 6 eV BE variation between these two peaks is indicating the formation of metallic silver [45–47]. Satellite peak at 371.8 eV BE further confirmed the existence of metallic silver [42,45]. Figure 2.4b shows XRD data that also supports the existence of metallic silver [48]. All the carbon peaks in the XRD analysis are coming from the GCE.

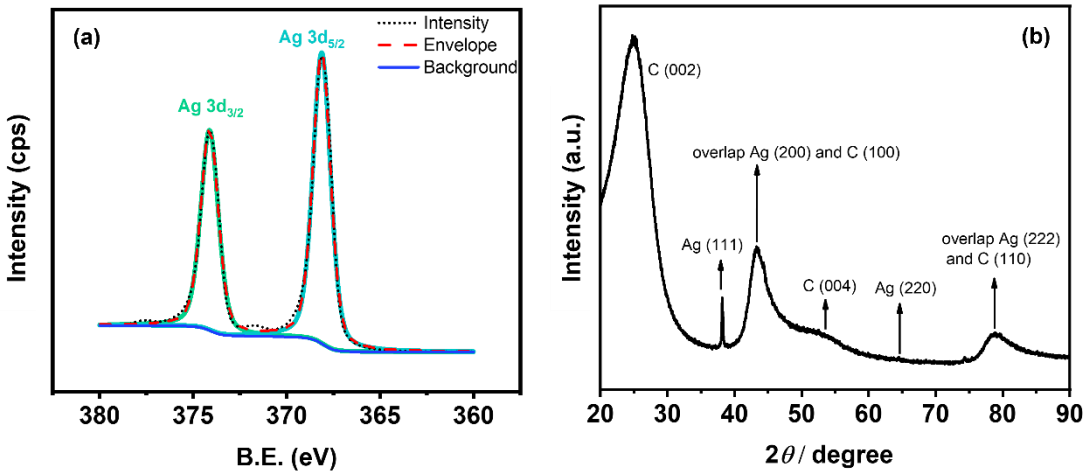

Figure 2.4 (a) The XPS spectra of Ag 3d, and (b) XRD data of silver dendrite on the glassy carbon electrode surface.

2.4.2 Electrochemical characterization

Figure 2.5 exhibits cyclic voltammograms of 0.1 M PBS utilizing GCE and silver dendrite deposited GCE (Ag/GCE) between -0.3 and 0.8 V at a scan rate of 0.1 V s^{-1}. The cyclic voltammogram response displays redox peaks at Ag/GCE. Silver particles on GCE are oxidized at +0.11 V during the positive scan. During the reverse scan, oxidized

silver particles were reduced to the previous condition (Ag^0) at -0.06 V. This characteristic is similar to others described in the literature [48,49]. In the case of bare GCE, such characteristics are absent. Thus it can be concluded that silver particles are successfully deposited on the GCE surface by the electroless process. The relative electronic characteristics of the bare GCE and Ag/GCE surface are investigated via electrochemical impedance spectroscopic (EIS). The EIS study is carried out in a frequency range of 0.1 Hz to 0.1 MHz in presence of AA in 0.1 M PBS by applying 0.25 V. Figure 2.6 shows complex plane plots of 0.1 M PBS containing 2.9 mM AA recorded with bare GCE and Ag/GCE surface. In both electrodes, there is a semicircle in the high-frequency region and a diagonal line with a 45° slope in the low-frequency area shown in Figure 2.6a. It can be said that at the lower frequency range, a diffusional mechanism is combined with a charge transfer process for both electrodes. The equivalent circuit for this process is made up of a series of solution resistances (R_s) with parallel to double-layer capacitances (C_{dl}), charge transfer resistance (R_{ct}), and Warburg impedances (W) [50,51]. In comparison to bare GCE, the reduced diameter of the semicircle in Ag/GCE indicates that the AA electrooxidation is enhanced. The charge transfer behavior of the two electrodes is more clearly revealed by the bode modulus graphs given in Figure 2.6b. There are two breakpoints for both electrodes however, Ag/GCE indicates a sharper breakpoint than that exhibited by bare GCE. The value of R_s, $R_{ct,}$ and C_{dl} can be calculated by corresponding time constants τ_1, and $\tau_{2,}$ at two breakpoints [52].

$$\tau_1 = \frac{1}{\omega_1} = \frac{R_s R_{ct} C_{dl}}{R_s + R_{ct}} \quad (2.1)$$

$$\tau_2 = \frac{1}{\omega_{max}} = R_{ct} C_{dl} \quad (2.2)$$

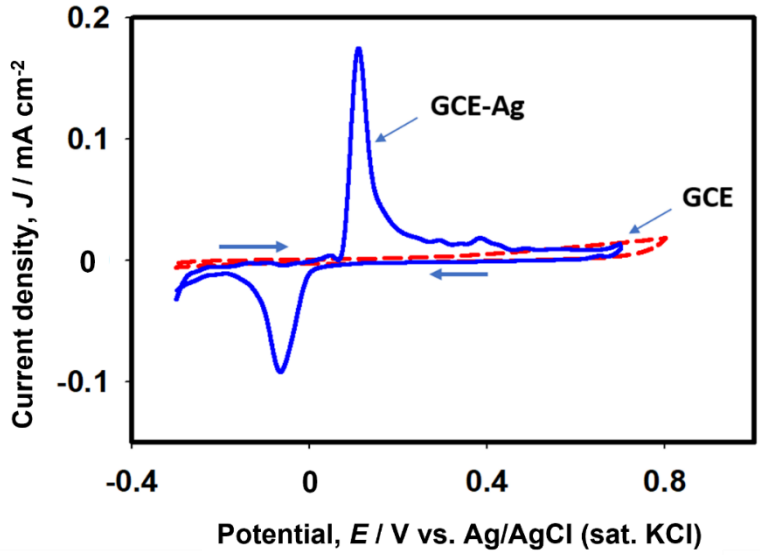

Figure 2.5 Cyclic voltammograms of bare GCE (dotted red line) and Ag/GCE (solid blue line) in 0.1 M PBS (pH 7.0) at scan rate 0.1 V s^{-1}.

The bode-phase plots (Figure 2.6c) also demonstrate similar meanings for the simplified Randle's circuit as those of the bode modulus plots. Table 2.1. explains the EIS characteristics based on the model circuit. The Ag/GCE showed 4.1 kΩ charge transfer resistance (R_{ct}) which is approximately one-third compared to the bare GCE (12.7 kΩ) for the electrooxidation of AA. In comparison with the bare GCE (221 nF), the double-layer capacitance also increased for Ag/GCE electrode (468 nF). As the double layer capacitance increases with the active area, the local charge layer is developed at the modified electrode surface [53]. All of these findings indicate that the Ag/GCE surface can effectively improve the AA electrooxidation process.

Table 2.1 EIS study for bare GCE and Ag/GCE surfaces in 2.9 mM ascorbic acid at 0.1 M PBS (pH 7) with excitation potential, 0.25 V

Electrode	R_s [Ω]	R_{ct} [kΩ]	C_{dl} [nF]
GCE	103	12.7	221
Ag/GCE	113	4.1	468

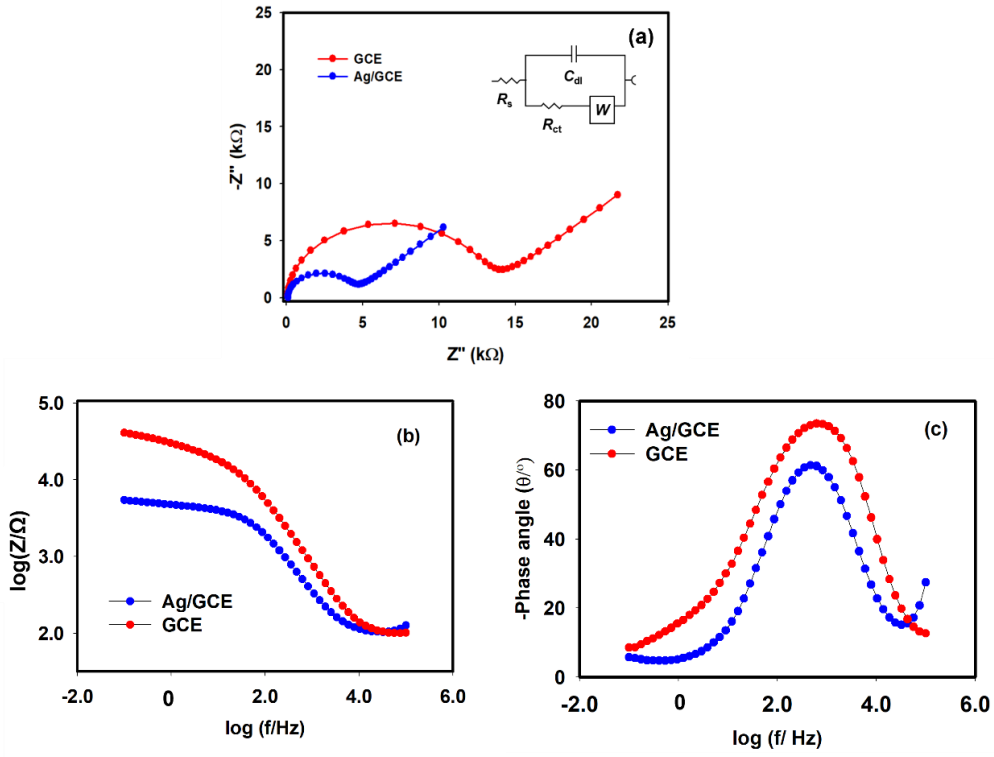

Figure 2.6 EIS spectra in presence of ascorbic acid in neutral pH solution at Ag/GCE and unmodified GCE. (a) Nyquist plots (inset: equivalent circuit), (b) bode modulus plots, and (c) bode phase plots.

Determining the surface concentration of catalytic species is a crucial characteristic when discussing the relationship between electroactive material concentration and electrocatalytic activities. Scan rate dependent study of Ag/GCE in 0.1 M PBS has been

explored for this purpose (Figure 2.7a). The surface concentrations can be estimated using the slope of the I_p vs. scan rate with the equation below [54,55].

$$I_p = \frac{n^2F^2\upsilon A\Gamma}{4RT} \quad (2.3)$$

Here, Γ is the surface concentration of electroactive species in mol cm^{-2}, I_p denotes as peak current (μA), *F* is Faraday constant (C mol^{-1}), *n* is the total electron transfer, *A* denotes the electrode surface area in cm^2, υ means scan rate (mV s^{-1}), *R* stands for gas constant (J K^{-1} mol^{-1}), and *T* is the temperature in K. The estimated surface concentration of silver particles is 1.5×10^{-6} mol cm^{-2} that is higher than previous work [54,55]. This simple electroless deposition technique provides a high concentration of electroactive species for electrocatalysis of AA oxidation.

The fractional dimension (*D*) is a helpful measure for quantifying fractal objects. Thus, the surface morphology of the Ag/GCE electrode was analyzed utilizing the fractal concept for rough surface structure analysis. *D* can be calculated by following equation [56]:

$$\alpha = \frac{D-1}{2} \quad (2.4)$$

Here, *D*=fractal dimension, α=fractal parameter and can be calculated by the slope of log scan rate vs log peak current of Ag/GCE in 0.1 M PBS (Figure 2.7b). The *D* value for Ag dendrite structure is 2.4 using α= 0.7. The *D* value is higher than the previous study of Ag dendrite structures [57].

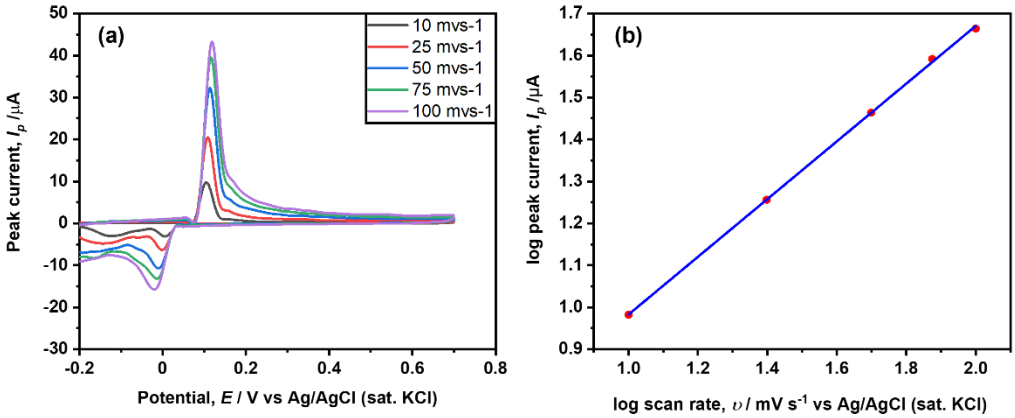

Figure 2.7 (a) Scan rate effect of Ag/GCE in 0.1 M PBS (pH 7.0), (b) log I_p vs log scan rate.

2.4.3 Electrocatalytic Performance and Kinetic Study

Cyclic voltammograms have been obtained in different experimental conditions for elucidating detail of AA electrooxidation utilizing the Ag/GCE. Figure 2.8a shows cyclic voltammograms obtained with Ag/GCE among -0.3 V and 0.7 V in the absence and presence of 2.9 mM AA into 0.1 M PBS at 50 mV s^{-1} scan rate. A well-defined oxidation peak has appeared at +0.20 V in the presence of AA molecules. Figure 2.8b shows cyclic voltammograms of AA molecules using the bare GCE and Ag/GCE to demonstrate the enhancement in the catalytic activity of the AA oxidation process by silver dendrite structure. The AA oxidation current density of the bare GCE is lower than the Ag/GCE. This finding is consistent with the findings of the EIS investigations discussed earlier. Therefore, the Ag/GCE has been conducted for voltammetric studies further. The concentration influence of AA (1.47–8.25 mM) utilizing the Ag/GCE into 0.1 M PBS at 50 mV s^{-1} scan rate is shown in Figure 2.9a. The oxidation current increased as the concentration of AA increasing, and the peak potential also shift positively. With the AA concentration increasing, the Ag^0 oxidation current (+0.11 V) decreased, suggesting

adsorption of AA molecules onto the electrode surface, limiting the Ag^0 oxidation. Figure 2.9b depicts current potential responses during the oxidation of 2.9 mM AA molecules at various scan rates. The Ag and AA oxidation peaks rose in parallel to the increased scan rate. The log peak current (I_p) value changed linearly with log (scan rate) having a slope value of 0.48 (Figure 2.10), close to 0.5, suggesting that the solution to electrode surface mass transfer step controls AA oxidation at the Ag/GCE surface [58].

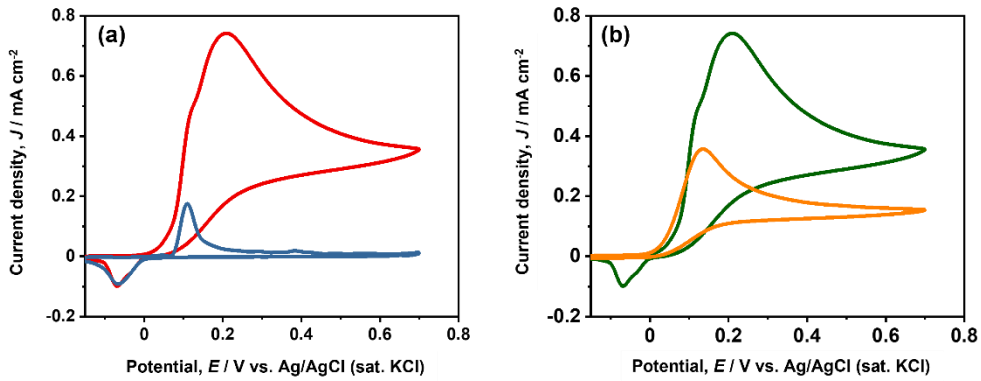

Figure 2.8 (a) Cyclic voltammograms of Ag/GCE in the presence of 2.9 mM ascorbic acid (red line) and absence of ascorbic acid (blue line), (b) catalytic activity comparison between Ag/GCE (green line) and bare GCE (orange line) of 2.9 mM ascorbic acid in 0.1 M PBS having pH 7 at 50 mV s^{-1}.

Though, AA oxidation reaction reflects an absolute irreversible electron transfer if the reaction ratio (Q) stays constant with scan rate, as shown by equations [52].

$$I_p = (2.99 \times 10^5) n\, A\, C\, \beta^{1/2} D^{1/2} \upsilon^{1/2} \qquad (2.5)$$

$$Q = \frac{I_p}{C \times \upsilon^{1/2}} \qquad (2.6)$$

Here, *C* is the AA concentration and *D* denotes the diffusion coefficient of AA. As seen in Figure 2.11, Q does not have a constant value at the slower scan rate. Due to the change of charge transfer coefficient with scan rate, the electron transfer (ET) kinetics is scan-rate dependent. We studied the influence of $\Delta E_{p/2}$ (distinction of peak potential and half peak potential) on scan rate to understand more about the details of ET kinetics. Figure 2.12a shows that when the scan rate increases, $\Delta E_{p/2}$ shifts positively. For a simple irreversible oxidation reaction, the charge transfer coefficient (β) should stay constant as a function of scan rate.

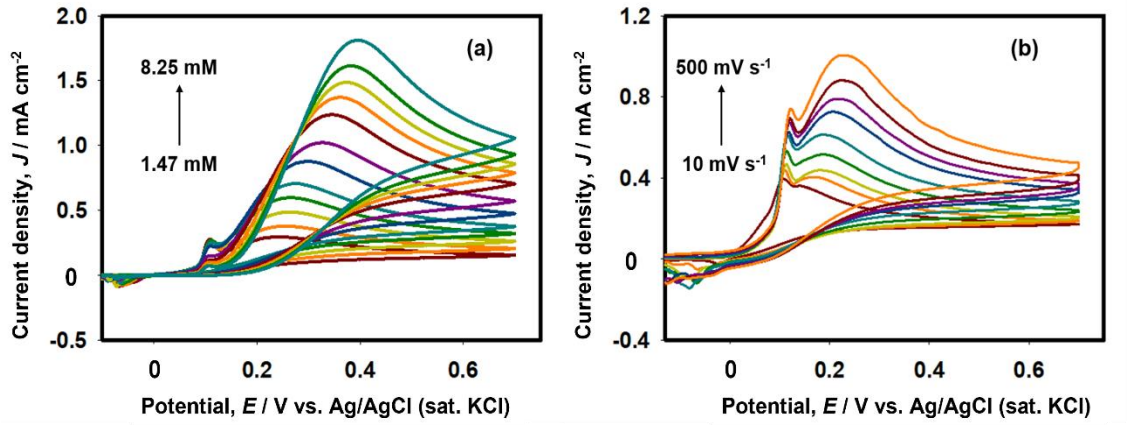

Figure 2.9 (a) Ascorbic acid concentration effect (1.47 mM-8.25 mM) at 50 mV s^{-1} scan rate. (b) The scan rate effect in presence of 2.9 mM ascorbic acid in 0.1 M PBS (pH 7) at Ag/GCE.

The following equation defines the relationship between β and $\Delta E_{p/2}$ [52].

$$\beta = \frac{1.86RT}{F|E_p - E_{p/2}|} \qquad (2.7)$$

Results demonstrate that $\Delta E_{p/2}$ grew along with scan rate (Figure 2.12a) and the β (charge transfer coefficient) value changes negatively (Figure 2.12b). The value of β varied from 0.62 to 0.39 corresponding to increasing scan rate from 10 to 50 mV s^{-1} respectively. A step-wise process is indicated by the value of β greater than 0.5. Smaller values imply that an electron transfer is occurring simultaneously with a chemical process [58,59]. We concluded that the electrooxidation of AA follows a step-by-step process at the slower scan rate (υ < 0.15 V s^{-1}), while concerted mechanisms at the fastest scan rate at the Ag/GCE during the AA oxidation into DHA. The intermediate step is the dissociation

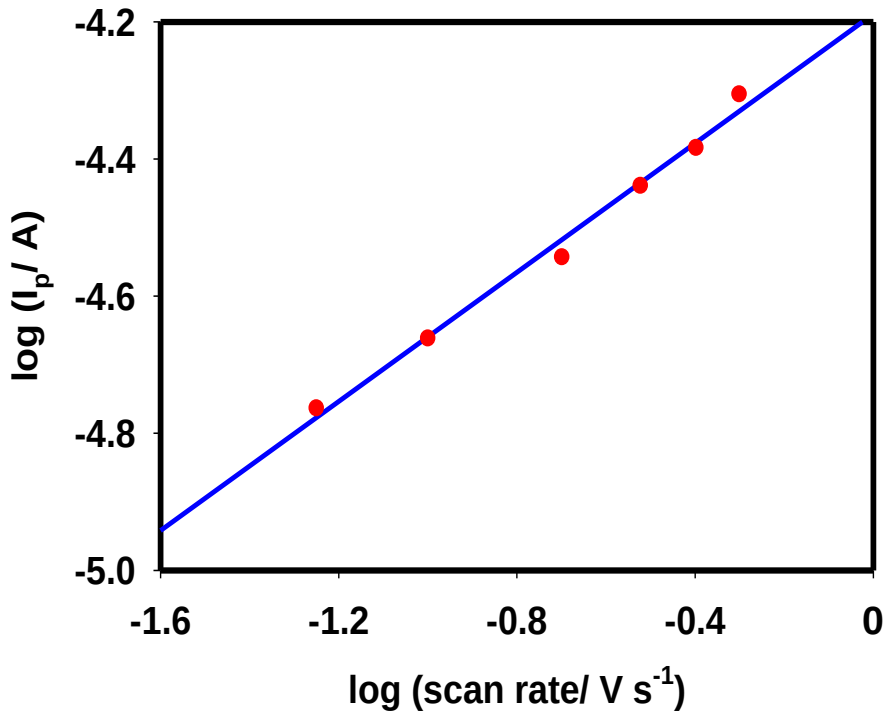

Figure 2.10 The plot of Log (I_p) vs. log (scan rate). Values are taken from the experimental conditions shown in Figure 2.9b.

of one electron, which results in the formation of a radical anion and then one-electron removal to form DHA [24]. Radical formation takes place in the slow scan rate, while no radical formation happened in the faster scan.

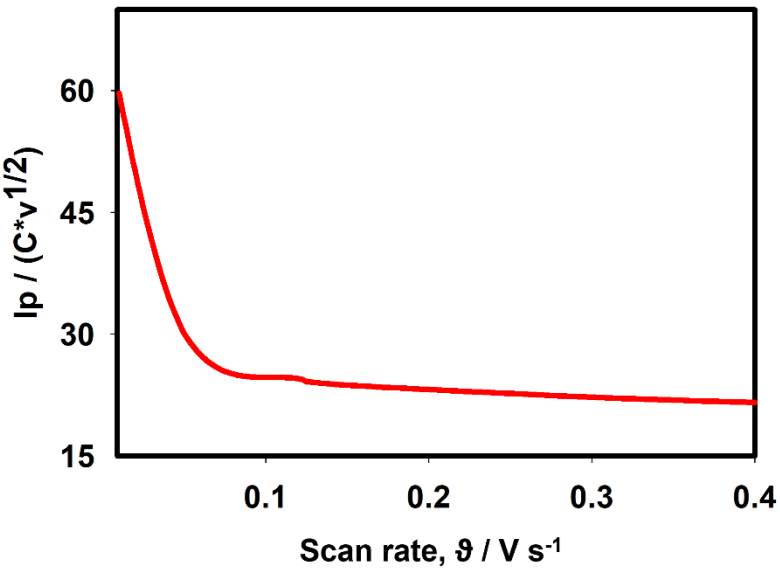

Figure 2.11 Plot of I_p / (C × $\upsilon^{1/2}$) vs scan rate at Ag/GCE. Experimental conditions are the same as Figure 2.9b.

Next, we check the stability of the silver dendrite structure. Chronoamperometry is a good technique for checking electrode stability [60]. The chronoamperometry test for 1000 s has been performed at the peak potential of 0.25 V to verify the stability of the Ag/GCE electrode (Figure 2.13a). After startup, the current curve remains flat even after 1000 s. Figure 2.13b shows the morphology of Ag/GCE following the chronoamperometry test. The silver dendrite nanostructure exhibited almost similar characteristics. The Ag 3d XPS data of the silver dendrite nanostructure is shown in Figure 2.13c following the chronoamperometry test.

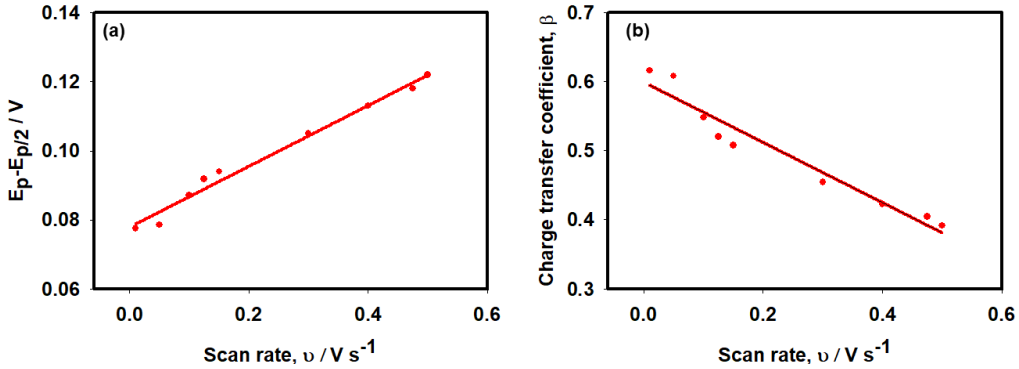

Figure 2.12 Scan rate dependency of (a) $\Delta E_{p/2}$ and (b) corresponding β value using Ag/GCE. Values are taken from experimental conditions described in Figure 2.9b.

The two primary peaks Ag^0 $3d_{5/2}$ and Ag^0 $3d_{3/2}$ have not changed means that the silver dendritic nanostructure remained in a silver metallic condition. Table 2.2 shows the comparison study with previously reported AA electrocatalytic oxidation performance on a silver-modified electrode. The silver dendrite catalyst showed the highest electrocatalytic performance than the previously reported silver-based catalyst for AA electrooxidation.

Table 2.2 Comparison of ascorbic acid electrocatalytic performance by silver modified electrodes

Electrode	Peak current density (μA cm^{-2})	Reference
Ag/GCE	740	This work
Ag/CNT-CPE	75.3	[34]
Ag/CPE	3.4	[61]

Note: CPE=carbon paste electrode, CNT=carbon nanotube

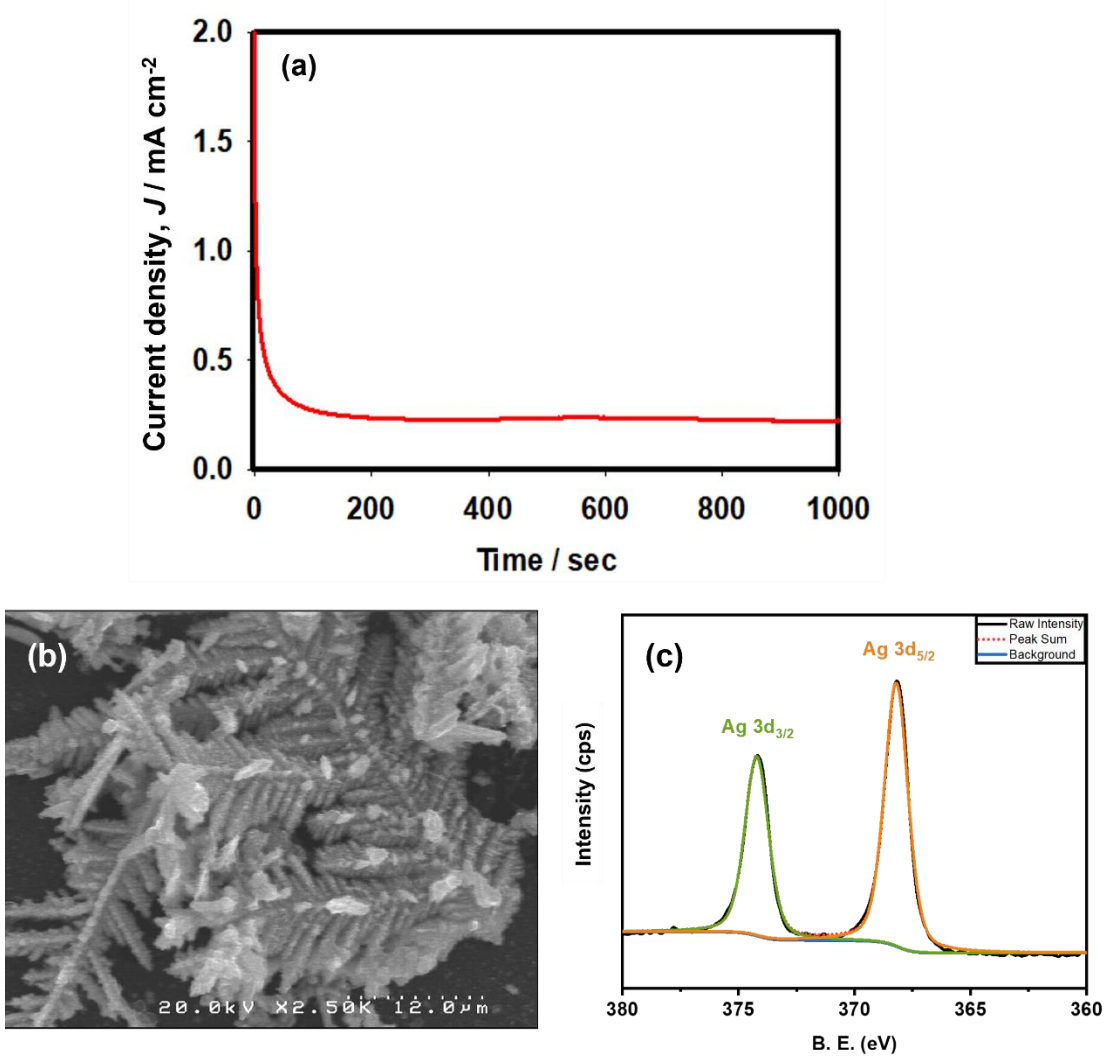

Figure 2.13 (a) Chronoamperogram in presence of 4.8 mM of ascorbic acid at Ag/GCE. Characterization of silver dendrite nanostructures after the Chronoamperometry test (b) FE-SEM image, and (c) Ag 3d XPS spectra.

We also checked the stability of Ag/GCE in presence of 0.9 mM of AA for 50 cycles at 50 mV s^{-1}. The current, potential versus the number of cycles curve is shown in Figure 2.14. The current is a slight decrease in the first several cycles then stabilize. Meanwhile, in terms of oxidation peak positions, the electrode shows highly stable performance.

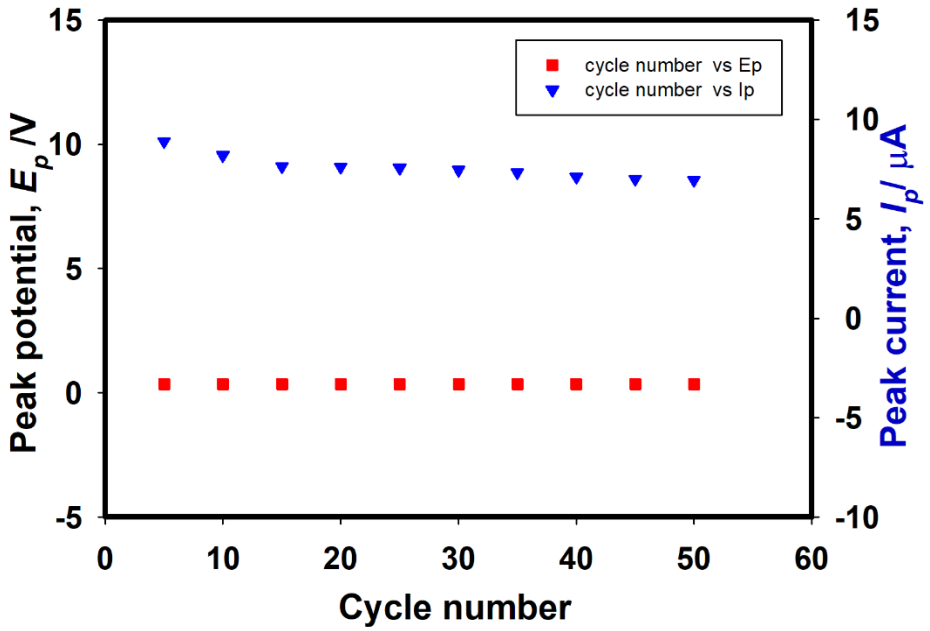

Figure 2.14 Stability check in terms of cycles numbers of Ag/GCE in presence of 0.9 mM of ascorbic acid at 50 mV s^{-1}.

The performance of the AA electrooxidation under alkaline conditions (1 M KOH) was further examined by the Ag dendritic structure (Ag/GCE) to evaluate whether the Ag metal is suitable for the anode catalyst in the alkaline AA-based fuel cell system. Figure 2.15 showed the comparison of the AA electrooxidation in the alkaline solution and the PBS (pH~7) at Ag/GCE. The AA electrocatalytic performance does not enhance in the alkaline condition. The Ag can react with KOH and form Ag_2O. So, the Ag catalyst is not suitable for AA electrooxidation in alkaline conditions.

$$2Ag + 2KOH \rightarrow Ag_2O + H_2O + 2K$$

Thus, an alternative metal catalyst is needed to evaluate the AA electrooxidation performance in the alkaline condition, which will be discussed in the next chapter.

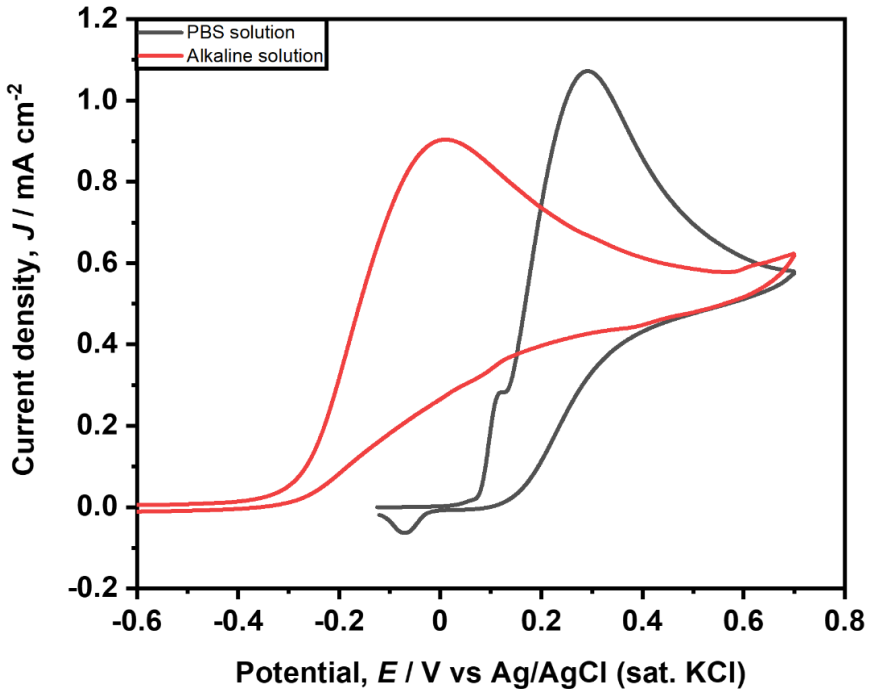

Figure 2.15 Electrochemical performance comparison of 5.6 mM ascorbic acid at Ag/GCE at 50 mV s^{-1} in different pH solutions.

2.5 Conclusion

Stable silver dendritic structures have been devised by a simple electroless deposition technology on a GCE surface. Test results revealed the high catalytic activity of the silver dendrite modified GCE for AA oxidation. The silver dendrite surface concentration is quite high (1.5×10^{-6} mol cm^{-2}) with homogenous coverage on the GCE. The kinetic results showed that the process of oxidation is stepwise with slower scan rates and concerted with faster scan rates. The kinetic study helped us to understand more about the electron transfer process during AA electrooxidation. In the field of catalysis, this novel synthetic technique for silver dendrites formation can play a vital role in the near future.

References

[1] A. Pardakhty, S. Ahmadzadeh, S. Avazpour, V.K. Gupta, Highly sensitive and efficient voltammetric determination of ascorbic acid in food and pharmaceutical samples from aqueous solutions based on nanostructure carbon paste electrode as a sensor, J. Mol. Liq. 216 (2016) 387–391. https://doi.org/10.1016/j.molliq.2016.01.010.

[2] W. Ren, S. Guo, S. Dong, E. Wang, A Simple Route for the Synthesis of Morphology-Controlled and SERS-Active Ag Dendrites with Near-Infrared Absorption, J. Phys. Chem. C. 115 (2011) 10315–10320. https://doi.org/10.1021/jp110532c.

[3] L. Fu, T. Tamanna, W.-J. Hu, A. Yu, Chemical preparation and applications of silver dendrites, Chem. Pap. 68 (2014) 1283–1297. https://doi.org/10.2478/s11696-014-0582-2.

[4] X. Sun, M. Hagner, Novel Preparation of Snowflake-like Dendritic Nanostructures of Ag or Au at Room Temperature via a Wet-Chemical Route, Langmuir. 23 (2007) 9147–9150. https://doi.org/10.1021/la701519x.

[5] L. Wang, H. Li, J. Tian, X. Sun, Monodisperse, Micrometer-Scale, Highly Crystalline, Nanotextured Ag Dendrites: Rapid, Large-Scale, Wet-Chemical Synthesis and Their Application as SERS Substrates, ACS Appl. Mater. Interfaces. 2 (2010) 2987–2991. https://doi.org/10.1021/am100968j.

[6] J. Huang, S. Vongehr, S. Tang, H. Lu, J. Shen, X. Meng, Ag Dendrite-Based Au/Ag Bimetallic Nanostructures with Strongly Enhanced Catalytic Activity, Langmuir. 25 (2009) 11890–11896. https://doi.org/10.1021/la9015383.

[7] X. Wen, Y. Xie, W.C. Mak, K.Y. Cheung, X. Li, R. Renneberg, S. Yang, Dendritic Nanostructures of Silver: Facile Synthesis, Structural Characterizations, and Sensing Applications, Langmuir. 22 (2006) 4836–4842. https://doi.org/10.1021/la060267x.

[8] S. Xie, X. Zhang, D. Xiao, M.C. Paau, J. Huang, M.M.F. Choi, Fast Growth Synthesis of Silver Dendrite Crystals Assisted by Sulfate Ion and Its Application for Surface-Enhanced Raman Scattering, J. Phys. Chem. C. 115 (2011) 9943–9951. https://doi.org/10.1021/jp201484r.

[9] K. Zou, X.H. Zhang, X.F. Duan, X.M. Meng, S.K. Wu, Seed-mediated synthesis of silver nanostructures and polymer/silver nanocables by UV irradiation, J. Cryst. Growth. 273 (2004) 285–291. https://doi.org/10.1016/j.jcrysgro.2004.08.016.

[10] X.-K. Wang, L. Shao, W.-L. Guo, J.-G. Wang, Y.-P. Zhu, C. Wang, Synthesis of dendritic silver nanostructures by means of ultrasonic irradiation, Ultrason. Sonochem. 16 (2009) 747–751. https://doi.org/10.1016/j.ultsonch.2009.03.005.

[11] C. Gu, T. Zhang, Electrochemical Synthesis of Silver Polyhedrons and Dendritic Films with Superhydrophobic Surfaces, Langmuir. 24 (2008) 12010–12016. https://doi.org/10.1021/la802354n.

[12] S. Tang, X. Meng, H. Lu, S. Zhu, PVP-assisted sonoelectrochemical growth of silver nanostructures with various shapes, Mater. Chem. Phys. 116 (2009) 464–468. https://doi.org/10.1016/j.matchemphys.2009.04.004.

[13] X. Zhang, R. Ji, L. Wang, L. Yu, J. Wang, B. Geng, G. Wang, Controllable synthesis of silver nanodendrites on copper rod and its application to hydrogen peroxide and glucose detection, CrystEngComm. 15 (2013) 1173–1178. https://doi.org/10.1039/C2CE26255J.

[14] M.C. Devendrachari, R. Thimmappa, Z.M. Bhat, S.P. Shafi, H.M. Nimbegondi Kotresh, A.R. Kottaichamy, K.R. Venugopala Reddy, M.O. Thotiyl, A vitamin C fuel cell with a non-bonded cathodic interface, Sustain. Energy Fuels. 2 (2018) 1813–1819. https://doi.org/10.1039/C8SE00221E.

[15] O. Muneeb, E. Do, T. Tran, D. Boyd, M. Huynh, G. Ghosn, J.L. Haan, A direct ascorbate fuel cell with an anion exchange membrane, J. Power Sources. 351 (2017) 74–78. https://doi.org/10.1016/j.jpowsour.2017.03.068.

[16] M. Choun, H.J. Lee, J. Lee, Positively charged carbon electrocatalyst for enhanced power performance of L-ascorbic acid fuel cells, J. Energy Chem. 25 (2016) 793–797. https://doi.org/10.1016/j.jechem.2016.05.006.

[17] A. Rizzolo, A. Brambilla, S. Valsecchi, P. Eccher-Zerbini, Evaluation of sampling and extraction procedures for the analysis of ascorbic acid from pear fruit tissue, Food Chem. 77 (2002) 257–262. https://doi.org/10.1016/S0308-8146(02)00107-3.

[18] H. Iwase, Use of nucleic acids in the mobile phase for the determination of ascorbic acid in foods by high-performance liquid chromatography with electrochemical detection, J. Chromatogr. A. 881 (2000) 327–330. https://doi.org/10.1016/S0021-9673(00)00057-1.

[19] E.J. Oliveira, D.G. Watson, Chromatographic techniques for the determination of putative dietary anticancer compounds in biological fluids, J. Chromatogr. B. 764 (2001) 3–25. https://doi.org/10.1016/S0378-4347(01)00401-7.

[20] O.A. Zaporozhets, E.A. Krushinskaya, Determination of ascorbic acid by molecular spectroscopic techniques, J. Anal. Chem. 57 (2002) 286–297. https://doi.org/10.1023/A:1014938011955028 6.

[21] Y.G. Lee, B.X. Liao, Y.C. Weng, Ruthenium oxide modified nickel electrode for ascorbic acid detection, Chemosphere. 173 (2017) 512–519. https://doi.org/10.1016/j.chemosphere.2017.01.086.

[22] G. Wu, Y. Wu, X. Liu, M. Rong, X. Chen, X. Chen, An electrochemical ascorbic acid sensor based on palladium nanoparticles supported on graphene oxide, Anal. Chim. Acta. 745 (2012) 33–37. https://doi.org/10.1016/j.aca.2012.07.034.

[23] S. Kuss, R.G. Compton, Electrocatalytic detection of ascorbic acid using N,N,N',N'-tetramethyl-para-phenylene-diamine (TMPD) mediated oxidation at unmodified gold electrodes; reaction mechanism and analytical application, Electrochim. Acta. 242 (2017) 19–24. https://doi.org/10.1016/j.electacta.2017.05.003.

[24] I.F. Hu, T. Kuwana, Oxidative mechanism of ascorbic acid at glassy carbon electrodes, Anal. Chem. 58 (1986) 3235–3239. https://doi.org/10.1021/ac00127a069.

[25] F. Prieto, B.A. Coles, R.G. Compton, Mechanistic Determination Using Arrays of Variable-Sized Channel Microband Electrodes: The Oxidation of Ascorbic Acid in Aqueous Solution, J. Phys. Chem. B. 102 (1998) 7442–7447. https://doi.org/10.1021/jp982080n.

[26] N. Fujiwara, S. Yamazaki, Z. Siroma, T. Ioroi, K. Yasuda, Direct oxidation of l-ascorbic acid on a carbon black electrode in acidic media and polymer electrolyte fuel cells, Electrochem. Commun. 8 (2006) 720–724. https://doi.org/10.1016/j.elecom.2006.02.021.

[27] S.J. Padayatty, A. Katz, Y. Wang, P. Eck, O. Kwon, J.-H. Lee, S. Chen, C. Corpe, A. Dutta, S.K. Dutta, M. Levine, Vitamin C as an Antioxidant: Evaluation of Its

Role in Disease Prevention, J. Am. Coll. Nutr. 22 (2003) 18–35. https://doi.org/10.1080/07315724.2003.10719272.

[28] M. Zhang, K. Liu, L. Xiang, Y. Lin, L. Su, L. Mao, Carbon Nanotube-Modified Carbon Fiber Microelectrodes for In Vivo Voltammetric Measurement of Ascorbic Acid in Rat Brain, Anal. Chem. 79 (2007) 6559–6565. https://doi.org/10.1021/ac0705871.

[29] J.J. Ruiz, A. Aldaz, M. Dominguez, Mechanism of L-ascorbic acid oxidation and dehydro- L-ascorbic acid reduction on a mercury electrode. I. Acid medium, Can. J. Chem. 55 (1977) 2799–2806. https://doi.org/10.1139/v77-389.

[30] M. Rueda, A. Aldaz, F. Sanchez-Burgos, Oxidation of L-ascorbic acid on a gold electrode, Electrochim. Acta. 23 (1978) 419–424. https://doi.org/10.1016/0013-4686(78)87040-6.

[31] C.R. Raj, K. Tokuda, T. Ohsaka, Electroanalytical applications of cationic self-assembled monolayers: square-wave voltammetric determination of dopamine and ascorbate, Bioelectrochemistry. 53 (2001) 183–191. https://doi.org/10.1016/S0302-4598(00)00129-X.

[32] C.R. Raj, T. Ohsaka, Electroanalysis of ascorbate and dopamine at a gold electrode modified with a positively charged self-assembled monolayer, J. Electroanal. Chem. 496 (2001) 44–49. https://doi.org/10.1016/S0022-0728(00)00335-1.

[33] F.A. Harraz, M. Faisal, A.E. Al-Salami, A.M. El-Toni, A.A. Almadiy, S.A. Al-Sayari, M.S. Al-Assiri, Silver nanoparticles decorated stain-etched mesoporous silicon for sensitive, selective detection of ascorbic acid, Mater. Lett. 234 (2019) 96–100. https://doi.org/10.1016/j.matlet.2018.09.076.

[34] J. Tashkhourian, M.R.H. Nezhad, J. Khodavesi, S. Javadi, Silver nanoparticles modified carbon nanotube paste electrode for simultaneous determination of dopamine and ascorbic acid, J. Electroanal. Chem. 633 (2009) 85–91. https://doi.org/10.1016/j.jelechem.2009.04.028.

[35] G. Karim-Nezhad, M. Hasanzadeh, L. Saghatforoush, N. Shadjou, B. Khalilzadeh, S. Ershad, Electro-oxidation of ascorbic acid catalyzed on cobalt hydroxide-modified glassy carbon electrode, J. Serbian Chem. Soc. 74 (2009) 581–593. https://doi.org/10.2298/JSC0905581K.

[36] L. Xi, D. Ren, J. Luo, Y. Zhu, Electrochemical analysis of ascorbic acid using copper nanoparticles/polyaniline modified glassy carbon electrode, J. Electroanal. Chem. 650 (2010) 127–134. https://doi.org/10.1016/j.jelechem.2010.08.014.

[37] M.A. Alonso-Lomillo, O. Domínguez-Renedo, A. Saldaña-Botín, M.J. Arcos-Martínez, Determination of ascorbic acid in serum samples by screen-printed carbon electrodes modified with gold nanoparticles, Talanta. 174 (2017) 733–737. https://doi.org/10.1016/j.talanta.2017.07.015.

[38] B.R. Sathe, A scalable and facile synthesis of carbon nanospheres as a metal free electrocatalyst for oxidation of l -ascorbic acid: Alternate fuel for direct oxidation fuel cells, J. Electroanal. Chem. 799 (2017) 609–616. https://doi.org/10.1016/j.jelechem.2017.03.049.

[39] X. Zhang, S. Yu, W. He, H. Uyama, Q. Xie, L. Zhang, F. Yang, Electrochemical sensor based on carbon-supported $NiCoO_2$ nanoparticles for selective detection of ascorbic acid, Biosens. Bioelectron. 55 (2014) 446–451. https://doi.org/10.1016/j.bios.2013.12.046.

[40] B.K. Chethana, Y. Arthoba Naik, Electrochemical oxidation and determination of

ascorbic acid present in natural fruit juices using a methionine modified carbon paste electrode, Anal. Methods. 4 (2012) 3754. https://doi.org/10.1039/c2ay25528f.

[41] M. Hassler, Other commonly used biomedical coatings: Pyrolytic carbon coatings, Coatings Biomed. Appl. (2012) 75–105.

[42] N.J. Firet, M.A. Blommaert, T. Burdyny, A. Venugopal, D. Bohra, A. Longo, W.A. Smith, Operando EXAFS study reveals presence of oxygen in oxide-derived silver catalysts for electrochemical CO2 reduction, J. Mater. Chem. A. 7 (2019) 2597–2607. https://doi.org/10.1039/C8TA10412C.

[43] M.M. Hasan, R.H. Rakib, M.A. Hasnat, Y. Nagao, Electroless Deposition of Silver Dendrite Nanostructure onto Glassy Carbon Electrode and Its Electrocatalytic Activity for Ascorbic Acid Oxidation, ACS Appl. Energy Mater. 3 (2020) 2907–2915. https://doi.org/10.1021/acsaem.9b02513.

[44] G. Zhang, S. Sun, M.N. Banis, R. Li, M. Cai, X. Sun, Morphology-Controlled Green Synthesis of Single Crystalline Silver Dendrites, Dendritic Flowers, and Rods, and Their Growth Mechanism, Cryst. Growth Des. 11 (2011) 2493–2499. https://doi.org/10.1021/cg200256j.

[45] T.C. Kaspar, T. Droubay, S.A. Chambers, P.S. Bagus, Spectroscopic Evidence for Ag(III) in Highly Oxidized Silver Films by X-ray Photoelectron Spectroscopy, J. Phys. Chem. C. 114 (2010) 21562–21571. https://doi.org/10.1021/jp107914e.

[46] G. Schön, J. Tummavuori, B. Lindström, C.R. Enzell, C.R. Enzell, C.-G. Swahn, ESCA Studies of Ag, Ag_2O and AgO., Acta Chem. Scand. 27 (1973) 2623–2633.

[47] D. Breitwieser, M.M. Moghaddam, S. Spirk, M. Baghbanzadeh, T. Pivec, H. Fasl, V. Ribitsch, C.O. Kappe, In situ preparation of silver nanocomposites on

cellulosic fibers – Microwave vs. conventional heating, Carbohydr. Polym. 94 (2013) 677–686. https://doi.org/10.1016/j.carbpol.2013.01.077.

[48] B. Kaur, T. Pandiyan, B. Satpati, R. Srivastava, Simultaneous and sensitive determination of ascorbic acid, dopamine, uric acid, and tryptophan with silver nanoparticles-decorated reduced graphene oxide modified electrode, Colloids Surfaces B Biointerfaces. 111 (2013) 97–106.

[49] M.E. Hafez, H. Ma, Y.-Y. Peng, W. Ma, Y.-T. Long, Correlated Anodic–Cathodic Nanocollision Events Reveal Redox Behaviors of Single Silver Nanoparticles, J. Phys. Chem. Lett. 10 (2019) 3276–3281.

[50] B. A. Lasia, Electrochemical Impedance Spectroscopy and Its Applications, in Modern Aspects of Electrochemistry, in: Springer, New York, 2002: pp. 143–248. http://pirg.ch.pw.edu.pl/instrukcje/eis_extensive_introduction.pdf.

[51] L.R.F.A.J. Bard, Electrochemical methods: fundamentals and applications, in: 2nd Ed., Wiley, New York, 2001: pp. 1–864. https://doi.org/10.1002/1521.

[52] M.A. Hasnat, M.M. Hasan, N. Tanjila, M.M. Alam, M.M. Rahman, pH dependent kinetic insights of electrocatalytic arsenite oxidation reactions at Pt surface, Electrochim. Acta. 225 (2017) 105–113.

[53] R. Ahmed, K. Reifsnider, Study of Influence of Electrode Geometry on Impedance Spectroscopy, Int. J. Electrochem. Sci. 6 (2011) 1159–1174.

[54] R. Ji, L. Wang, L. Yu, B. Geng, G. Wang, X. Zhang, Effective Electrocatalysis Based on Ag_2O Nanowire Arrays Supported on a Copper Substrate, ACS Appl. Mater. Interfaces. 5 (2013) 10465–10472. https://doi.org/10.1021/am4016523.

[55] M. Noroozifar, M. Khorasani-Motlagh, A. Taheri, Preparation of silver hexacyanoferrate nanoparticles and its application for the simultaneous

determination of ascorbic acid, dopamine and uric acid, Talanta. 80 (2010) 1657–1664. https://doi.org/10.1016/j.talanta.2009.10.005.

[56] L. Fotouhi, N. Fathali, A. Ehsani, ZnO/Polytyramine nanocomposite film: Facile electrosynthesis and high performance electrocatalytic activity toward methanol oxidation, Int. J. Hydrogen Energy. 43 (2018) 6987–6996.

[57] J. Fang, H. You, P. Kong, Y. Yi, X. Song, B. Ding, Dendritic Silver Nanostructure Growth and Evolution in Replacement Reaction, Cryst. Growth Des. 7 (2007) 864–867. https://doi.org/10.1021/cg0604879.

[58] M.A. Hasnat, Z. Mumtarin, M.M. Rahman, Electrocatalytic reduction of hydroxylamine on copper immobilized platinum surface: Heterogeneous kinetics and sensing performance, Electrochim. Acta. 318 (2019) 486–495.

[59] A. Muthukrishnan, V. Boyarskiy, M. V. Sangaranarayanan, I. Boyarskaya, Mechanism and Regioselectivity of the Electrochemical Reduction in Polychlorobiphenyls (PCBs): Kinetic Analysis for the Successive Reduction of Chlorines from Dichlorobiphenyls, J. Phys. Chem. C. 116 (2012) 655–664.

[60] D.F. Silva, A.O. Neto, E.S. Pino, M. Linardi, E. V. Spinacé, Preparation of PtSn/C electrocatalysts using electron beam irradiation, in: Stud. Surf. Sci. Catal., 2010: pp. 555–558. https://doi.org/10.1016/S0167-2991(10)75107-7.

[61] M.A. Khalilzadeh, M. Borzoo, Green synthesis of silver nanoparticles using onion extract and their application for the preparation of a modified electrode for determination of ascorbic acid, J. Food Drug Anal. 24 (2016) 796–803.

Chapter 3

Electrochemically deposited Christmas-tree-shaped Palladium Nanostructures for Ascorbic Acid Electrooxidation in Alkaline Medium

3.1 Abstract

Nobel metals are frequently employed in electrochemical processes because of their superior catalytic properties. Non-Pt-based noble metals have recently become an important alternative in research. Palladium (Pd) is a popular choice for electrocatalytic processes because of its excellent catalytic capability. The hierarchical structure of the Pd catalysts could greatly improve electrochemical performance. In this chapter, Pd nanostructures in the shape of a hierarchical Christmas tree were created on a glassy carbon electrode (GCE) surface using a simple one-step electrodeposition technique with no additives. The applied voltage, deposition duration, and precursor concentration were optimized to produce hierarchical nanostructures. In alkaline conditions, the Pd nanostructures in form of Christmas trees showed excellent catalytic activity for electrooxidation of ascorbic acid (AA). The modified electrode showed 4.5 mA cm^{-2} current density: significantly higher than unmodified GCE (0.6 mA cm^{-2}). The easy electrodeposition approach is intended to give new insights into several study fields employing Pd-based nanostructured surfaces.

3.2 Introduction

The reaction kinetics study in the previous chapter helped us to understand the electron transfer during AA electrooxidation. For the further improvement of the catalytical performance in the alkaline condition, noble Pd-based catalysts will be explored in this chapter. Another simple deposition technique is developed for the unique hierarchical Pd catalyst preparation. From this chapter, the morphological effect of a catalyst towards AA electrooxidation will be evaluated.

Nanostructured metal surfaces have unique physical and chemical characteristics, and their use in heterogeneous catalysis, biosensors, and electrocatalysis has sparked researchers' attention [1–3]. The manufacturing process controlled the size, and shape of metal nanostructures. Thus, the production of well-defined nanostructures has gained a lot of interest nowadays [4–8]. Several synthesis techniques for metal nanostructures have been successfully established and applied to various applications. But the manufacturing process needs numerous stages with linker molecules [9]. The linker molecule has a potential impact on morphology and electrocatalytic activities [10]. Thus the preparation of metal nanostructures without using linkers molecules gained much attention.

The electrochemical deposition technique offered a synthesis of clean metal nanostructures[11]. Electrochemical deposition methods have been utilized to create various metal nanostructures on diverse substrates, especially on a glassy carbon electrode (GCE) surface [12,13]. Due to chemical inertness, impermeability of gasses, liquids, and high-temperature resistance, GCE is frequently used for electrochemical deposition for metal nanostructures fabrication [14]. In certain cases, pre-modification

of GCE electrodes or electrolyte additives is required for the preparation of metal nanostructures by electrochemical deposition technique [15]. Thus one-pot easy electrodeposition approach is obtaining awareness for the production of clean metal nanostructures to avoid the effects of additives or surfactants in analytical and electrochemical applications [16].

Palladium (Pd) has sparked a lot of interest in the field of heterogeneous catalysis, due to its strong catalytic activity. The formation of Pd nanostructures via electrodeposition on various substrates has been studied recently. Controlled electrodeposition on an indium tin oxide (ITO) electrode had created unique flower-shaped Pd nanostructures [17]. Employing ethylenediamine as an additive, Pd nanodendrites were formed on the GCE surface by electrodeposition [18]. Recently, different Pd nanostructures were created via the electrodeposition technique without any additives. There have been reports of Pd dendrites [19] and Pd urchins [20] onto ITO electrode; Pd nanoflake [1], and Pd triangular rod structures [7] onto Au electrode; Pd nanothorns [21,22] on the carbon surface. The electrocatalytic performance of these Pd nanostructures was excellent. Therefore, the fabrication of different morphological Pd nanostructures is important to increase electrochemical efficiency.

Researchers have concentrated on sustainable energy resources like electrochemical energy conversion and storage devices to solve environmental problems[23–28]. Fuel cells have a lot of potential as zero-emission energy conversion devices [29–32]. Despite the development of different types of fuel cells like alcohol, hydrogen, hydrazine, etc, commercial viability stays doubtful due to concerns of storage, safety, environment [33–36]. Ascorbic acid (AA) might be used as a fuel in direct liquid fuel cells (DLFC) to

address these challenges. AA generates harmless byproducts, releases two electrons, and forms dehydroascorbic acid after oxidation (DHA) [37–41]. The catalytic performance of AA electrooxidation is important to the performance of the AA-based DLFC. The Pd is a promising catalyst for improving AA electrooxidation. Recent research has found that Pd catalyst has high a capability for AA electrocatalysis [42–44]. Pd has greater AA electrooxidation in the alkaline condition than the acidic one [45]. Therefore, it is necessary to examine the Pd nanostructure morphological influence on the catalytic activity of AA electrooxidation in alkaline condition.

In this chapter, Pd nanostructures have developed onto GCE via the constant potential mode electrodeposition technique without utilizing any additives or substrate pre-modification. The Pd nanostructures are described as Christmas-tree-shaped [46]. I have optimized the fabrication process of these unique nanostructures. In the alkaline condition, the catalytic activity of AA electrooxidation has been tested by Christmas-tree-shaped Pd nanostructures deposited GCE. The Pd morphological impacts, as well as Pd mass activities on the catalytic activity of AA electrooxidation under alkaline conditions, have been also investigated.

3.3 Experimental

3.3.1 Chemicals and Instruments

Analytical grade sodium tetrachloropalladate (II) (Na_2PdCl_4), ascorbic acid (AA), sulfuric acid (H_2SO_4), and potassium hydroxide (KOH) were purchased from Fujifilm Wako Pure Chemical Corp and used without further modifications. Milli-Q water was used to make all of the essential aqueous solutions. For electrode modification and all

electrochemical experiments, a potentiostat CHI 701 with a three-electrode setup was employed. The 3 mm diameter GCE, Ag/AgCl (KCl sat.), and Pt wire were used as working electrode, reference, and counter electrodes respectively.

3.3.2 Electrochemical Deposition of Christmas-tree-shaped Palladium Nanostructures

The Pd nanostructures in the shape of a Christmas tree were electrochemically deposited on the GCE. To eliminate contaminants, the GCE surface was mechanically cleaned using alumina powder (0.05 m diameter) and sonicate with water and ethanol for 10 minutes. Then GCE surface was electrochemically cleaned with 0.1 M H_2SO_4 (Ar saturated) solution by potential cycling from 0 V to +1.0 V at a scan rate of 100 mV s^{-1} and washed with water followed by dry under room conditions. The GCE was modified by 15 mM Na_2PdCl_4 solution (dissolved in 0.1 M H_2SO_4) by constant potential mode. Five electrodes have been constructed by constant potential mode and identified: Pd/GCE-0.1V_175S, Pd/GCE-0.1V_400S, Pd/GCE-0.1V_600S, Pd/GCE-0.4V_175S, and Pd/GCE-0.4V_400S for the deposition of -0.1 V for 175 s, 400 s, 600 s, and -0.4 V for 175 s, 400 s, respectively.

3.3.3 Characterizations

A scanning electron microscope (SEM) combined with energy-dispersive x-ray spectroscopy (EDX, TM3030Plus miniscope; Hitachi Ltd.) and field-emission scanning electron microscopy were used to examine the silver dendritic structure (FE-SEM, S4100; Hitachi Ltd.). X-ray photoelectron spectroscopy (XPS) measurements were also

performed using an Al K radiation source (1486.6 eV) and a delay-line detector (DLD) spectrometer (Kratos Axis-Ultra; Kratos Analytical Ltd.). Powder x-ray diffractometer (XRD) patterns were recorded as a 2θ range from 20° to 90° on a completely automated horizontal multi-purpose x-ray diffractometer (Rigaku Smartlab; Rigku Corp.).

3.4 Results and Discussion

3.4.1 Morphological and elemental analysis

Figure 3.1(a-d) shows FE-SEM images of Pd/GCE-0.1V_400S. The development of Christmas-tree-shaped nanostructures is revealed by FE-SEM. Nanostructures are uniformly dispersed onto GCE seen in Figure 3.1a. High-level enlargement pictures (Figure 3.1(b-d)) demonstrated exceptional shape of 200–300 nm Christmas-tree-shaped nanostructures. Each of the Christmas-tree-shaped structures has around 10-12 sharp edges (Figure 3.1d). The Pd nanostructure, as validated through EDX, is exclusive and distinct from earlier published findings like nanoparticles, dendritic, or rod shape structures [7,19]. Pd nanostructures in the shape of Christmas trees were electrodeposited on the GCE surface using 15 mM Na_2PdCl_4 solution at -0.1 V for 400 seconds. The atomic ratio of the Pd/GCE-0.1V_400S is shown in Figure 3.1e. The Pd/GCE-0.1V_400S contains C, O, and Pd elements. When compared to other elements, the quantity of Pd is relatively large. As a result of the constant potential manner of electrodeposition, the Pd is effectively deposited on the GCE. The C element in the EDX study originates from GCE, while the O element might be due to PdO, as verified by XPS analysis. For Pd oxidation state validation, the XPS study had performed for Pd/GCE-0.1V_400S. Two prominent peaks were visible in the Pd 3d XPS spectra

(Figure 3.1f). These two peaks were separated by 5.2 eV with 340.7 eV and 335.5 eV binding energies which reflect both Pd ($3d_{3/2}$) and Pd ($3d_{5/2}$) respectively [47–50]. In the Pd/GCE-0.1V_400S, the XPS measurements indicated both metallic and oxide forms of Pd. When compared to metallic Pd, the quantity of PdO detected at higher binding energies was roughly 15 %. At 343.6 eV and 338.3 eV, two satellite peaks could be seen. The significant quantity of metallic Pd found in Pd/GCE-0.1V_400S is responsible for these two satellite peaks [51]. The XRD pattern for Pd/GCE-0.1V_400S is shown in Figure 3.1g. The C (002) plane of graphite corresponds to the wide diffraction peak at 25.1°. The C (100), C (004), and C (110) planes are found at 43.3°, 54.5°, and 78.8° in XRD, respectively [14,52,53]. The presence of GCE caused these peaks to emerge. The Pd (111) plane is represented by the diffraction peak at 40.2° [54]. The Pd (200) Pd (220) and Pd (311) planes were also identified at 46.7°, 68.1°, and 82.3°, respectively [55].

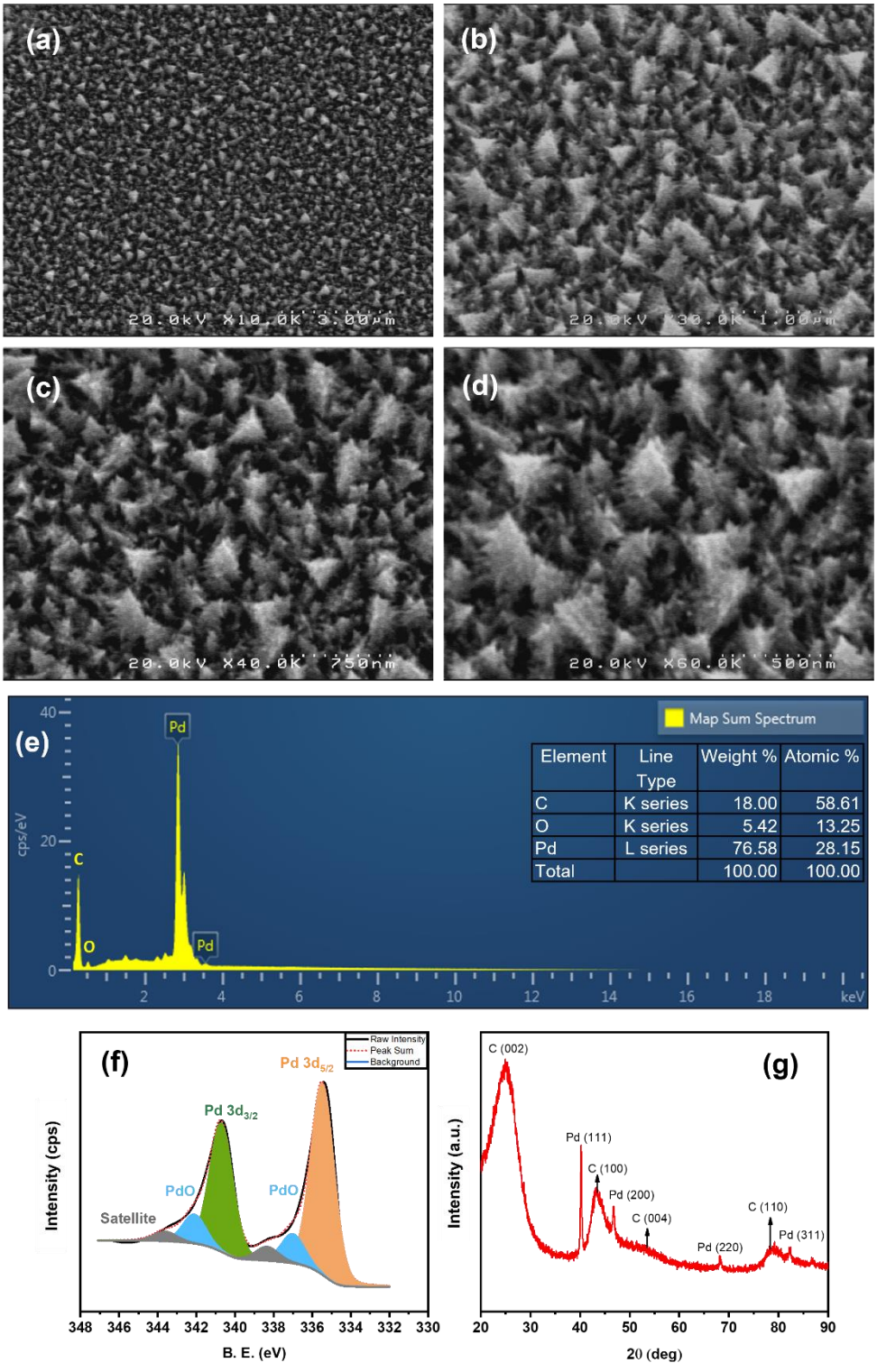

Figure 3.1 Pd/GCE-0.1V_400S characterization. (a-d) low and high magnification FE-SEM images, (e) the EDX analysis atomic element ratio, (f) the XPS spectra of Pd 3d, and (g) XRD pattern.

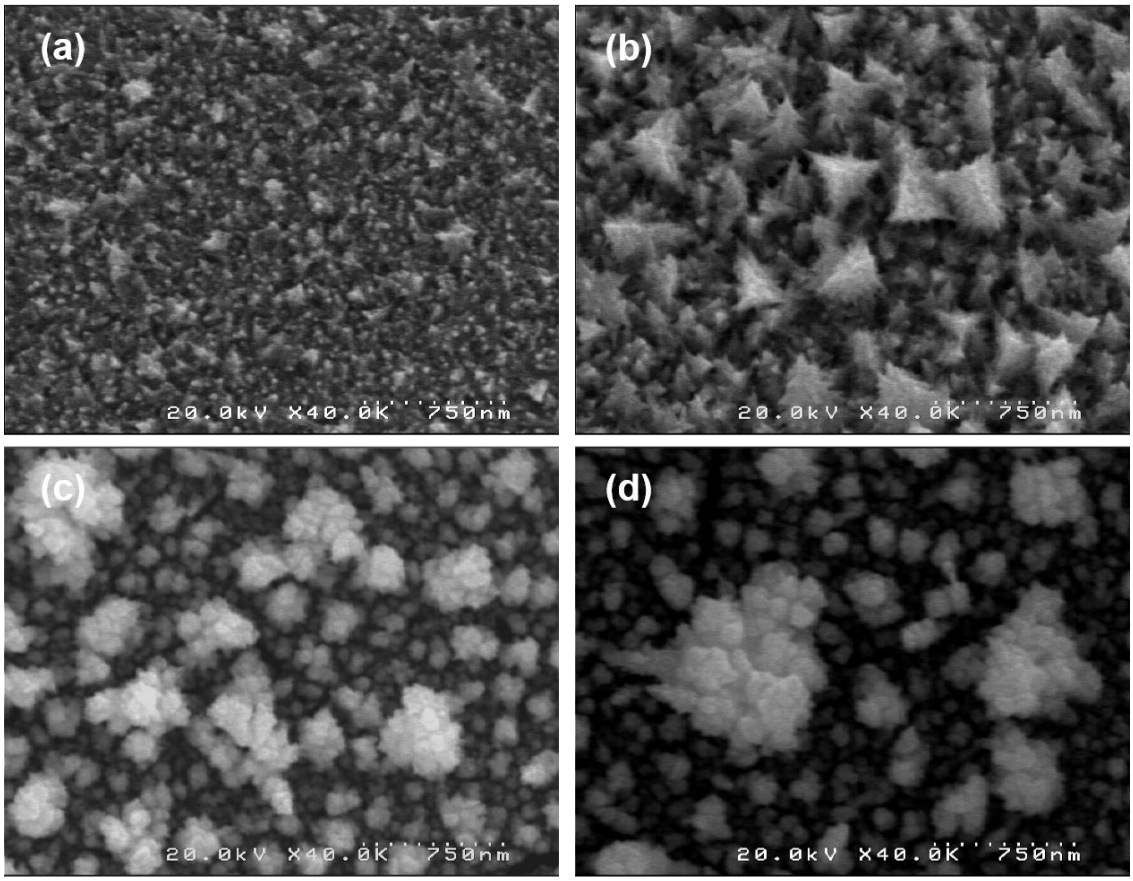

Figure 3.2 FE-SEM image of (a) Pd/GCE-0.1V_175S, (b) Pd/GCE-0.1V_600S, (c) Pd/GCE-0.4V_175S, and (d) Pd/GCE-0.4V_400S

As shown in Figure 3.2, I employed various potential and deposition times for the morphological study of electrodes. Although the potential of -0.1 V has been applied for 175 s (Figure 3.2a), the Pd nanostructures in form of the Christmas tree have not formed. The Pd/GCE-0.1V 600S exhibits (Figure 3.2b) comparable nanostructures but not identical to those of Christmas trees shapes. The nanostructures had fewer sharp edges than those deposited for 400 seconds at -0.1 V on the GCE (Figure 3.1d). With increasing deposition time, the amount of metal deposited increased. As a result of this growth, nanostructures with less sharp edges are formed. The optimum electrodeposition time of 400 s ensures that Christmas-tree-nanostructures having numerous sharp edges

onto GCE have an appropriate formation at -0.1 V. Deposition time is hence a crucial component for the creation of a unique nanostructure. I used a separate potential -0.4 V for 175 and 400 s to assess the effect of the applied potentials on the nanostructure morphology. Pd was deposited randomly on the GCE surface, according to FE-SEM images (Figure 3.2(c-d)), and no Christmas-tree-shaped nanostructures were seen. The shape of the Pd formations was influenced by the precursor (Na_2PdCl_4) concentration (Figure 3.3). When deposition potential -0.1V was used for 400 s, a lower concentration of Na_2PdCl_4 (5 mM) led to deposits of Pd with less defined structures. The random Pd structures resulted in a higher Na_2PdCl_4 concentration (30 mM). Thus the concentration of 15 mM Na_2PdCl_4 is needed to construct the Pd nanostructures in the Christmas-tree-form with many sharp edges. In the formation of vertically growing Pd nanostructures, the supporting electrolyte is equally important. Specific sulfuric acid anion (SO_4^{2-}) adsorption on Pd surfaces, is well recognized for vertical development of Pd during electrodeposition [19]. The development of the Christmas-tree-shaped Pd nanostructures onto GCE is aided through diffusion-limited current by -0.1 V [7], 400 s deposition time with Pd precursor concentration (15 mM Na_2PdCl_4) and SO_4^{2-} (supporting electrolyte anion).

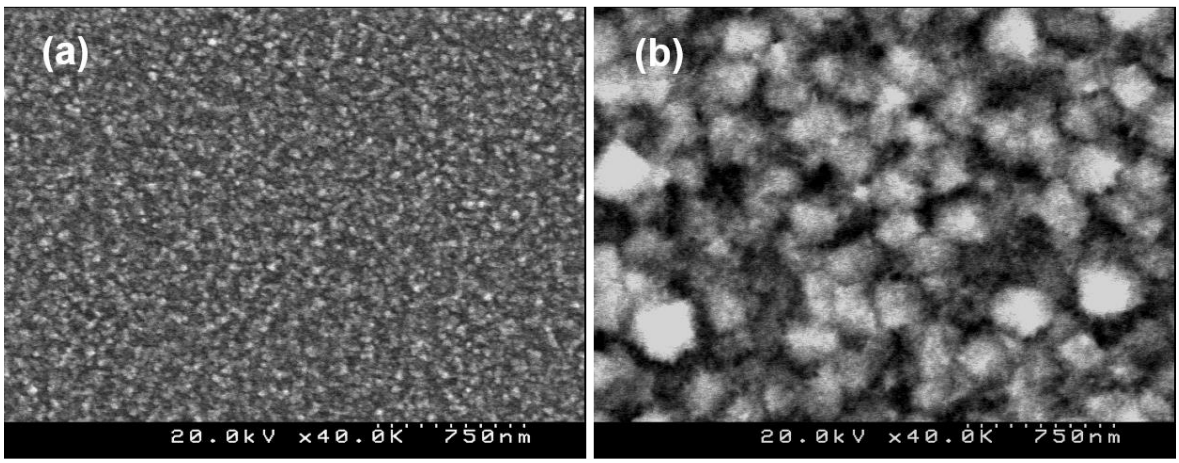

Figure 3.3 FE-SEM pictures: Pd has been electrodeposited at 0.1 V for 400 seconds from a solution comprising various Na_2PdCl_4 concentrations in 0.1 M H_2SO_4. (a) 5 mM Na_2PdCl_4 solution; (b) 30 mM Na_2PdCl_4 solution

The Pd 3d XPS spectra for the other modified electrodes revealed comparable characteristics (Figure 3.4) to those observed for Pd/GCE-0.1V_400S. Both metallic and oxide forms of Pd are found from the fitting curve of XPS spectra. As a result, the oxidation status of the Pd deposit is unaffected by varied deposition circumstances.

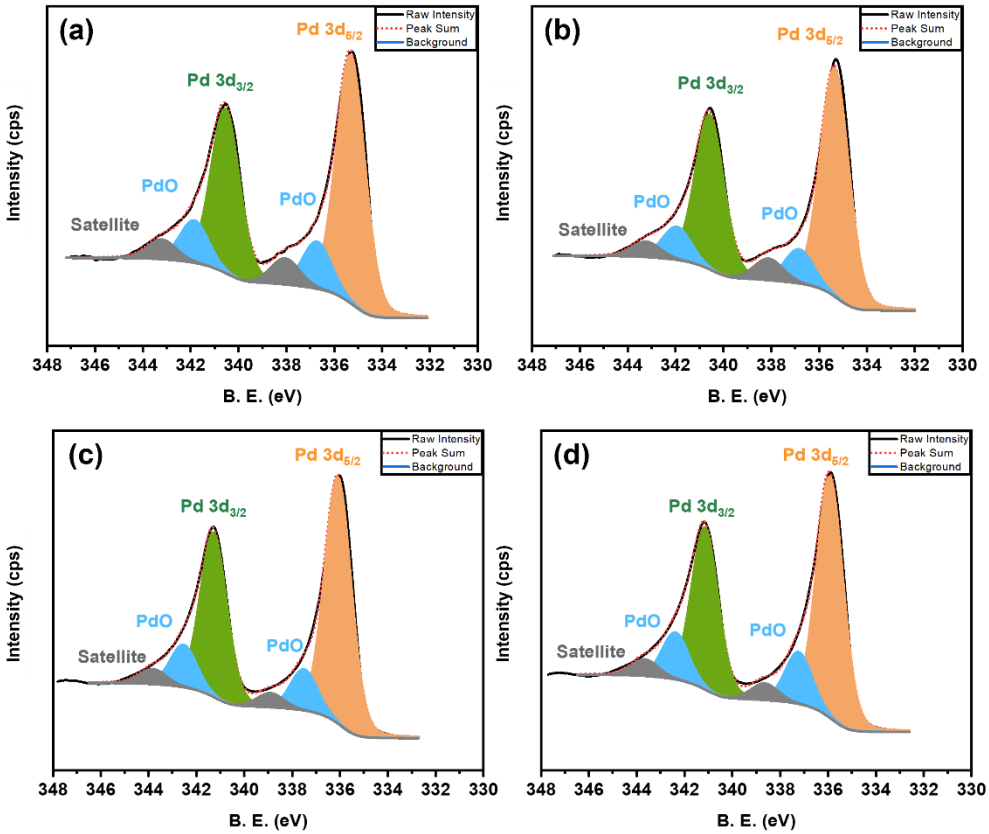

Figure 3.4 XPS spectra of Pd 3d. (a) Pd/GCE-0.1V_175S, (b) Pd/GCE-0.1V_600S, (c) Pd/GCE-0.4V_175S, and (d) Pd/GCE-0.4V_400S.

Figure 3.5 depicts the XRD patterns of the remaining modified electrodes. Among those electrodes, the Pd (111) plane has discovered with a 2θ value that is identical to the Pd/GCE-0.1V_400S.

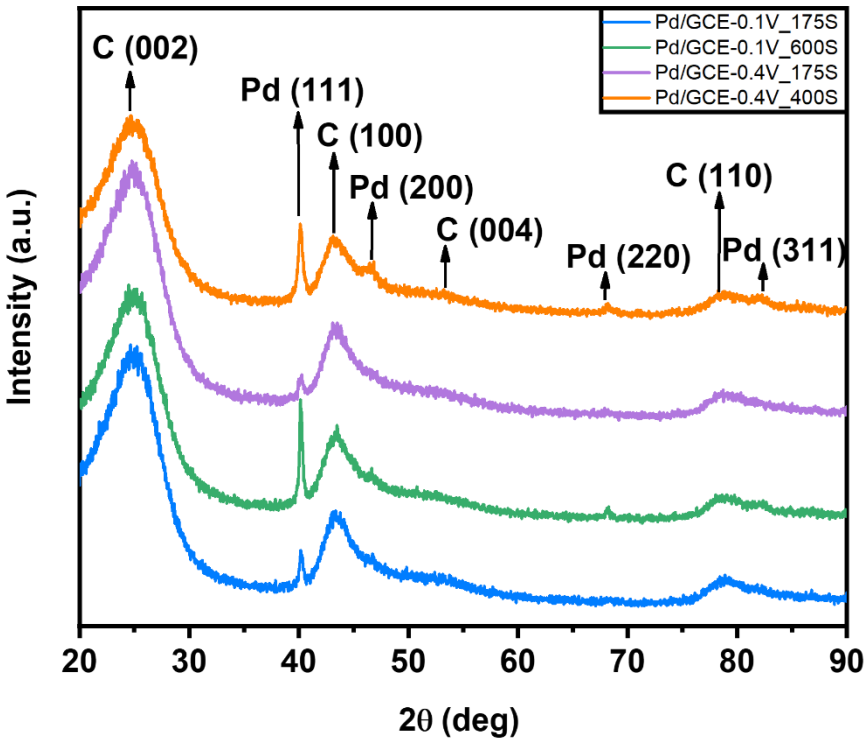

Figure 3.5 XRD patterns of other modified electrodes.

3.4.2 Electrocatalytic Performance

Under various experimental conditions, the electrocatalytic activity of Pd/GCE-0.1V_400S for AA electrooxidation in 1 M KOH was studied. In the absence and presence of AA (5.6 mM) in a 1 M KOH solution, cyclic voltammograms were obtained among -0.8 V and +0.7 V at 50 mV s^{-1} scan rate (Figure 3.6a). An oxidation wave of AA at -0.1 V could be seen at the Pd/GCE-0.1V_400S (red line). There is no oxidation peak when no AA is present in the 1 M KOH solution (cyan line). The reduction of PdO to Pd

results in a significant reduction peak at -0.4 V [56]. In 1 M KOH, a minor oxidation peak was observed at -0.2 V for the Pd/GCE-0.1V_400S (Figure 3.6a, cyan line). The formation of Pd^{2+} from Pd^{0} in alkaline conditions causes this oxidation peak [57,58]. In an alkaline environment, Pd is first oxidized to create Pd^{2+}, which improves AA oxidation. Cyclic voltammetry measurements were carried out to clarify the catalytic effect of the AA electrooxidation at the GCE and the Christmas trees-shaped Pd nanostructures. When compared to the Pd/GCE-0.1V_400S (red line), the voltammogram of the bare GCE (black line) reveals a lower AA oxidation peak. For AA electrooxidation, the Pd/GCE-0.1V_400S offers a significantly greater current density (4.5 mA cm^{-2}) than bare GCE (0.6 mA cm^{-2}) in the 1 M KOH. In alkaline conditions, the Pd plays a critical role in the outstanding catalytic activity of AA electrooxidation.

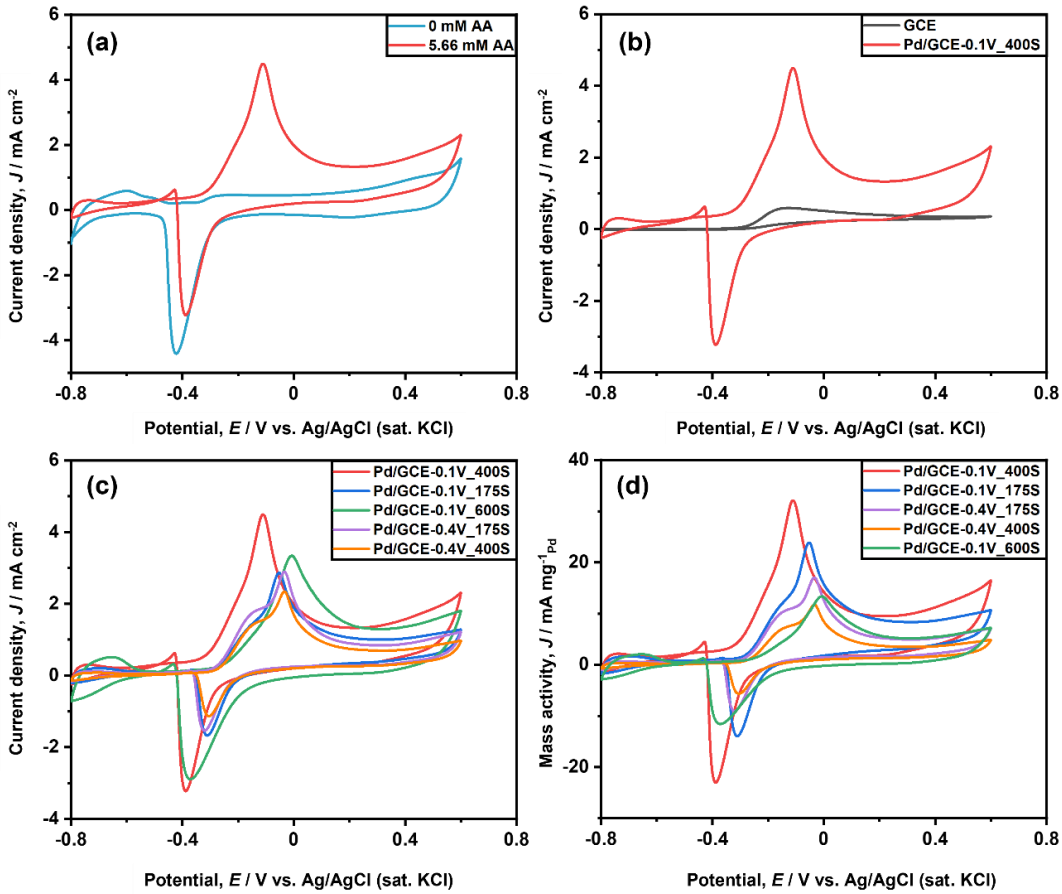

Figure 3.6 (a) Electrocatalytic performance evaluation of Pd/GCE-0.1V_400S in the absence and presence of 5.6 mM ascorbic acid, (b) comparison between bare GCE and Pd/GCE-0.1V_400S in 5.6 mM ascorbic acid. (c) Electrocatalytic response of ascorbic acid electrooxidation at different modified electrodes. (d) Mass activities of different modified electrodes. All the cyclic voltammograms were obtained in 1 M KOH at 50 mV s^{-1} scan rate.

All the electrodes were compared for the impact of distinct Pd nanostructures on AA electrooxidation. In the presence of 5.6 mM AA in 1 M KOH with the 50 mV s^{-1} scan rate, Figure 3.6c shows the response of all modified electrodes. The Christmas-tree-shaped Pd nanostructures electrode had the maximum catalytic activity of AA electrooxidation in 1 M KOH solution between all electrodes. Increased electrode surface area can improve catalytic activity. The electrochemical surface area (ESA) of all electrodes was estimated using the Randles–Sevcik equation by applying CV at varied scan rates in 3.0 mM $K_3Fe(CN)_6$ solution [59]

$$I_p = (2.69 \times 10^5) n^{3/2} A C D^{1/2} v^{1/2} \qquad (3.2)$$

Here I_p is peak current (A), A denotes the electrode area (cm^2), n means the total amount of transferred electrons during the redox $K_3Fe(CN)_6$ process, D stands for the diffusion coefficient of the $K_3Fe(CN)_6$ ($cm^2\ s^{-1}$), C is the $K_3Fe(CN)_6$ solution concentration (mol cm^{-3}), and v denotes the scan rate (V s^{-1}). The Pd/GCE-0.1V_400S had an ESA of 0.07 cm^{-2}, greater compared to Pd/GCE-0.1V_175S (0.05 cm^{-2}) and Pd/GCE-0.4V_175S (0.4

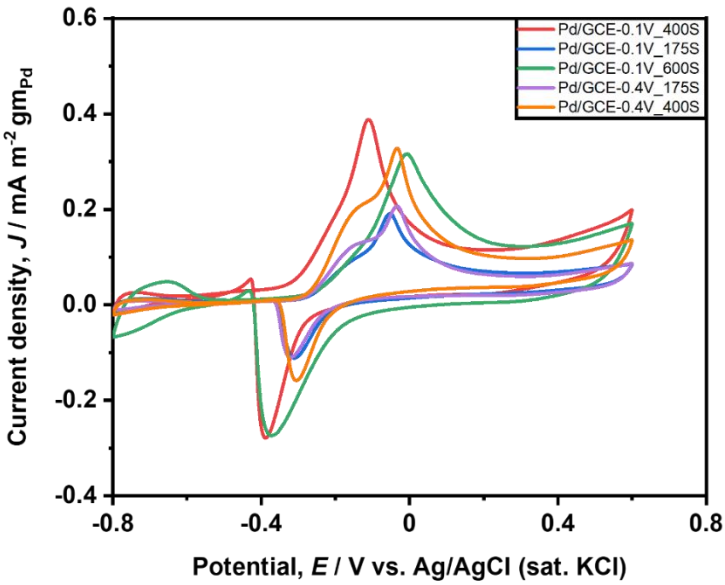

Figure 3.7 ECSA normalized 5.6 mM ascorbic acid electrooxidation at different modified electrodes. All of the cyclic voltammograms were obtained in 1 M KOH at a 50 mV s^{-1} scan rate.

cm^{-2}). Although Pd/GCE-0.4V_400S has a comparable ESA (0.07 cm^{-2}) to Pd/GCE-0.1V_400S the structural variations between them may have a significant impact on

catalytic activity. The Christmas-tree-shaped nanostructures shown in Figure 3.1d contain numerous sharp edges which improve AA electrooxidation. Even though Pd/GCE-0.1V_600S has a higher ESA (0.09 cm^{-2}), the electrocatalytic performance is lower than Pd/GCE-0.1V_400S. The Pd/GCE-0.1V_600S had less sharp edges of Christmas-tree-shaped nanostructures found in the FE-SEM image (Figure 3.2b) than the Pd/GCE-0.1V_400S (Figure 3.1d). The Pd/GCE-0.1V_400S is superior in catalytic performance due to the presence of many sharp edges in Christmas-tree-shaped nanostructures as compared to other modified elements. The bare GCE has an ESA of 0.06 cm^2, which is even smaller than Pd/GCE-0.1V_400S. The Pd/GCE-0.1V_400S has

a higher current density than GCE, as seen in Figure 3.6b. At Pd/GCE-0.1 V 400S, the onset potential of AA electrooxidation is lower than all the modified electrodes (Figure 3.6c). Except for the Pd/GCE-0.1V_400S, the onset potential of Pd/GCE-0.1V_600S is nearly identical compared to all modified electrodes (Table 3.1). The morphological effect can explain this pattern. Though the shape of Pd/GCE-0.1V _600S is similar to that of Pd/GCE-0.1V 400S, less sharp edges make it less catalytically reactive for AA electrooxidation. The mass activity of the modified electrodes was used to study the morphological impact of Pd nanostructures on AA electrooxidation in 1 M KOH solution. By normalizing the Pd mass loading at each electrode, the mass activity of each electrode was determined. The Pd mass (in mg) is determined by subtract the GCE mass before and after the electrodeposition:Pd/GCE-0.1V_175S (0.12 mg), Pd/GCE-0.1V_400S (0.14 mg), Pd/GCE-0.4V_175S (0.17 mg), Pd/GCE-0.4V_400S (0.20 mg), and Pd/GCE-0.1V_600S (0.25mg). The mass activity of all the modified electrodes is shown in Figure 3.6d. The mass activity value and onset potential for all electrodes are summarized in Table 3.1. The Pd/GCE-0.1V_400S has an estimated mass activity of 32.1 mA mg_{Pd}^{-1},

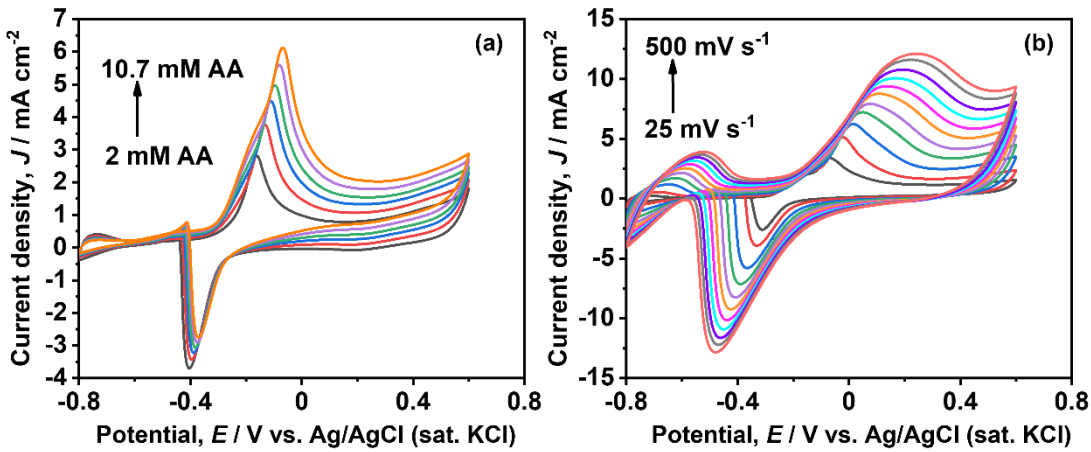

Figure 3.8 (a) Ascorbic acid concentration effect at scan rate 50 mV s^{-1} and (b) scan rate effect of 7.4 mM ascorbic acid in 1M KOH solution at Pd/GCE-0.1V_400S.

which is 1.34, 1.91, 2.41, and 2.76 times more than Pd/GCE-0.1V_175S, Pd/GCE-0.4V_175S, Pd/GCE-0.1V_600S, and Pd/GCE-0.4V_400S. This finding also proved the superior catalytic activity of Christmas-tree-shaped Pd nanostructures in 1 M KOH solution for AA electrooxidation.

Table 3.1 Mass activity and onset potential for all electrodes

Name of the electrode	Mass activity (mA mg_{Pd}^{-1})	Onset potential (V)
Pd/GCE-0.1V_175S	23.9	-0.29
Pd/GCE-0.1V_400S	32.1	-0.35
Pd/GCE-0.1V_600S	13.3	-0.27
Pd/GCE-0.4V_175S	16.8	-0.28
Pd/GCE-0.4V_400S	11.6	-0.27

The electrochemically active regions of modified electrodes have been studied further. A key parameter describing the number of electrochemically active sites relating to the mass of the metal catalyst is the electrochemical active surface (ECSA) [57].

$$ECSA = Q/sl \quad (3.3)$$

Here *Q* represents coulombic charge for reduction peak of metal oxide, *s* is the proportionality constant =0.405 mC cm^{-2}, and *l* denotes metal loading in g m^{-2}. Table 3.2 summarizes the ECSA for all electrodes. Table 3.2 shows that a maximum ECSA value is found for Pd/GCE-0.1V_400S compared to other catalysts. Therefore Pd/GCE-0.1V_400S has the most electrocatalysis center. Pd/GCE-0.1V_600S has a lower ECSA value due to fewer active catalyst sites. This further shows that the Pd nanostructures of Christmas-tree with numerous sharp edges are superior to AA electrooxidation, making the Pd/GCE-0.1V_400S electrode better.

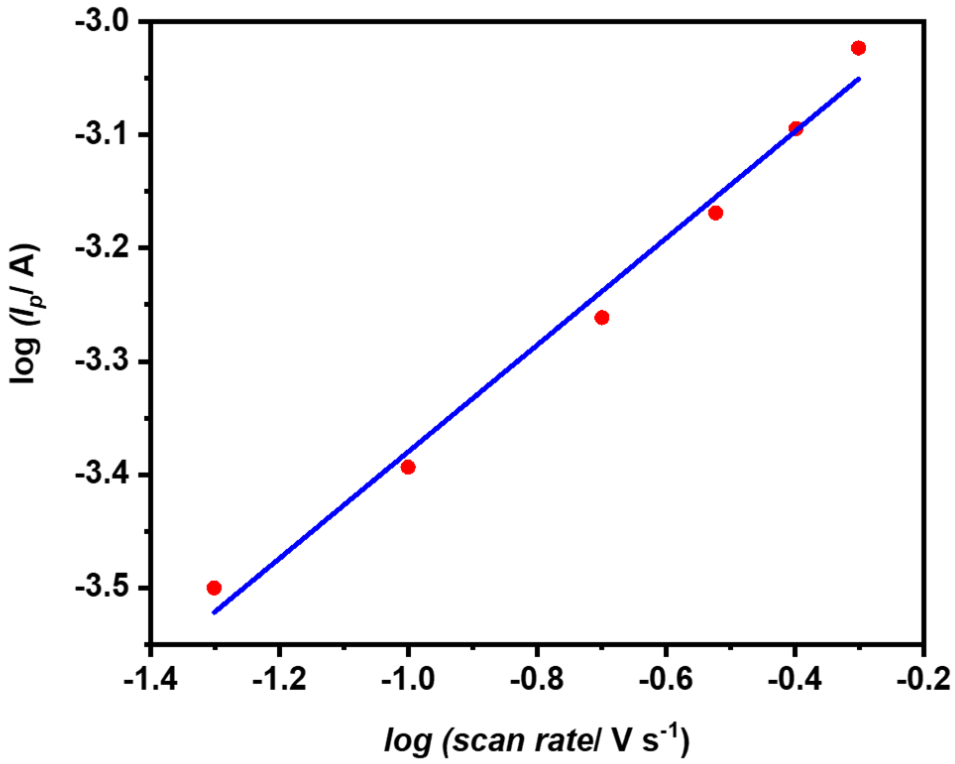

Figure 3.9 The plot of Log (I_p) vs log (scan rate) at Pd/GCE-0.1V_400S. Experimental data are taken from Figure 3.8b.

Table 3.2 Calculated ECSA value for all electrodes

Name of the electrode	Metal loading (g m^{-2})	ECSA (m^2 gm^{-1})
Pd/GCE-0.1V_175S	24.0	0.75
Pd/GCE-0.1V_400S	20.0	0.81
Pd/GCE-0.1V_600S	18.9	0.74
Pd/GCE-0.4V_175S	40.0	0.20
Pd/GCE-0.4V_400S	35.7	0.13

The ECSA normalized cyclic voltammograms are shown in Figure 3.7. After the ECSA normalization, the Pd/GCE-0.1V_400S electrode still showed high performance. The hierarchical Pd Christmas-tree-shaped structures provide high performance.

Figure 3.8a shows the effect of AA concentration (2.0–10.7 mM) on the surface Pd/GCE-0.1V_400S at a scan rate of 50 mV s^{-1}. With the increasing AA content, the current density of oxidation increased. With increased concentration, the maximum potential AA oxidation changed positively and can be referred to as diffusion-controlled [12] reactions. This change is due to the disruption of the analyte mass transportation mechanism. The rise in AA concentrations disrupts the process of diffusion, and the electrochemical system is more likely to restore mass transportation. The peak potential therefore changed favorably. Figure 3.8b shows the scan rate effect in presence of 7.4 mM AA electrooxidation in the 1 M KOH solution. With the increased scanning rate, the oxidation peak of the AA molecules increases. The peak current increased with the scan

rate due to heterogeneous kinetics. In Figure 3.9, with a slope value of 0.47, the plots of log peak current (Ip) are linear with the log (scan rate). This finding indicates that the AA electrooxidation follows a process of diffusion control with a slope value close to the theoretical slope value of 0.5 [14]. This result also verifies a diffusion-controlling response. The peaks at -0.8 V to -0.7 V are rising (Figure 3.8b) during scan rate increasing. The peak rise is for adsorption and desorption of hydrogen in the Pd catalyst [56,57].

Figure 3.10 depicts a chronoamperometric stability assessment of all modified electrodes for AA electrooxidation in 1 M KOH. For 1000 seconds, the peak potential of the AA electrooxidation was applied. All curves that began with the dropping current density, as shown in Figure 3.10, were attributable to the initial electrooxidation of AA at the beginning. Then, the curves turn flat and steady. The current density for all electrodes

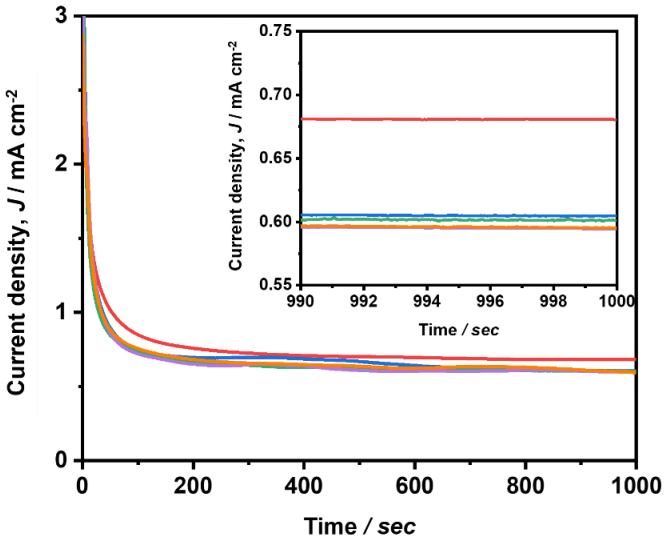

Figure 3.10 Chronoamperogramms in presence of 10.7 mM ascorbic acid in 1 M KOH solution at different modified electrodes (inset: magnification of chronoamperometric data from 990 to 1000 s for all electrodes).

from 990 to 1000 s is shown in the inset enlarged figure in Figure 3.10. When compared to all other modified electrodes, the Pd/GCE-0.1V_400S (red line) still demonstrated better electrocatalytic activity after 1000 s.

After the chronoamperometry (AA oxidation), I have checked the morphology of the Pd/GCE-0.1V_400S (Pd Christmas-tree-shape structures). Figure 3.11 showed the FE-SEM image where the structures of the Christmas-tree-shape remained almost similar as before the AA oxidation (Figure 3.1c). This proved that the Pd Christmas-tree-shaped structures have good stability.

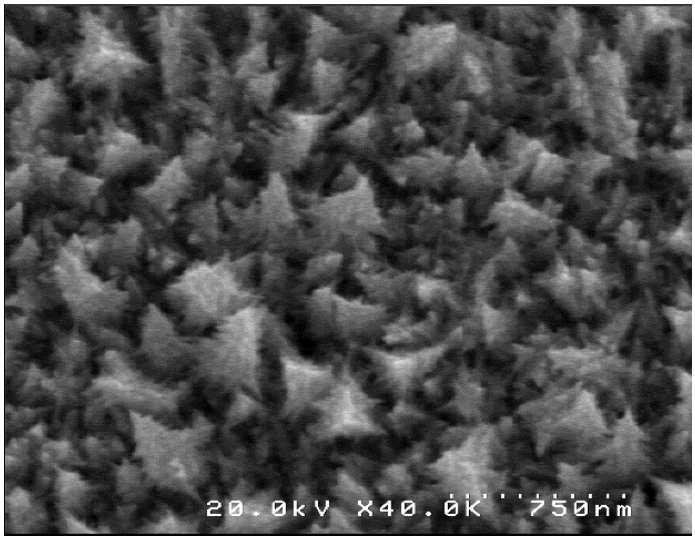

Figure 3.11 FE-SEM image of Pd/GCE-0.1V_400S after the chronoamperometry.

3.4.3 Selectivity and Real Samples Analysis

The Amperometry technique is used to determine the lower detection limit (LOD) as well as linear range value for AA electrooxidation in 1 M KOH solution at Pd/GCE-0.1V_400S (Figure 3.12). The current response has risen linearly as the AA concentration increased. The linear range value (1-950 µM) and LOD (1 µM) of AA

electrooxidation at Pd/GCE-0.1V_400S are equivalent to previously reported catalysts (Table 3.3). A comparison study between recently published AA electrooxidation catalysts and our catalyst is summarized in Table 3.3. In all cases, the peak current density is calculated using the peak current of cyclic voltammetry data. The Pd/GCE-0.1V_400S has the maximum peak current density. This verifies the outstanding catalytic activity of the Pd/GCE-0.1V_400S catalyst for AA electrooxidation.

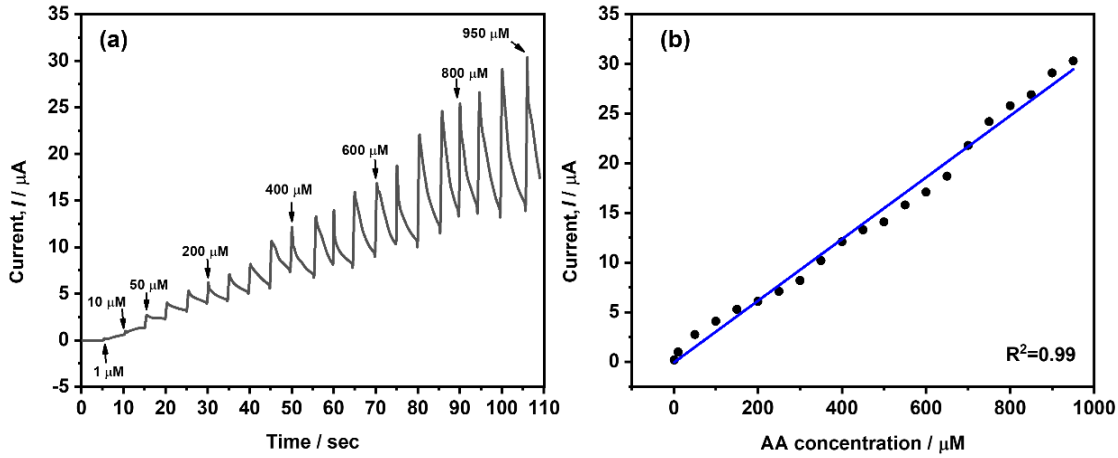

Figure 3.12 (a) Amperometric signals of Pd/GCE-0.1V_400S in 1 M KOH in the presence of ascorbic acid at various concentrations, and (b) related linear association between peak current and ascorbic acid concentration.

Table 3.3 Comparison study of ascorbic acid electrooxidation.

Electrode	Peak current density ($\mu A\ cm^{-2}$)	Onset potential (V)	Solution pH	LOD (µM)	Linear range (µM)	Ref.
Pd/GCE-0.1V_400S	4500	-0.35	Alkaline	1.0	1-950	This work
Pd/N-3D mesoporous C/GCE	2475	-0.20	Alkaline	-	400-4000	[42]
Pd NPs/carbon/GCE	750	-0.10	Alkaline	-	-	[43]
rMWCNTs/ Pd nanotubes /graphite	42	-0.04	Neutral	0.17	500-7500	[44]
Ag Nps/PVP/GCE	1650	+0.25	Neutral	0.47	2-150	[60]
Carbon nanoonions /$NiMoO_4$/ $MnWO_4$/GCE	-	-0.05	Acidic	0.33	1-100	[61]
PAP/ZrO_2 Nps / carbon nanotubes /GCE	35	+0.12	Acidic	0.35	1-295	[62]

Here, NPs= nanoparticles, rMWCNTs=reduced multi-walled carbon nanotubes; PVP= Polyvinylpyrrolidone; ; PAP= Poly(aminopyrazine).

Amperometry experiments in 1 M KOH solution were conducted for the selectivity evaluation of Pd/GCE-0.1V_400S for AA electrooxidation (Figure 3.13). Various interfering chemicals, including KNO_3, $ZnSO_4$, $FeCl_2$, and $MgCl_2$, were introduced. Each interfering chemical has a negligible response compared to the AA (Figure 3.13). This result validated that the Pd/GCE-0.1V_400S electrode has excellent selectivity for AA electrooxidation. The analytical performance of the Pd/GCE-0.1V_400S was further examined using an actual sample analysis in a 1 M KOH solution. I utilized a vitamin C tablet as well as a vitamin C drink. The recovery range of the spiked samples was 98.2 % to 101.5 % (Table 3.4), showing the excellent efficiency of the Pd/GCE-0.1V_400S for AA electrooxidation.

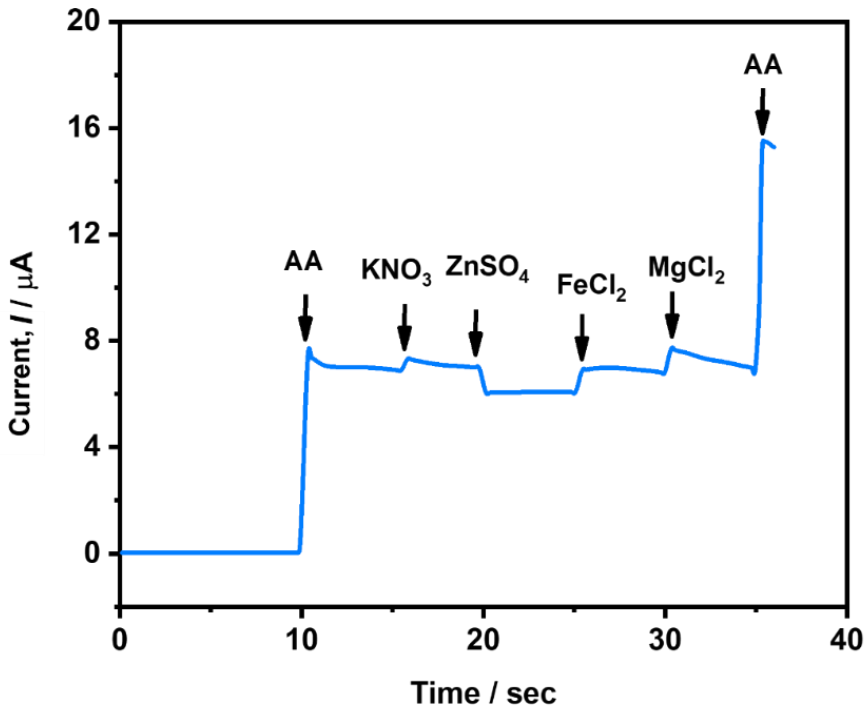

Figure 3.13 Different substances interference effects on ascorbic acid electrooxidation at Pd/GCE-0.1V_400S in 1 M KOH solution. Ascorbic acid has a concentration ratio of 1:1 with the interfering chemical

Table 3.4 Amperometric study of real samples at Pd/GCE-0.1V_400S (n=3).

Sample	Added (µM)	Obtained (µM)	RSD (%)	Recovery (%)
Vitamin C tablet	150	152.3	3.2	101.5
Vitamin C juice	150	147.3	2.1	98.2

The Pd catalyst showed good catalytic activity for AA electrooxidation in alkaline condition. The comparison between Ag catalyst (Chapter 2) and Pd catalyst (Chapter 3) is shown in Figure 3.14. The Pd catalyst showed higher catalytic activity than the Ag catalyst and the unmodified electrode (GCE). For this observation, it can be concluded that the Pd catalyst is suitable as anode catalyst for the alkaline ascorbic acid fuel cell system. In the next chapter Pd based catalysts (in powder form) will be synthesized and applied for the alkaline ascorbic acid fuel cell system.

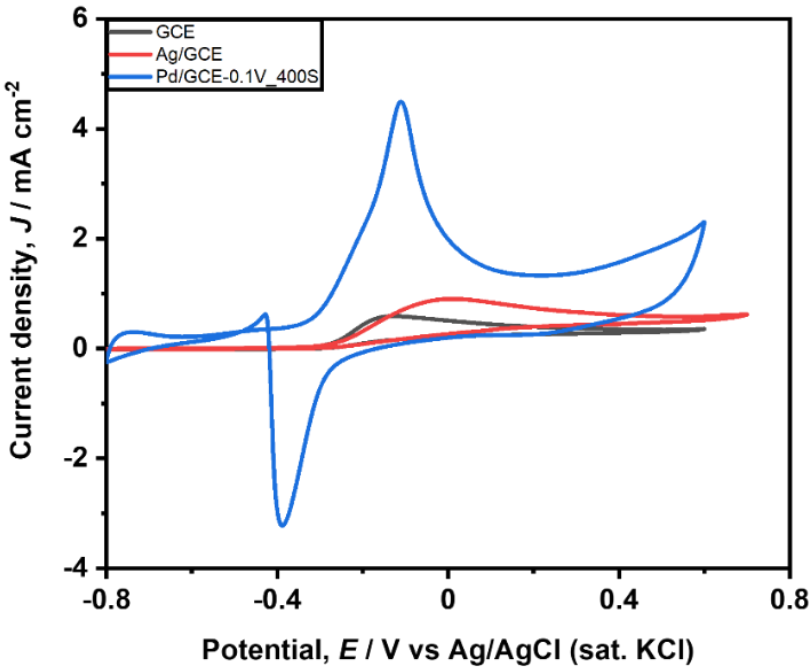

Figure 3.14 Catalytic activity comparison of 5.6 mM ascorbic acid between bare GCE, Ag dendrite (Ag/GCE), Pd/GCE-0.1 V_400S in at 50 mV S^{-1} scan rate in 1 M KOH solution.

3.5 Conclusion

Onto GCE, a one-pot constant potential mode electrodeposition technique was used to create unique Christmas-tree-shaped Pd nanostructures without any additives or premodification of the electrode surfaces. During electrodeposition, the nanostructure morphology was substantially influenced by the applied potential, duration, precursor concentration, and supporting electrolyte. Several customized Pd/GCE electrodes were created using various deposition conditions, and Christmas-tree-shaped Pd nanostructures having numerous sharp edges demonstrated the highest AA electrooxidation performance in 1 M KOH solution. The Pd/GCE-0.1V_400S also showed high in 1 M KOH during AA electrooxidation. The straightforward electrodeposition approach for the construction of unique Pd nanostructures onto GCE could open new avenues for the development of Pd-based catalysts in electrocatalysis.

References

[1] H. Jeong, J. Kim, Electrodeposition of Nanoflake Pd Structures: Structure-Dependent Wettability and SERS Activity, ACS Appl. Mater. Interfaces. 7 (2015) 7129–7135. https://doi.org/10.1021/acsami.5b02113.

[2] E. Katz, I. Willner, J. Wang, Electroanalytical and Bioelectroanalytical Systems Based on Metal and Semiconductor Nanoparticles, Electroanalysis. 16 (2004) 19–44. https://doi.org/10.1002/elan.200302930.

[3] M.J. Banholzer, J.E. Millstone, L. Qin, C.A. Mirkin, Rationally designed nanostructures for surface-enhanced Raman spectroscopy, Chem. Soc. Rev. 37 (2008) 885. https://doi.org/10.1039/b710915f.

[4] M.T. Islam, M.M. Hasan, M.F. Shabik, F. Islam, Y. Nagao, M.A. Hasnat, Electroless deposition of gold nanoparticles on a glassy carbon surface to attain methylene blue degradation via oxygen reduction reactions, Electrochim. Acta. 360 (2020) 136966. https://doi.org/10.1016/j.electacta.2020.136966.

[5] Y. Zhao, J. Qin, H. Xu, S. Gao, T. Jiang, S. Zhang, J. Jin, Gold nanorods decorated with graphene oxide and multi-walled carbon nanotubes for trace level voltammetric determination of ascorbic acid, Microchim. Acta. 186 (2019) 17. https://doi.org/10.1007/s00604-018-3138-2.

[6] H. Kim, H. Park, D.K. Kim, S. Oh, I. Choi, S.K. Kim, Electrochemically Fabricated NiW on a Cu Nanowire as a Highly Porous Non-Precious-Metal Cathode Catalyst for a Proton Exchange Membrane Water Electrolyzer, ACS Sustain. Chem. Eng. 7 (2019) 8265–8273. https://doi.org/10.1021/acssuschemeng.8b06643.

[7] S. Choi, H. Jeong, K. Choi, J.Y. Song, J. Kim, Electrodeposition of Triangular Pd Rod Nanostructures and Their Electrocatalytic and SERS Activities, ACS Appl. Mater. Interfaces. 6 (2014) 3002–3007. https://doi.org/10.1021/am405601g.

[8] R. Ji, L. Wang, L. Yu, B. Geng, G. Wang, X. Zhang, Effective Electrocatalysis Based on Ag2O Nanowire Arrays Supported on a Copper Substrate, ACS Appl. Mater. Interfaces. 5 (2013) 10465–10472. https://doi.org/10.1021/am4016523.

[9] L. Wang, L. Xu, H. Kuang, C. Xu, N.A. Kotov, Dynamic Nanoparticle Assemblies, Acc. Chem. Res. 45 (2012) 1916–1926. https://doi.org/10.1021/ar200305f.

[10] R. Shenhar, T.B. Norsten, V.M. Rotello, Polymer-Mediated Nanoparticle Assembly: Structural Control and Applications, Adv. Mater. 17 (2005) 657–669. https://doi.org/10.1002/adma.200401291.

[11] L.P. Bicelli, B. Bozzini, C. Mele, L. D'Urzo, A review of nanostructural aspects of metal electrodeposition, Int. J. Electrochem. Sci. 3 (2008) 356–408.

[12] M.A. Hasnat, M.M. Hasan, N. Tanjila, M.M. Alam, M.M. Rahman, pH dependent kinetic insights of electrocatalytic arsenite oxidation reactions at Pt surface, Electrochim. Acta. 225 (2017) 105–113. https://doi.org/10.1016/j.electacta.2016.12.055.

[13] Z.L. Zhou, T.F. Kang, Y. Zhang, S.Y. Cheng, Electrochemical sensor for formaldehyde based on Pt–Pd nanoparticles and a Nafion-modified glassy carbon electrode, Microchim. Acta. 164 (2009) 133–138. https://doi.org/10.1007/s00604-008-0046-x.

[14] M.M. Hasan, R.H. Rakib, M.A. Hasnat, Y. Nagao, Electroless Deposition of Silver Dendrite Nanostructure onto Glassy Carbon Electrode and Its

Electrocatalytic Activity for Ascorbic Acid Oxidation, ACS Appl. Energy Mater. 3 (2020) 2907–2915. https://doi.org/10.1021/acsaem.9b02513.

[15] M.M. Hossain, M.M. Islam, S. Ferdousi, T. Okajima, T. Ohsaka, Anodic Stripping Voltammetric Detection of Arsenic(III) at Gold Nanoparticle-Modified Glassy Carbon Electrodes Prepared by Electrodeposition in the Presence of Various Additives, Electroanalysis. 20 (2008) 2435–2441. https://doi.org/10.1002/elan.200804339.

[16] M.S. Alam, M.F. Shabik, M.M. Rahman, M. del Valle, M.A. Hasnat, Enhanced electrocatalytic effects of Pd particles immobilized on GC surface on the nitrite oxidation reactions, J. Electroanal. Chem. 839 (2019) 1–8. https://doi.org/10.1016/j.jelechem.2019.02.058.

[17] Y. Li, G. Lu, X. Wu, G. Shi, Electrochemical Fabrication of Two-Dimensional Palladium Nanostructures as Substrates for Surface Enhanced Raman Scattering, J. Phys. Chem. B. 110 (2006) 24585–24592. https://doi.org/10.1021/jp0638787.

[18] A.J. Wang, F.F. Li, Z. Bai, J.J. Feng, Large-scale electrosynthesis of Pd nanodendrites and their improved electrocatalytic properties for methanol oxidation, Electrochim. Acta. 85 (2012) 685–692. https://doi.org/10.1016/j.electacta.2012.08.097.

[19] Y.J. Song, J.Y. Kim, K.W. Park, Synthesis of Pd Dendritic Nanowires by Electrochemical Deposition, Cryst. Growth Des. 9 (2009) 505–507. https://doi.org/10.1021/cg8007574.

[20] Y. Fang, S. Guo, C. Zhu, S. Dong, E. Wang, Twenty Second Synthesis of Pd Nanourchins with High Electrochemical Activity through an Electrochemical Route, Langmuir. 26 (2010) 17816–17820. https://doi.org/10.1021/la1036597.

[21] H. Meng, F. Xie, J. Chen, P.K. Shen, Electrodeposited palladium nanostructure as novel anode for direct formic acid fuel cell, J. Mater. Chem. 21 (2011) 11352. https://doi.org/10.1039/c1jm10361j.

[22] H. Meng, S. Sun, J.P. Masse, J.P. Dodelet, Electrosynthesis of Pd Single-Crystal Nanothorns and Their Application in the Oxidation of Formic Acid, Chem. Mater. 20 (2008) 6998–7002. https://doi.org/10.1021/cm8014513.

[23] E. Mourad, L. Coustan, P. Lannelongue, D. Zigah, A. Mehdi, A. Vioux, S.A. Freunberger, F. Favier, O. Fontaine, Biredox ionic liquids with solid-like redox density in the liquid state for high-energy supercapacitors, Nat. Mater. 16 (2017) 446–453. https://doi.org/10.1038/nmat4808.

[24] N. Mahne, B. Schafzahl, C. Leypold, M. Leypold, S. Grumm, A. Leitgeb, G.A. Strohmeier, M. Wilkening, O. Fontaine, D. Kramer, C. Slugovc, S.M. Borisov, S.A. Freunberger, Singlet oxygen generation as a major cause for parasitic reactions during cycling of aprotic lithium-oxygen batteries, Nat. Energy. 2 (2017) 1–9. https://doi.org/10.1038/nenergy.2017.36.

[25] Y. Nabil, S. Cavaliere, I.A. Harkness, J.D.B. Sharman, D.J. Jones, J. Rozière, Novel niobium carbide/carbon porous nanotube electrocatalyst supports for proton exchange membrane fuel cell cathodes, J. Power Sources. 363 (2017) 20–26. https://doi.org/10.1016/j.jpowsour.2017.07.058.

[26] S. Nanda, R. Rana, Y. Zheng, J.A. Kozinski, A.K. Dalai, Insights on pathways for hydrogen generation from ethanol, Sustain. Energy Fuels. 1 (2017) 1232–1245. https://doi.org/10.1039/C7SE00212B.

[27] M. del Cueto, P. Ocón, J.M.L. Poyato, Comparative Study of Oxygen Reduction Reaction Mechanism on Nitrogen-, Phosphorus-, and Boron-Doped Graphene

Surfaces for Fuel Cell Applications, J. Phys. Chem. C. 119 (2015) 2004–2009. https://doi.org/10.1021/jp512588r.

[28] S. Goodwin, D.A. Walsh, Closed Bipolar Electrodes for Spatial Separation of H2 and O2 Evolution during Water Electrolysis and the Development of High-Voltage Fuel Cells, ACS Appl. Mater. Interfaces. 9 (2017) 23654–23661. https://doi.org/10.1021/acsami.7b04226.

[29] K. Dhara, R.M. Debiprosad, Review on nanomaterials-enabled electrochemical sensors for ascorbic acid detection, Anal. Biochem. 586 (2019) 113415. https://doi.org/10.1016/j.ab.2019.113415.

[30] A. Mahajan, S. Banik, D. Majumdar, S.K. Bhattacharya, Anodic Oxidation of Butan-1-ol on Reduced Graphene Oxide-Supported Pd–Ag Nanoalloy for Fuel Cell Application, ACS Omega. 4 (2019) 4658–4670. https://doi.org/10.1021/acsomega.8b03561.

[31] Z. Tao, Q. Zhang, X. Xi, G. Hou, L. Bi, A strategy of tailoring stable electrolyte material for high performance proton-conducting solid oxide fuel cells (SOFCs), Electrochem. Commun. 72 (2016) 19–22. https://doi.org/10.1016/j.elecom.2016.08.019.

[32] N. Fujiwara, S. Yamazaki, Z. Siroma, T. Ioroi, K. Yasuda, Direct oxidation of l-ascorbic acid on a carbon black electrode in acidic media and polymer electrolyte fuel cells, Electrochem. Commun. 8 (2006) 720–724. https://doi.org/10.1016/j.elecom.2006.02.021.

[33] D. Sebastián, A. Serov, I. Matanovic, K. Artyushkova, P. Atanassov, A.S. Aricò, V. Baglio, Insights on the extraordinary tolerance to alcohols of Fe-N-C cathode catalysts in highly performing direct alcohol fuel cells, Nano Energy. 34 (2017)

195–204. https://doi.org/10.1016/j.nanoen.2017.02.039.

[34] D. Sebastián, A. Serov, K. Artyushkova, J. Gordon, P. Atanassov, A.S. Aricò, V. Baglio, High Performance and Cost-Effective Direct Methanol Fuel Cells: Fe-N-C Methanol-Tolerant Oxygen Reduction Reaction Catalysts, ChemSusChem. 9 (2016) 1986–1995. https://doi.org/10.1002/cssc.201600583.

[35] D.K. Ross, Hydrogen storage: The major technological barrier to the development of hydrogen fuel cell cars, Vacuum. 80 (2006) 1084–1089. https://doi.org/10.1016/j.vacuum.2006.03.030.

[36] Z.M. Bhat, R. Thimmappa, M.C. Devendrachari, S.P. Shafi, S. Aralekallu, A.R. Kottaichamy, M. Gautam, M.O. Thotiyl, A Direct Alcohol Fuel Cell Driven by an Outer Sphere Positive Electrode, J. Phys. Chem. Lett. 8 (2017) 3523–3529. https://doi.org/10.1021/acs.jpclett.7b01418.

[37] O. Muneeb, E. Do, T. Tran, D. Boyd, M. Huynh, G. Ghosn, J.L. Haan, A direct ascorbate fuel cell with an anion exchange membrane, J. Power Sources. 351 (2017) 74–78. https://doi.org/10.1016/j.jpowsour.2017.03.068.

[38] B.R. Sathe, A scalable and facile synthesis of carbon nanospheres as a metal free electrocatalyst for oxidation of l -ascorbic acid: Alternate fuel for direct oxidation fuel cells, J. Electroanal. Chem. 799 (2017) 609–616. https://doi.org/10.1016/j.jelechem.2017.03.049.

[39] M. Choun, H.J. Lee, J. Lee, Positively charged carbon electrocatalyst for enhanced power performance of L-ascorbic acid fuel cells, J. Energy Chem. 25 (2016) 793–797. https://doi.org/10.1016/j.jechem.2016.05.006.

[40] S. Uhm, J. Choi, S.T. Chung, J. Lee, Electrochemically oxidized carbon anode in direct l-ascorbic acid fuel cells, Electrochim. Acta. 53 (2007) 1731–1736.

https://doi.org/10.1016/j.electacta.2007.08.034.

[41] N. Fujiwara, S. Yamazaki, Z. Siroma, T. Ioroi, K. Yasuda, l-Ascorbic acid as an alternative fuel for direct oxidation fuel cells, J. Power Sources. 167 (2007) 32–38. https://doi.org/10.1016/j.jpowsour.2007.02.023.

[42] A. Brouzgou, E. Gorbova, Y. Wang, S. Jing, A. Seretis, Z. Liang, P. Tsiakaras, Nitrogen-doped 3D hierarchical ordered mesoporous carbon supported palladium electrocatalyst for the simultaneous detection of ascorbic acid, dopamine, and glucose, Ionics (Kiel). 25 (2019) 6061–6070. https://doi.org/10.1007/s11581-019-03116-z.

[43] F. Yang, J. Wang, Y. Cao, L. Zhang, X. Zhang, A highly sensitive ascorbic acid sensor based on carbon-supported CoPd nanoparticles, Sensors Actuators B Chem. 205 (2014) 20–25. https://doi.org/10.1016/j.snb.2014.08.050.

[44] C.D. Shruthi, Y. Venkataramanappa, G.S. Suresh, Reduced MWCNTs/Palladium Nanotubes Hybrid Fabricated on Graphite Electrode for Simultaneous Detection of Ascorbic Acid, Dopamine and Uric Acid, J. Electrochem. Soc. 165 (2018) B458–B465. https://doi.org/10.1149/2.1161810jes.

[45] O. Muneeb, E. Do, D. Boyd, J. Perez, J.L. Haan, PdCu/C anode catalysts for the alkaline ascorbate fuel cell, Appl. Energy. 235 (2019) 473–479. https://doi.org/10.1016/j.apenergy.2018.10.073.

[46] M.M. Hasan, Y. Nagao, Christmas-Tree-Shaped Palladium Nanostructures Decorated on Glassy Carbon Electrode for Ascorbic Acid Oxidation in Alkaline Condition, ChemistrySelect. 6 (2021) 5885–5892. https://doi.org/10.1002/slct.202100974.

[47] T. Sun, Z. Zhang, J. Xiao, C. Chen, F. Xiao, S. Wang, Y. Liu, Facile and Green

Synthesis of Palladium Nanoparticles-Graphene-Carbon Nanotube Material with High Catalytic Activity, Sci. Rep. 3 (2013) 2527. https://doi.org/10.1038/srep02527.

[48] A. Bin Yousaf, M. Imran, A. Zeb, X. Xie, K. Liang, X. Zhou, C.Z. Yuan, A.W. Xu, Synergistic effect of graphene and multi-walled carbon nanotubes composite supported Pd nanocubes on enhancing catalytic activity for electro-oxidation of formic acid, Catal. Sci. Technol. 6 (2016) 4794–4801. https://doi.org/10.1039/C5CY02217G.

[49] Y. She, Z. Lu, W. Fan, S. Jewell, M.K.H. Leung, Facile preparation of PdNi/rGO and its electrocatalytic performance towards formic acid oxidation, J. Mater. Chem. A. 2 (2014) 3894. https://doi.org/10.1039/c3ta14546h.

[50] H. Ye, Y. Li, J. Chen, J. Sheng, X.Z. Fu, R. Sun, C.P. Wong, PdCu alloy nanoparticles supported on reduced graphene oxide for electrocatalytic oxidation of methanol, J. Mater. Sci. 53 (2018) 15871–15881. https://doi.org/10.1007/s10853-018-2759-5.

[51] G. Hu, F. Nitze, T. Sharifi, H.R. Barzegar, T. Wågberg, Self-assembled palladium nanocrystals on helical carbon nanofibers as enhanced electrocatalysts for electro-oxidation of small molecules, J. Mater. Chem. 22 (2012) 8541. https://doi.org/10.1039/c2jm16075g.

[52] Y. Wu, Lithium Intercalation into Graphene Ribbons of Glassy Carbon, Int. J. Electrochem. Sci. 12 (2017) 1004–1013. https://doi.org/10.20964/2017.02.48.

[53] A.A. Rafati, A. Afraz, A. Hajian, P. Assari, Simultaneous determination of ascorbic acid, dopamine, and uric acid using a carbon paste electrode modified with multiwalled carbon nanotubes, ionic liquid, and palladium nanoparticles,

Microchim. Acta. 181 (2014) 1999–2008. https://doi.org/10.1007/s00604-014-1293-7.

[54] C. Lu, W. Guan, T.K.A. Hoang, Y. Li, T.N.L. Doan, H. Zhao, A novel synthetic strategy for pd3sn nanoparticles loaded reduced graphene oxide as electrocatalyst for the ethanol-tolerant oxygen reduction reaction, Int. J. Electrochem. Sci. 10 (2015) 5077–5085.

[55] Y. Lu, W. Chen, PdAg Alloy Nanowires: Facile One-Step Synthesis and High Electrocatalytic Activity for Formic Acid Oxidation, ACS Catal. 2 (2012) 84–90. https://doi.org/10.1021/cs200538g.

[56] X.L. Xing, Y.F. Zhao, H. Li, C.T. Wang, Q.X. Li, W. Bin Cai, High Performance Ag Rich Pd-Ag Bimetallic Electrocatalyst for Ethylene Glycol Oxidation in Alkaline Media, J. Electrochem. Soc. 165 (2018) J3259–J3265. https://doi.org/10.1149/2.0311815jes.

[57] K.M. Hassan, A.A. Hathoot, R. Maher, M. Abdel Azzem, Electrocatalytic oxidation of ethanol at Pd, Pt, Pd/Pt and Pt/Pd nano particles supported on poly 1,8-diaminonaphthalene film in alkaline medium, RSC Adv. 8 (2018) 15417–15426. https://doi.org/10.1039/C7RA13694C.

[58] B. Habibi, S. Mohammadyari, Facile synthesis of Pd nanoparticles on nano carbon supports and their application as an electrocatalyst for oxidation of ethanol in alkaline media: The effect of support, Int. J. Hydrogen Energy. 40 (2015) 10833–10846. https://doi.org/10.1016/j.ijhydene.2015.07.021.

[59] M. Abu Zahed, S.C. Barman, M. Sharifuzzaman, X. Xuan, J.S. Nah, J.Y. Park, Ex Situ Synthesis of Hexagonal NiO Nanosheets and Carboxyl-Terminated Reduced Graphene Oxide Nanocomposite for Non-Enzymatic Electrochemical Detection

of H2O2 and Ascorbic Acid, J. Electrochem. Soc. 165 (2018) B840–B847. https://doi.org/10.1149/2.0621816jes.

[60] K. Karaboduk, Electrochemical Determination of Ascorbic Acid Based on AgNPs/PVP-Modified Glassy Carbon Electrode, ChemistrySelect. 4 (2019) 6361–6369. https://doi.org/10.1002/slct.201901102.

[61] M. Saleh Mohammadnia, E. Marzi Khosrowshahi, E. Naghian, A. Homayoun Keihan, E. Sohouli, M.E. Plonska-Brzezinska, Ali-Sobhani-Nasab, M. Rahimi-Nasrabadi, F. Ahmadi, Application of carbon nanoonion-NiMoO4-MnWO4 nanocomposite for modification of glassy carbon electrode: Electrochemical determination of ascorbic acid, Microchem. J. 159 (2020) 105470. https://doi.org/10.1016/j.microc.2020.105470.

[62] S. Duzmen, A.K. Baytak, M. Aslanoglu, A novel voltammetric platform composed of poly(aminopyrazine), ZrO2 and CNTs for a rapid, sensitive and selective determination of ascorbic acid in pharmaceuticals and food samples, Mater. Chem. Phys. 252 (2020) 123170. https://doi.org/10.1016/j.matchemphys.2020.123170.

Chapter 4

Palladium Nanoparticles with Reduced Graphene Oxide and Multiwall Carbon Nanotubes Hybrid nanocomposite for Direct Alkaline Ascorbic Acid Fuel Cell

4.1 Abstract

The use of ascorbic acid (Vitamin C) as a sustainable alternative fuel for alkaline direct liquid fuel cells (DLFCs) has been explored. The potential anode catalyst is synthesized by incorporating palladium nanoparticles (Pd NPs) into reduced graphene oxide (rGO) and multiwall carbon nanotubes (MWCNT) hybrid nanocomposite (Pd/rGO/MWCNT) via a chemical reduction process and applied in ascorbic acid (AA) electrooxidation. The properties of Pd/rGO/MWCNT are characterized using scanning electron microscopy (SEM), energy-dispersive X-ray spectroscopy (EDX), X-ray photoelectron spectroscopy (XPS), transmission electron microscopy (TEM), X-ray powder diffraction (XRD), and Brunauer−Emmett−Teller (BET). The electrocatalytic performance is investigated by the cyclic voltammetry (CV) method. The Pd/rGO/MWCNT modified glassy carbon electrode (Pd/rGO/MWCNT/GCE) exhibited a high current density of 17.6 mA cm^{-2} than the unmodified GCE (0.6 mA cm^{-2}) for AA electrooxidation. The prepared Pd/rGO/MWCNT/GCE also showed excellent stability. At 60 °C, the fuel cell generates a maximum power density of 9.54 mW cm^{-2} with an open-circuit voltage of 0.88 V while supplying 1 M AA + 2 M KOH as the anode fuel and humidified oxygen as the cathode fuel.

4.2 Introduction

The noble Pd catalyst, which was studied in the previous chapter, demonstrated outstanding electrocatalytic activity. We devised a novel Pd-based anode catalyst to develop the fuel cell system. In this chapter, we will discuss the performance of the new catalyst in detail. We will also propose an environmentally friendly AA-based fuel cell system in this chapter, which might alleviate the energy problem along with reducing the greenhouse impact.

Recently electrochemical energy storage and conversion devices have achieved much attention from scientists to address climate change [1–6]. Fuel cells are a promising candidate due to having potential zero-emission energy conversion devices [7–10]. Different fuel cells like alcohol-based fuel cells, borohydride fuel cells, hydrazine fuel cells, hydrogen fuel cells, etc are anticipated by the safety, environmental, and storage issues [11–14]. Ascorbic acid (AA), known as Vitamin C, is another possible fuel to be used in direct liquid fuel cells (DLFCs) because of its natural abundance, producing nontoxic by-products [15–19]. In the electrochemical oxidation process, AA releases two electrons and two protons [20,21]. The DLFCs performance could be improved by developing a better electrocatalyst for AA electrooxidation.

Carbon-based materials have glittered much attention in the field of electrocatalysis, owing to their outstanding physical and chemical properties [22,23]. Carbon-based electrodes are easily renewable. Using carbon or carbon-based materials has many advantages other than renewability, including easy preparation, high stability, reproducibility, can be easily distributed into the paste, and good conductivity [24]. Researchers have been reported that conductive materials could be used as transductive materials at an electrocatalyst-electrode interface for fast electron transfer [25].

Graphene is sp^2 bonded two-dimensional carbon material with a honeycomb structure. It is broadly used in catalyst applications for its excellent properties like large surface area, highly conductive, and biocompatibility [26]. Graphite oxide (GO) can easily be prepared by the oxidation of graphite powder and the reduction of GO is called reduced graphene oxide (rGO) [27,28]. GO has oxygen-containing functional groups resulting in less conductive materials than rGO and can increase the resistance [22,29]. Several methods have already been reported for the preparation of rGO from GO such as chemical, thermal, and hydrothermal technique [30–32]. The chemical reduction method has several benefits such as high stability, cost-effectiveness, and shorter production time [33]. However, the π-π interaction between graphene layers causes agglomeration of rGO that hindrance its electrical performance that exhibits low surface area [34]. The stacking effect of graphene sheets has been a critical issue for catalytic performance. Multiwall carbon nanotubes (MWCNTs) are generally used to improve electrocatalytic performance. MWCNTs have high mechanical strength, a large surface area, and are chemically stable [35]. It is well known that MWCNTs can combine with rGO through Vander Waals forces and hydrogen bonds. Thus, MWCNTs could be used as a spacer between the interfacial graphene layers during the reduction process of rGO to resist agglomeration and increase the specific surface area [34,36].

To further improvement of the catalytic performance, researchers have introduced metal nanoparticles (NPs) into the rGO and MWCNTs hybrid nanocomposite [30,34,37–39]. Superior electrocatalytic effectiveness makes novel metals of Pt and Pd, the most promising candidates of anode catalysts in energy conversion and storage devices [40–42]. Pd-based anode catalyst shows higher performance than Pt in the electrocatalytic oxidation of AA [43–45]. Pd NPs decorated rGO and MWCNTs hybrid nanocomposite

could lead to improve electrocatalytic oxidation of AA. Several research works have been reported the incorporation of Pd NPs in the rGO and MWCNTs hybrid nanocomposite for catalytic performance [30,37,38,43,46,47]. Besides, one-pot synthesis of the chemical reduction method is preferable due to easy and shorter time preparation. In this chapter, a simple one-pot synthesis process is developed for Pd NPs decorated rGO and MWCNTs hybrid nanocomposite (Pd/rGO/MWCNT) for AA electrooxidation.

The alkaline DLFCs offer benefits over the acidic DLFCs. Water is generated at the anode in alkaline DLFCs, thus water management is negligible, and the cathode has little effect on total fuel cell efficiency. Alkaline fuel cells provide a lower activation overpotential, quicker reaction kinetics, and a less toxic and corrosive environment for fuel cell components, particularly metal catalysts [15]. Finally, the liquid fuels utilized in the alkaline DLFC are easier to handle, store, and transport than hydrogen. The direct alkaline AA-based DLFC (DAAFC) also showed better performance than acidic conditions [48]. Hence the synthesized hybrid nanocomposite is used as an anode catalyst to check the DAAFC.

4.3 Experimental

4.3.1 Chemicals and Instruments

Analytical grade MWCNT, AA, sodium tetrachloropalladate (II) (Na_2PdCl_4), 5% Nafion solution, sodium borohydride ($NaBH_4$), sulfuric acid (H_2SO_4), potassium hydroxide (KOH), were purchased from Fujifilm Wako Pure Chemical Corp and used as received. GO was purchased from NiSiNa materials Co. Ltd. All the necessary solutions were

prepared by Milli-Q water. All the experiments were conducted in alkaline condition under deaeration and at room temperature (25 °C ± 0.5 °C).

The purity of the MWCNTs has been checked by thermogravimetric analysis (TGA) and Raman spectra (Figure 4.1a). The TGA was performed in air heated to 800 °C at a rate of 10 °C/min. The MWCNTs are extremely pure, with a carbon content of roughly 95 wt% (same as company specification) and can withstand a sintering temperature of up to 550 °C in the air without losing weight. This data is well-matched with previous data [49]. The Raman spectra of the MWCNTs is shown in Figure 4.1b. Two distinct peaks, corresponding to disordered carbon (D-bond) and ordered graphitic carbon (G-bond), can be seen at about 1340 and 1570 cm^{-1}, respectively. These two peaks further proved the high purity of the MWCNTs [49].

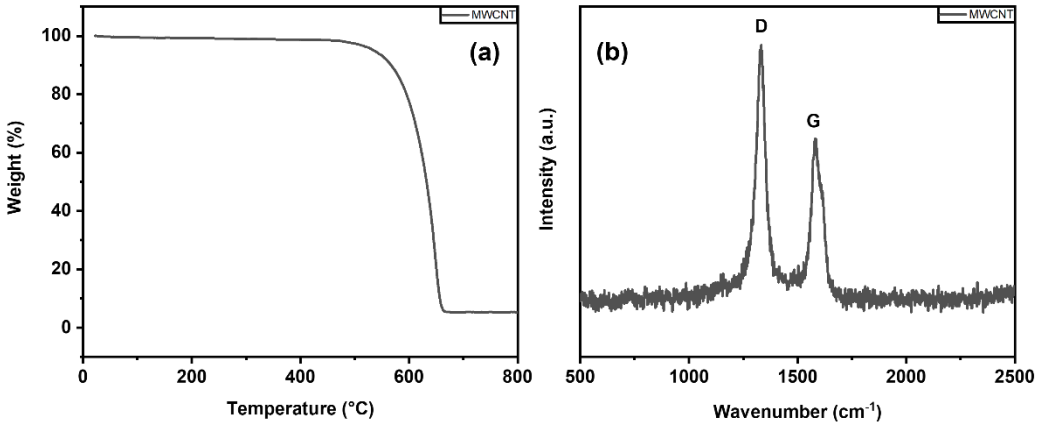

Figure 4.1 Characterization of MWCNT (a) TGA, (b) Raman spectra.

4.3.2 Synthesis of the nanocomposite

Different catalysts named Pd/rGO/MWCNT, Pd/rGO, and rGO/MWCNT were synthesized by a chemical reduction method employing $NaBH_4$ as the reductant. For the preparation of Pd/rGO/MWCNT, 20 mg of GO and 20 mg MWCNT were

homogeneously dispersed in 20 mL deionized water by ultrasonication. 5.0 mL of 15 mM of Na_2PdCl_4 (dissolved in 0.1 M H_2SO_4) solution was added and the solution was treated by ultrasonication for another 30 min. Then dropwise added 7.6 mL of 0.5 M $NaBH_4$ (freshly-prepared) into the reactant slowly until the solution pH ~10. The reactant was then stirred for 4 h at room temperature. After that catalyst was filtered with filter paper and washed with deionized water and ethanol three times, respectively. Finally, the catalyst was dried at 30 ^{0}C in a vacuum oven (12 h). The methods for preparing the other two catalysts were as described above but only metal precursor and GO was added in the case of Pd/rGO. For rGO/MWCNT no additional metal precursor was added.

4.3.3 Characterizations

The morphology of the as-prepared catalysts was characterized by field-emission scanning electron microscopy (FE-SEM, S4100; Hitachi Ltd.) and scanning electron microscope (SEM) coupled with energy-dispersive X-ray spectroscopy (EDX, TM3030Plus miniscope; Hitachi Ltd.). For elemental analysis of catalysts, X-ray photoelectron spectroscopy (XPS) measurements were taken on a delay-line detector (DLD) spectrometer (Kratos Axis-Ultra; Kratos Analytical Ltd.) with an Al Kα radiation source (1486.6 eV). Transmission electron microscopy (TEM) (H-7100; Hitachi Ltd.) was used to check the size of Pd NPs. Powder X-ray diffractometer (XRD) patterns were recorded on a fully automatic horizontal multi-purpose X-ray diffractometer (Rigaku Smartlab; Rigku Corp.) as a 2θ range from 20° to 90°. The surface area of the catalysts was obtained by the Brunauer−Emmett−Teller (BET) method using BELSORP-miniII-BP. All the electrochemical measurements were taken using a potentiostat CHI 701

having a three-electrode system. The GCE (3 mm diameter), Ag/AgCl (sat. KCl), Pt wire was used as a working electrode, reference, and counter electrodes, respectively.

4.3.4 Modification of GCE

The GCE surface was cleaned by rubbing with alumina powder (0.05 µm diameter), and then removing the impurities by sonication with ethanol and water for 10 min, respectively. Then the GCE surface was cleaned electrochemically by potential cycling in 0.1 M H_2SO_4 (Ar saturated) from 0 V to +1.0 V at a scan rate of 100 mV s^{-1} and dry at room temperature. To investigate AA electrooxidation, the GCE was modified with a catalyst suspension solution. The catalyst ink solution was prepared by the addition of 2 mg Pd/rGO/MWCNT into 200 µL of 0.25% Nafion-ethanol solution and sonicate for a homogeneous mixture. Then catalyst ink solution was dropped onto the clean GCE surface containing 0.04 mg Pd and dried at room temperature. The modified electrode was named Pd/rGO/MWCNT/GCE whereas Pd/rGO/GCE and rGO/MWCNT/GCE for Pd/rGO and rGO/MWCNT, respectively. The detailed preparation of Pd/rGO/MWCNT/GCE is shown in scheme 4.1.

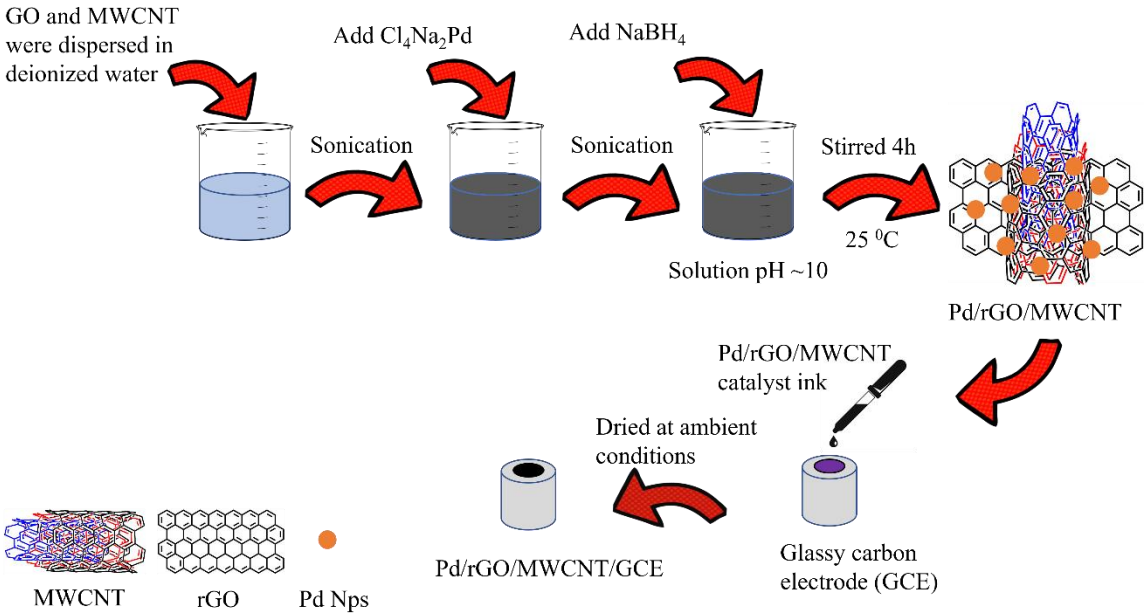

Scheme 4.1 Preparation of Pd/rGO/MWCNT/GCE.

4.3.5 Fuel cell testing

The Pd/rGO/MWCNT catalyst was further used to construct a DAAFC. The anode and cathode catalysts were Pd/rGO/MWCNT and Pt/C respectively. The amount of catalyst loading is 2 mg/cm^2 of Pd for the anode and 2 mg/cm^2 of Pt for the cathode. The Tokuyama A201 membrane and AS-4 ionomer were used for the preparation of membrane electrode assembly (MEA). The catalyst to ionomer ratio was 1:4 wt% for both anode and cathode. The carbon paper TGP-H-060 was used for the gas diffusion layer (GDL). The MEA was prepared by a customized hot press instrument, where catalyst coated GDLs and A-201 membrane was pressed under 1 MPa for 3 minutes at 130 °C. The anode fuel was the combination of 1 M AA + 2 M KOH (1 mL/min) whereas, humidified O_2 was supplied as cathode fuel (100 mL/min).

4.4 Results and Discussion

4.4.1 Morphological and elemental analysis

Figure 4.2a displays FE-SEM images of the as-prepared Pd/rGO/MWCNT. Figure 4.2b shows a high magnification image of one part of Pd/rGO/MWCNT. The wrinkles in the image indicate that rGO in Pd/rGO/MWCNT was well reduced by the chemical reduction process [25]. The FE-SEM image of GO, Pd/rGO, and rGO/MWCNT are also shown in Figure 4.3. In comparison to the GO, the surface morphology of all synthesized materials was completely changed. This suggested that the GO was properly reduced. EDX image of the Pd/rGO/MWCNT is shown in Figure 4.2c. The bright spots are due to the presence of Pd metal. A similar observation was also found in the case of Pd/rGO (Figure 4.3c). Elemental mapping of C, O, and Pd is shown in Figure 4.2d, 4.2e, and 4.2f, respectively. Elemental mapping revealed the presence of Pd metal into the rGO and MWCNT system homogenously. Figure 4.2g shows the atomic ratio of the Pd/rGO/MWCNT. This also revealed the presence of Pd. A small amount of oxygen is found in the EDX mapping. This is due to the oxidation of Pd metal, which is also found in XPS analysis.

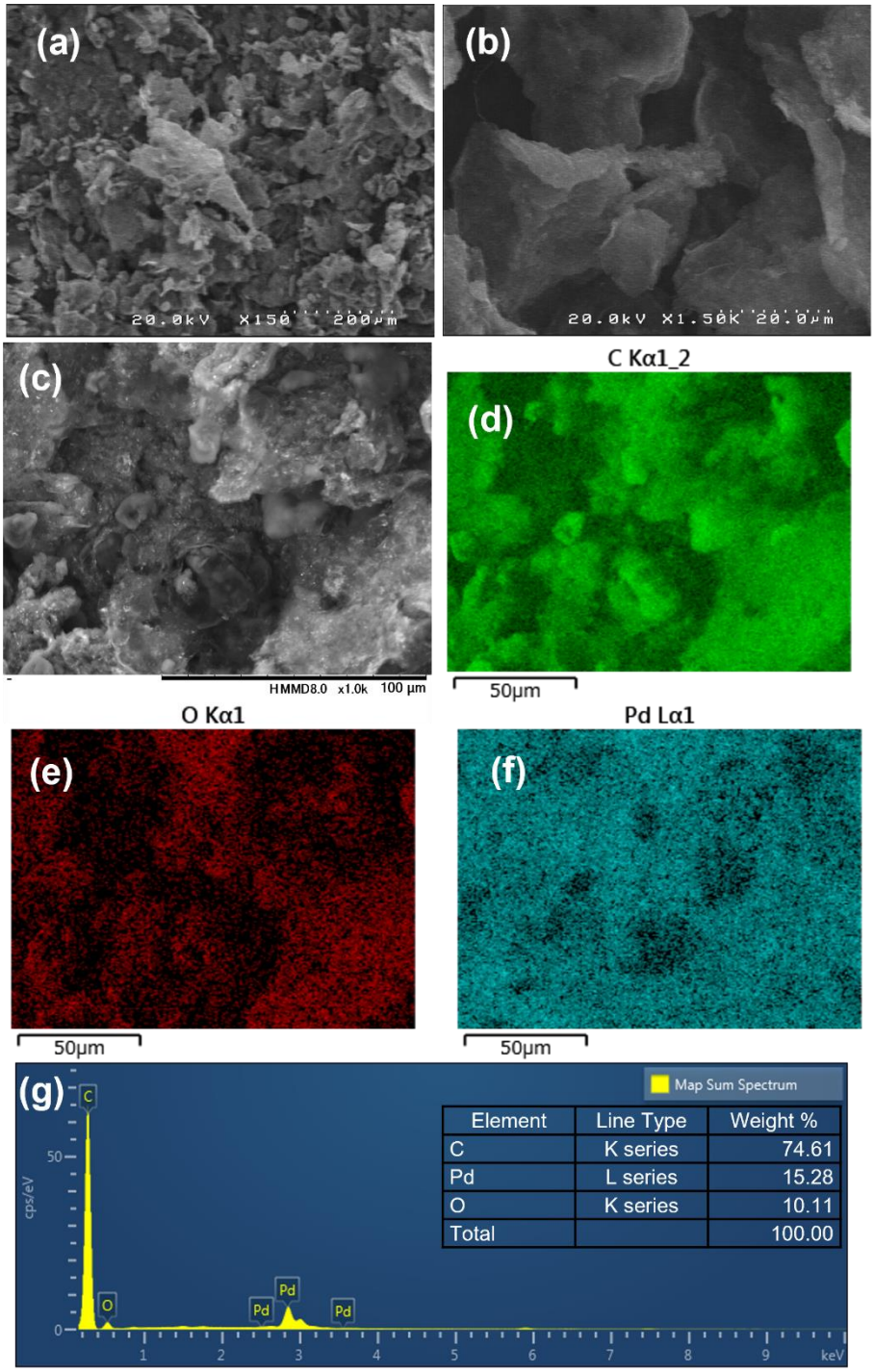

Figure 4.2 FE-SEM image of the (a) Pd/rGO/MWCNT (b) high magnification of Pd/rGO/MWCNT; EDX image of (c) Pd/rGO/MWCNT, elemental mapping of (d) C, (e) O, (f) Pd, (g) atomic ratio of Pd/rGO/MWCNT (inset table: atomic weight ratio).

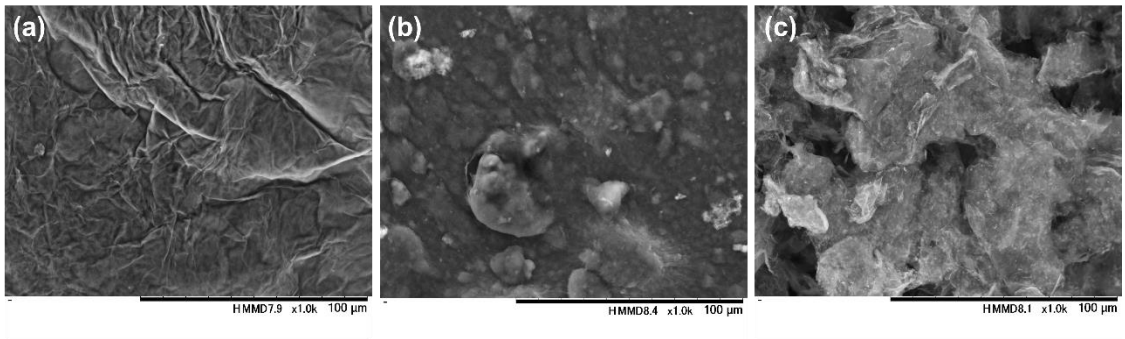

Figure 4.3. SEM images (a) GO, (b) rGO/MWCNT and (c) Pd/rGO

XPS analysis was conducted to check the oxidation state of carbon and Pd metal (Figure 4.4a and 4.4b). XPS is a powerful technique to check the successful reduction of GO, as the oxo groups in C 1s XPS spectra will be lower in the case of rGO. C 1s XPS data of the GO is shown in Figure 4.5a. In the case of GO, the deconvoluted C 1s suggested the presence of C–C, C-O, and C=O corresponding to the binding energies of 284.5 eV, 286.6 eV, and 288.2 eV, respectively [50,51]. The deconvoluted C 1s peak of Pd/rGO/MWCNT is shown in Figure 4.4a, where the C-O signal is much less pronounced and the peak for C=O is very weak, indicating a successful reduction of GO [50]. The deconvoluted C 1s spectra of rGO/MWCNT and Pd/rGO also shows similar features are displayed in Figure 4.5b and 4.5c, respectively. This suggested that in all cases the GO is chemically reduced successfully. The π-π^* interaction peak was found at binding energy 291.1 eV in the case of both Pd/rGO/MWCNT (Figure 4.4a) and Pd/rGO (Figure 4.5c) [50]. Figure 4.4b shows the Pd 3d XPS spectra of Pd/rGO/MWCNT. Two major peaks were observed at binding energies of 340.8 eV and 335.6 eV representing Pd ($3d_{3/2}$) and Pd ($3d_{5/2}$), respectively with 5.2 eV separation [31,37,39,50,52]. XPS data revealed that most of the Pd NPs are in the metallic state in Pd/rGO/MWCNT. That means Pd precursor is successfully converted to metal Pd by the chemical reduction

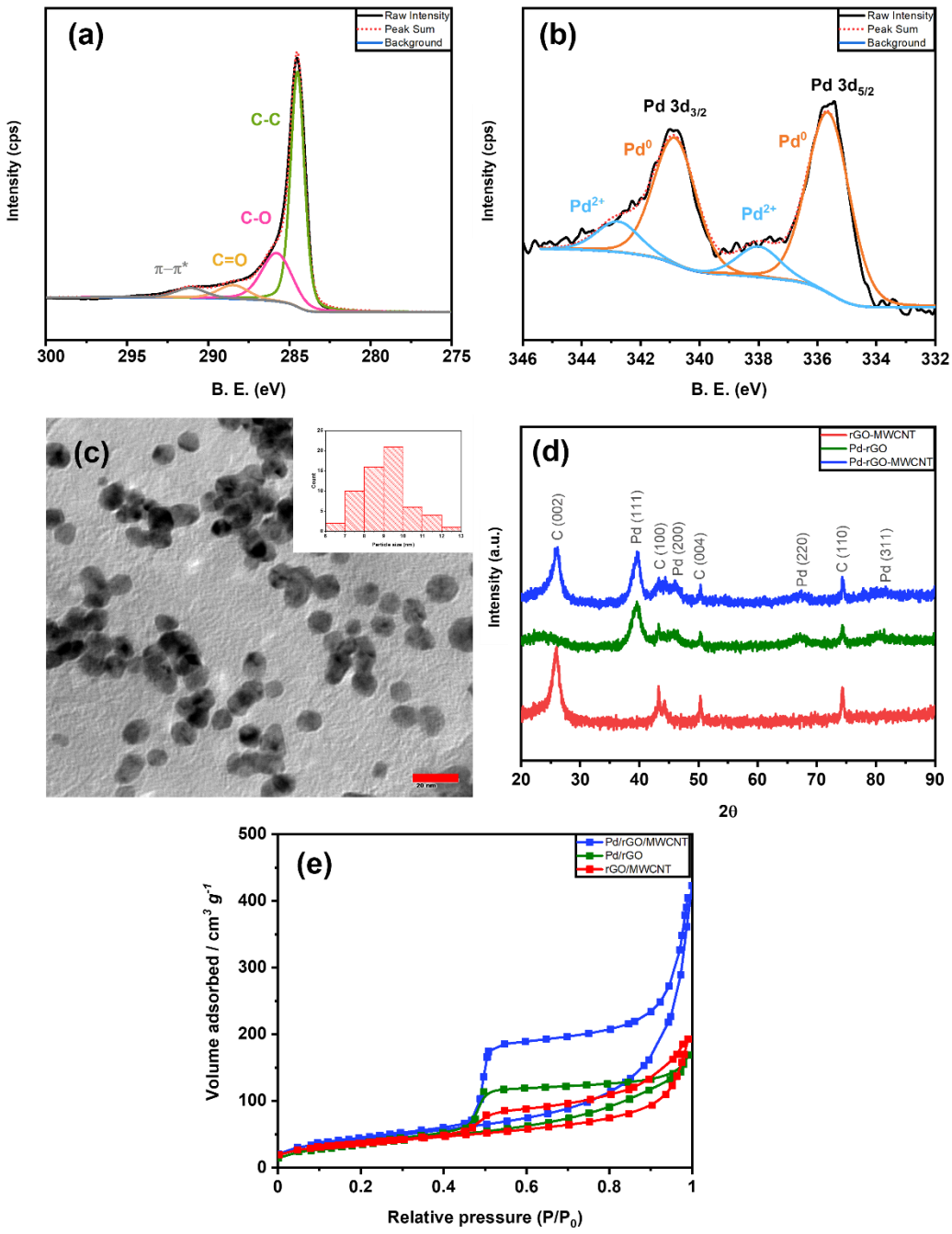

Figure 4.4 XPS spectra of Pd/rGO/MWCNT (a) C 1s and (b) Pd 3d; (c) TEM image of Pd/rGO/MWCNT (scale bar = 20 nm, inset: histogram of the Pd NPs); (d) XRD patterns of as-synthesized rGO/MWCNT, Pd/rGO, and Pd/rGO/MWCNT; (e) Nitrogen adsorption curves of Pd/rGO/MWCNT, Pd/rGO and rGO/MWCNT.

process. A small amount of PdO was found in XPS data at higher binding energy compared to metal Pd. In the case of Pd/rGO, the Pd 3d XPS spectrum was found with similar features compared to the Pd/rGO/MWCNT (Figure 4.5d). Pd 3d XPS data of Pd/rGO also revealed that most of the Pd metals are metallic states. The TEM image of Pd/rGO/MWCNT is displayed in Figure 4.4c. The synthesized Pd NPs are dispersed on the rGO/MWCNT support. Inset histogram displayed that the average size of the Pd NPs are approximately 9 nm. The TEM image revealed that most Pd NPs are round-shaped. XRD patterns shown in Figure 4.4d confirm the Pd diffraction peaks along with carbon. All the Pd contain catalyst has a similar diffraction pattern. The diffraction peak at 40.1° corresponds to the Pd (111) plane [52,53]. The peak at 25.8° for Pd/rGO/MWCNT and rGO/MWCNT corresponds to the C (002) to an interlayer spacing of 3.45 Å [54–56]. The disappearance of the C (002) diffraction peak in Pd/rGO composites due to less agglomeration of the rGO sheets [57]. The particle size of Pd NPs calculated by the Scherrer equation is 6 nm, which is close to the TEM statistics result [53]. N_2 adsorption and desorption test (BET analysis) was performed to investigate the surface area of all electrocatalysts as shown in Figure 4.4e. The BET-specific surface area and the total pore size of all catalysts are summarized in Table 4.1. The specific surface area of the Pd/rGO/MWCNT catalyst was higher than Pd/rGO and rGO/MWCNT. The adsorption analysis revealed that pore volume for Pd/rGO/MWCNT catalyst was also higher than others. The pore volume of the catalyst increased by the insertion of Pd and MWCNT between graphene layers. A combination of Pd and MWCNT with rGO in Pd/rGO/MWCNT will enhance the surface area as well as pore volume compare with Pd/rGO and rGO/MWCNT separately. The combination of two complementary materials, results in a synergistic effect, could improve the catalytic performance.

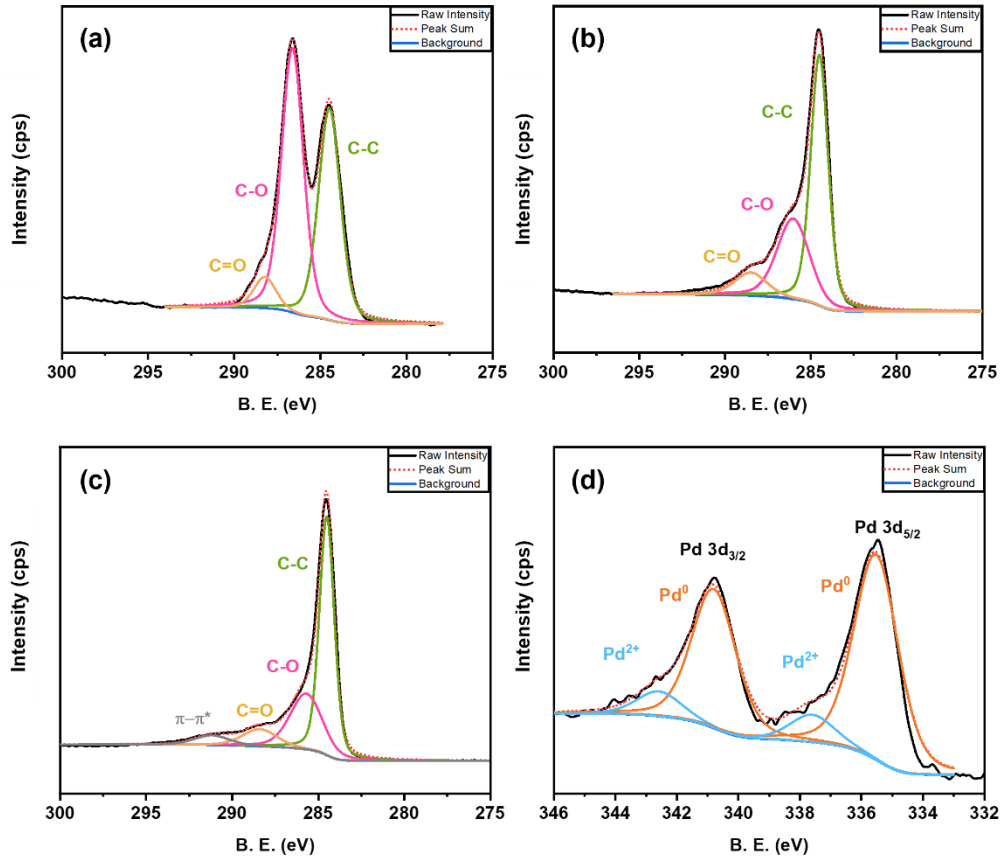

Figure 4.5 C 1s XPS spectra of (a) GO, (b) rGO/MWCNT, (c) Pd/rGO, and (d) Pd 3d XPS spectra of Pd/rGO.

Table 4.1 BET surface area and pore volume of Pd/rGO/MWCNT, Pd/rGO, and rGO/MWCNT.

Catalyst	BET surface area ($m^2 g^{-1}$)	Pore volume ($cm^3 g^{-1}$)
Pd/rGO/MWCNT	153.7	0.61
Pd/rGO	130.1	0.26
rGO/MWCNT	130.7	0.29

4.4.2 Electrocatalytic activity

To investigate the electrocatalytic performance of Pd/rGO/MWCNT/GCE towards the oxidation of AA molecules, cyclic voltammograms were recorded under different experimental conditions. First, the modified electrode response was checked in the presence of AA, shown in Figure 4.6a. Cyclic voltammograms were recorded between -0.3 V and +0.7 V in 1 M KOH solution in the absence and presence of AA molecules (5.6 mM) using Pd/rGO/MWCNT/GCE at a scan rate of 50 mV s^{-1}. A well-defined oxidation wave attributable to the oxidation of AA appears at +0.2 V whereas no oxidation peak in absence of AA. We further evaluate the catalytic improvement by comparing all the catalyst electrodes with the bare GCE. Figure 4.6b represents cyclic voltammograms of AA molecules using the bare GCE and all modified electrodes. Compared to bare GCE and other modified electrodes, the Pd/rGO/MWCNT/GCE shows the higher catalytic activity for AA electrooxidation. The Pd/rGO/MWCNT/GCE (17.6 mA cm^{-2}) exhibits a higher current density than the bare GCE (0.6 mA cm^{-2}). This is due to the synergetic effect of Pd NPs with the rGO and MWCNT hybrid nanocomposite. In the case of rGO/MWCNT/GCE, the current increased significantly due to a larger surface area of rGO and MWCNT hybrid nanocomposite. When Pd Nps incorporated into this hybrid nanocomposite, the electrocatalytic performance is enhanced considerably. Small size Pd NPs also play an important role in catalytic performance. The concentration effect of AA at the Pd/rGO/MWCNT/GCE surface was investigated and shown in Figure 4.6c at a scan rate of 50 mV s^{-1}. The oxidation current increased with the increasing concentration of AA. This observation suggests that the active site of the Pd/rGO/MWCNT catalyst does not affect by the concentration of AA. The peak potential of AA oxidation shifted positively with increasing concentration

which can be denoted as a diffusion-controlled reaction [58]. This change is due to a disruption of the analyte mass transportation mechanism. The current can be explained by the analyzer mass transfer from the bulk of the solution to the surface of the electrode.

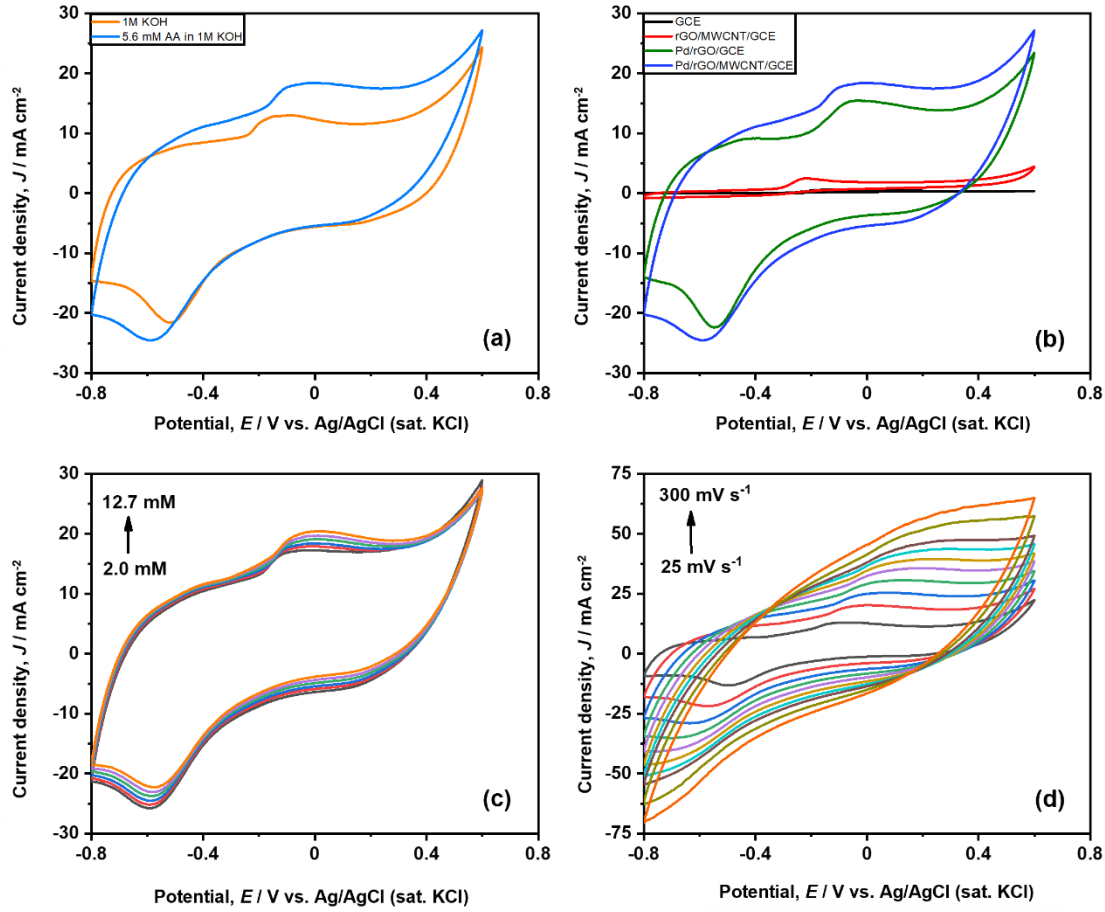

Figure 4.6 (a) Cyclic voltammograms of Pd/rGO/MWCNT/GCE in the absence and presence of 5.6 mM ascorbic acid. (b) Catalytic activity comparison of bare GCE, rGO/MWCNT/GCE, Pd/rGO/GCE, and Pd/rGO/MWCNT/GCE for 5.6 mM ascorbic acid at 50 mV s^{-1}. (c) Concentration effect of ascorbic acid at 50 mV s^{-1}. (d) Scan rate effect of 12.7 mM ascorbic acid using Pd/rGO/MWCNT/GCE catalyst. All the above experiments are in a 1 M KOH solution.

The rise in AA concentrations disrupts the process of diffusion, and the electrochemical system is more likely to restore mass transportation. The peak potential, therefore, changed positively. The influence of scan rates on AA oxidation is shown in Figure 4.6d. The Pd/rGO/MWCNT/GCE anodic peak current increased concomitantly with the increasing scan rate ranging from 25 to 500 mV s^{-1}. We further investigate the peak current behaviors with the scan rate effect. Figure 4.7 shows the log peak current (*Ip*) vs log (scan rate) curve. The plots revealed a linear relationship having a slope of 0.49, close to 0.5. From the slope value, it can be concluded that the AA oxidation at the Pd/rGO/MWCNT/GCE surface is controlled by the solution to the electrode surface mass transfer step [20,52].

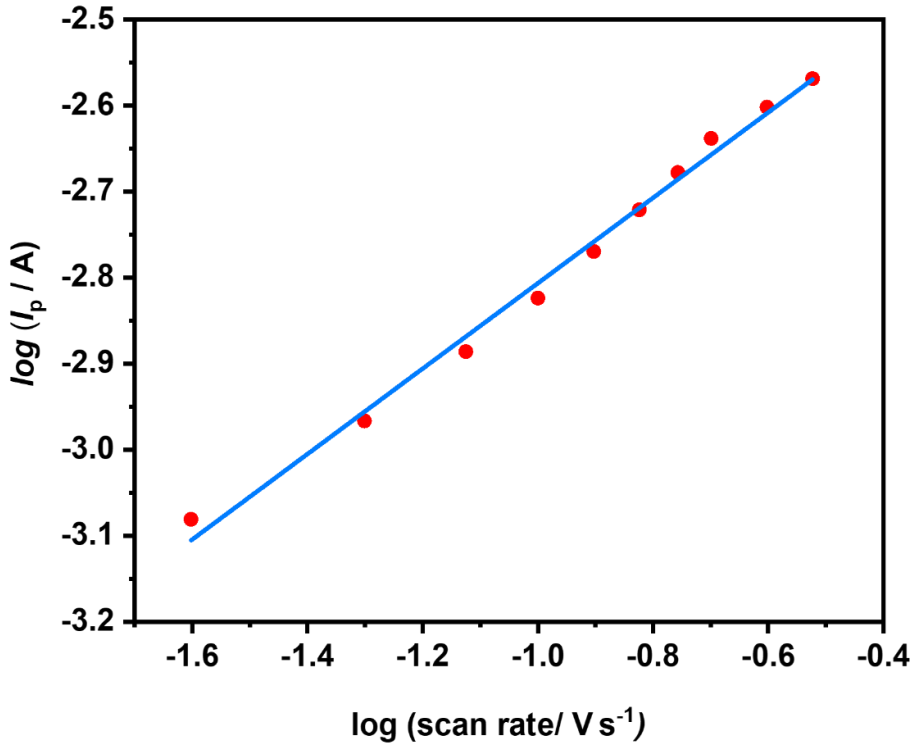

Figure 4.7 Log (I_p) vs. log (scan rate) plots. Experimental conditions are the same as those shown in Figure 4.6d.

Figure 4.8 showed the high concentration effect of ascorbic acid at Pd/rGO/MWCNT/GCE catalyst. With increasing the concentration the peak current density also increased. The Pd/rGO/MWCNT/GCE catalyst has similar electrochemical behaviors for AA oxidation in the low and high concentrations of AA solution.

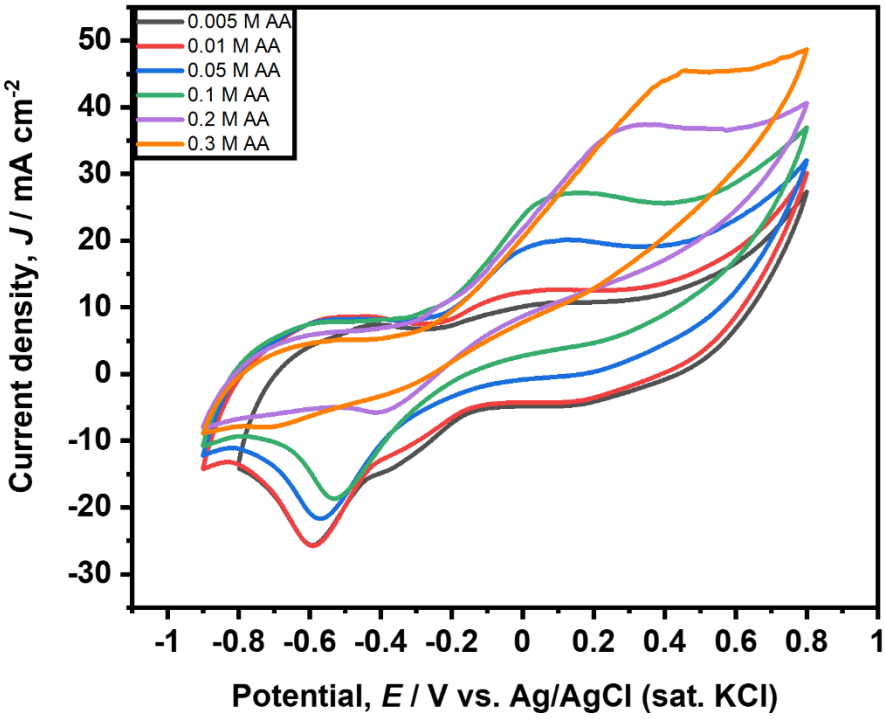

Figure 4.8 High concentration effect of ascorbic acid at Pd/rGO/MWCNT/GCE at 50 mV s^{-1} scan rate.

We further checked chronoamperometry for the electrochemical stability of all the modified electrodes [59]. The stability check by chronoamperometry of Pd/rGO/MWCNT/GCE, Pd/rGO/GCE, and rGO/MWCNT/GCE electrodes is shown in Figure 4.9, applying a working potential of peak potential of AA oxidation. After 1000 s the current density of Pd/rGO/MWCNT/GCE is still higher compared with the other two modified catalysts electrode. From Figure 4.9, the stability of

Pd/rGO/MWCNT/GCE for AA oxidation is quite high. From this data, we can say that the Pd/rGO/MWCNT catalyst could be a potential anode catalyst for AA fuel cell application.

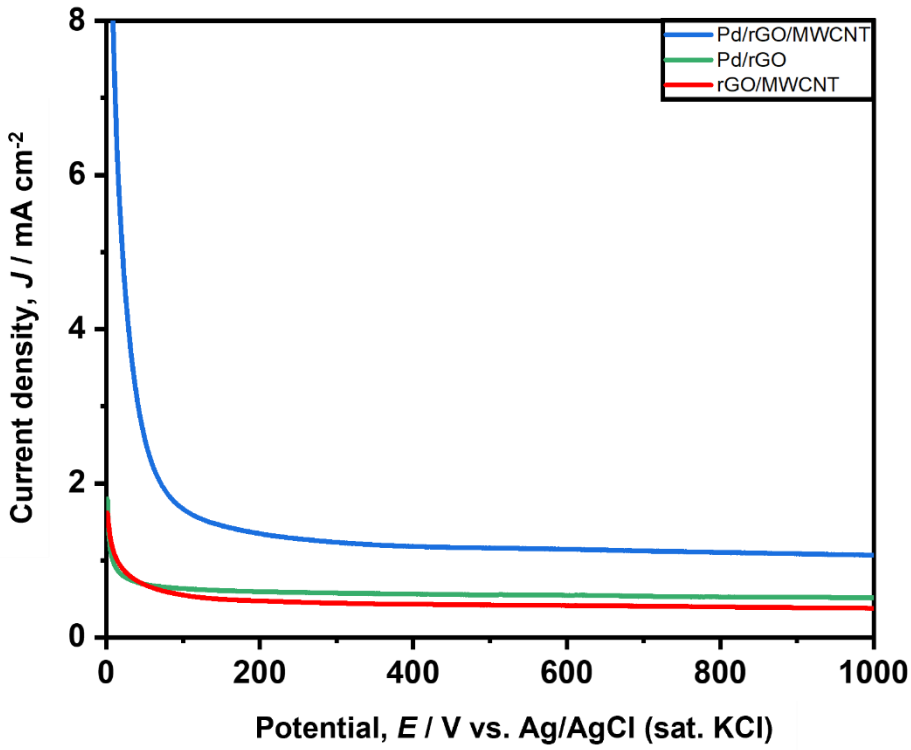

Figure 4.9 Chronoamperometry of 5 mM of ascorbic acid at rGO/MWCNT/GCE, Pd/rGO/GCE, and Pd/rGO/MWCNT/GCE.

We also compare our data with the reported data of Pd, rGO, and MWCNT based catalyst for AA electrooxidation summarized in Table 4.2. Pd/rGO/MWCNT/GCE shows the highest performance compared to previously reported results.

Table 4.2 Electrocatalytic performance comparison of Pd, rGO, and MWCNT based catalyst for ascorbic acid electrooxidation

Electrode	Peak current density ($\mu A\ cm^{-2}$)	Reference
Pd/rGO/MWCNT/GCE	17630	This work
Pd/MWCNT/IL/CPE	9004	[60]
Pd/GCE-0.1V_400S	4500	[52]
CoO/rGO/MWCNT/GCE	2321	[25]
SMT/MWCNTs/PGE	945	[35]
AuNR/MWCNT/GO/GCE	262	[22]

Note: IL= ionic liquid, CPE= carbon paste electrode, SMT= nano-smectite, PGE= graphite electrode, AuNR= gold nanorods.

The Pd/rGO/MWCNT exhibits very high catalytic performance with quite high stability. The noble metal Pd NPs insertion into the rGO and MWCNT hybrid nanocomposite increase the electrochemical active site for AA oxidation. The modified electrode Pd/rGO/MWCNT/GCE also has good stability with the highest performance for AA oxidation lead to the one step ahead for the construction of AA fuel cell.

4.4.3 Fuel Cell Performance

We establish an alkaline DLFC that uses ascorbic acid as anode fuel, humidified oxygen as an oxidant, a polymer anion exchange membrane, Pd/rGO/MWCNT anode catalysts, and platinum cathode catalysts. Figure 4.10 shows the voltage-current (VI) curves for a single cell DAAFC. At first, the voltage is decreased due to the energy barrier needed for the redox reactions of the electrodes in the fuel cells. Due to resistive losses in the fuel cell, especially inside the membrane, the slope reduces after the activation overpotential and continues downward. Finally, at low voltages, the slope begins to rise again, owing to mass transport losses caused by materials oxidization in high currents at the anode side. The maximum power output of DAAFC is 9.54 mW/cm^2 and the maximum current density is 126 mA cm^{-2} at an operating temperature of 60 °C with the OCV value +0.88 V.

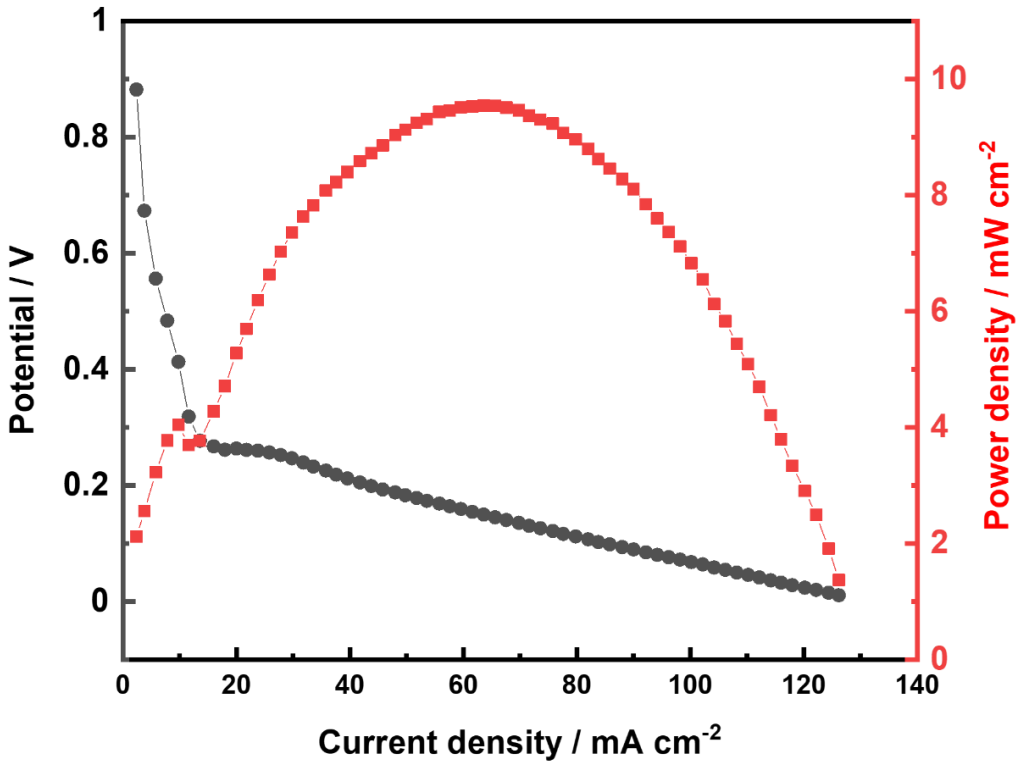

Figure 4.10 The VI plots for DAAFC at 60 °C using Pd/rGO/MWCNT as anode catalyst and Pt/C as cathode catalyst. Anode fuel flow rate is 1 mL/min (1 M AA + 2 M KOH) and cathode fuel 100 mL/min humidified O_2.

At various temperatures, the fuel cell performance was also assessed using the VI graphs mode. As demonstrated in Figure 4.11, the fuel cell performance improved from 40 to 60 °C. The highest performance was achieved at 60 °C. The difficulty of generating large current densities at lower temperatures is mostly due to the membrane conductivity. The optimum temperature for the DAAFC is 60 °C.

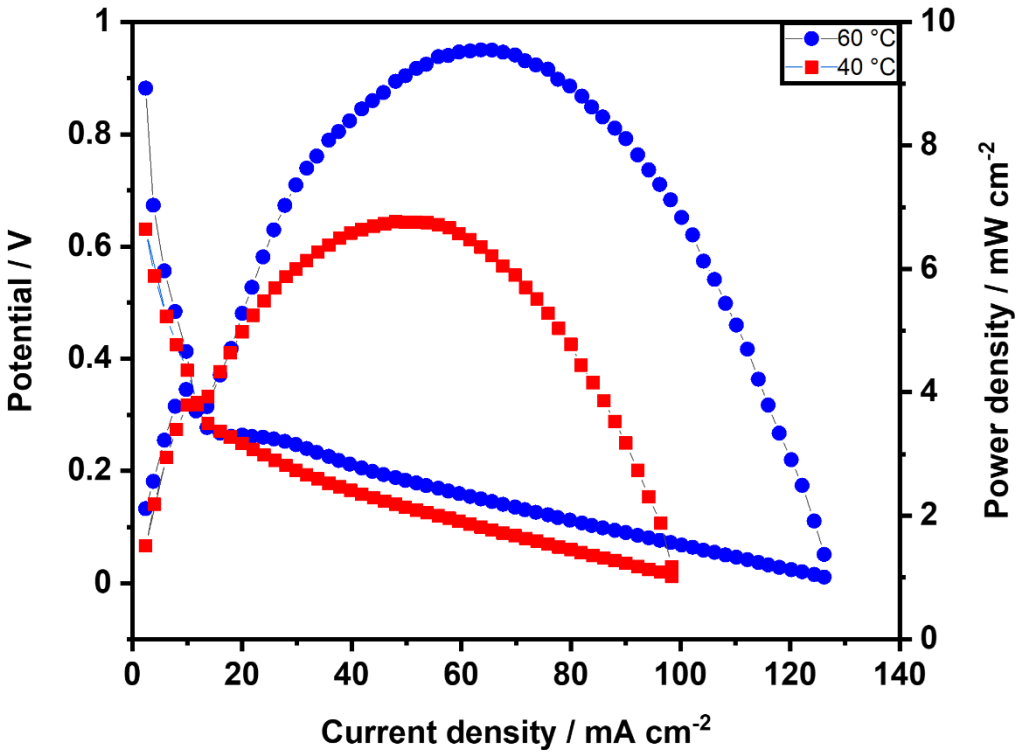

Figure 4.11 The VI plots for DAAFC at different operating temperatures using Pd/rGO/MWCNT as anode catalyst and Pt/C as cathode catalyst. Anode fuel flow rate is 1 mL/min (1 M AA + 2 M KOH) and cathode fuel 100 mL/min humidified O_2.

The oxidant also has an impact on the DAAFC performance. The supply of the humidified O_2 in the cathode side enhanced the performance compared to the dry O_2 (Figure 4.12). Humidified condition is needed to transport the OH- through the membrane from the cathode side to the anode side.

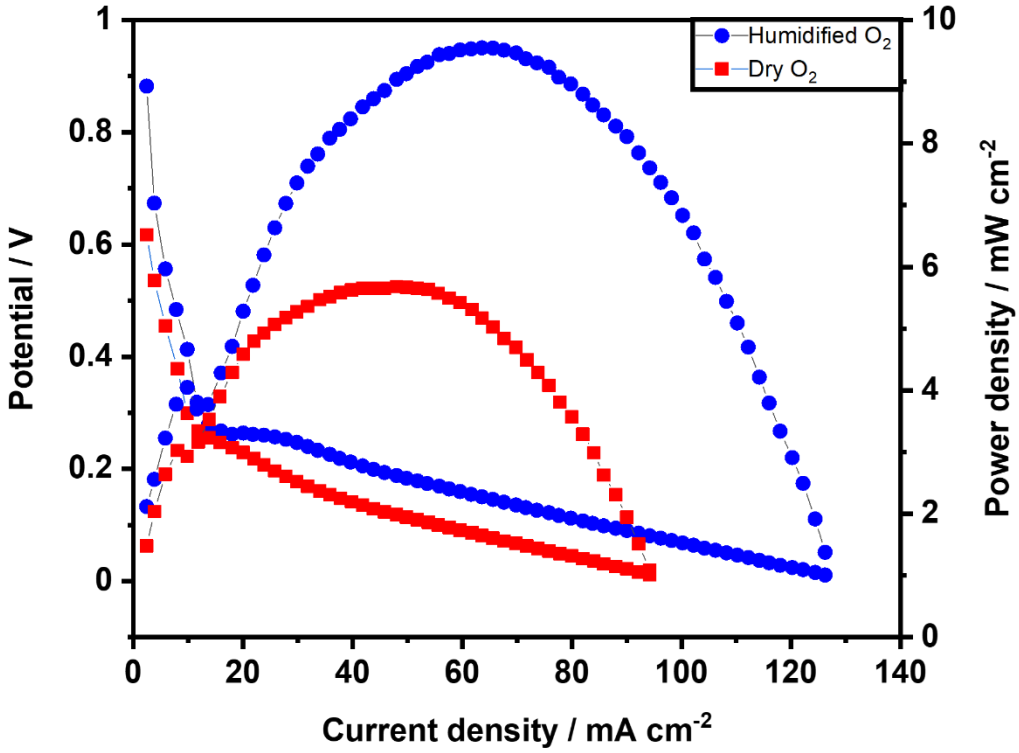

Figure 4.12 The VI plots for DAAFC using dry and humidified O_2 at 60 °C temperature using Pd/rGO/MWCNT as anode catalyst and Pt/C as cathode catalyst. Anode fuel flow rate is 1 mL/min (1 M AA + 2 M KOH) and cathode fuel 100 mL/min O_2.

We have compared the DAAFC performance using our synthesized catalysts. It can be noted from Figure 4.13a that Pd/rGO/MWCNT anode catalyst showed higher performance (9.54 mW/cm^2 maximum power density and 126 mA/cm^2 maximum current density) than the Pd/rGO catalyst (9.19 mW/cm^2 maximum power density and 120.2

mA/cm^2 maximum current density). The OCV value of Pd/rGO/MWCNT is +0.88 V and for Pd/rGO OCV is +0.79 V. However, rGO/MWCNT catalyst does not have the DAAFC performance (Figure 4.13b).

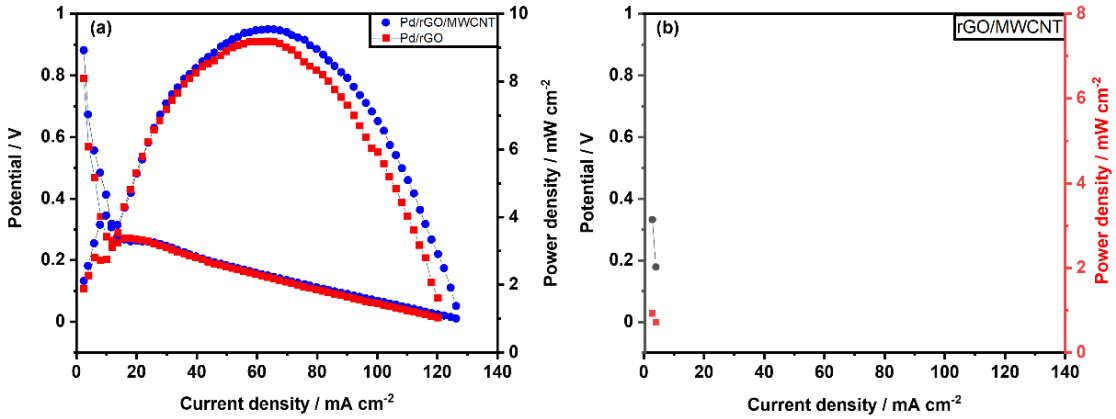

Figure 4.13 The VI plots for DAAFC using dry and humidified O_2 at 60 °C temperature using Pd/rGO/MWCNT as anode catalyst and Pt/C as cathode catalyst. Anode fuel flow rate is 1 mL/min (1 M AA + 2 M KOH) and cathode fuel 100 mL/min O_2.

Table 4.3 showed the comparison data of DAAFC using different anode catalysts. However, the performance of the Pd/rGO/MWCNT catalyst showed lower performance. The lower BET surface area of the Pd/rGO/MWCNT system (153.7 $m^2\ g^{-1}$) compared to the commercial Vulcan XC-72 carbon (227.7 $\pm$3.570 $m^2\ g^{-1}$) [61], used in the previous study, could be one of the reasons for the lower performance.

Table 4.3 Direct alkaline ascorbic acid fuel cell performance using different anode catalyst

Anode	Anode fuel	Cathode	Cathode fuel	Membrane	Power density (mW/ cm^2)	Current density (mA/ cm^2)	Ref.
PdCu/C	1M AA + 1M KOH	Pt/C	O_2	Tokuyama A201 AEM	89	~560	[62]
Pd/C	1M AA + 1M KOH	Pt/C	O_2	Tokuyama A201 AEM	73	497	[15]
Pd/rGO/ MWCNT	1M AA + 2M KOH	Pt/C	O_2	Tokuyama A201 AEM	9.54	~126	This work

Note: AEM= anion exchange membrane. In all cases, fuel cell testing was conducted at 60 °C.

4.5 Conclusion

We successfully incorporated Pd NPs into the rGO and MWCNT hybrid nanocomposite for the application of AA electrooxidation. We prepared three modified electrodes using three synthesized catalysts. Compared to the other two modified electrodes (Pd/rGO/GCE and rGO/MWCNT/GCE), Pd/rGO/MWCNT/GCE exhibits quite high catalytic performance for AA oxidation. The Pd/rGO/MWCNT/GCE also shows good stability to AA electrooxidation than other prepared electrodes. The simplest synthetic method for the preparation of Pd NPs, rGO, and MWCNT hybrid nanocomposite with good stability is used as anode material in the fuel cell application. We have optimized the DAAFC performance and found that Pd/rGO/MWCNT anode catalyst could generate 9.54 mW/cm^2 power using Pt/C on the cathode side. The fuel cell testing result entitled us to the potential use of DAAFC in near future for the alternative environment-friendly energy harvesting system.

References

[1] E. Mourad, L. Coustan, P. Lannelongue, D. Zigah, A. Mehdi, A. Vioux, S.A. Freunberger, F. Favier, O. Fontaine, Biredox ionic liquids with solid-like redox density in the liquid state for high-energy supercapacitors, Nat. Mater. 16 (2017) 446–453. https://doi.org/10.1038/nmat4808.

[2] N. Mahne, B. Schafzahl, C. Leypold, M. Leypold, S. Grumm, A. Leitgeb, G.A. Strohmeier, M. Wilkening, O. Fontaine, D. Kramer, C. Slugovc, S.M. Borisov, S.A. Freunberger, Singlet oxygen generation as a major cause for parasitic reactions during cycling of aprotic lithium-oxygen batteries, Nat. Energy. 2 (2017) 1–9. https://doi.org/10.1038/nenergy.2017.36.

[3] Y. Nabil, S. Cavaliere, I.A. Harkness, J.D.B. Sharman, D.J. Jones, J. Rozière, Novel niobium carbide/carbon porous nanotube electrocatalyst supports for proton exchange membrane fuel cell cathodes, J. Power Sources. 363 (2017) 20–26. https://doi.org/10.1016/j.jpowsour.2017.07.058.

[4] S. Nanda, R. Rana, Y. Zheng, J.A. Kozinski, A.K. Dalai, Insights on pathways for hydrogen generation from ethanol, Sustain. Energy Fuels. 1 (2017) 1232–1245. https://doi.org/10.1039/C7SE00212B.

[5] M. del Cueto, P. Ocón, J.M.L. Poyato, Comparative Study of Oxygen Reduction Reaction Mechanism on Nitrogen-, Phosphorus-, and Boron-Doped Graphene Surfaces for Fuel Cell Applications, J. Phys. Chem. C. 119 (2015) 2004–2009. https://doi.org/10.1021/jp512588r.

[6] S. Goodwin, D.A. Walsh, Closed Bipolar Electrodes for Spatial Separation of H2 and O2 Evolution during Water Electrolysis and the Development of High-Voltage Fuel Cells, ACS Appl. Mater. Interfaces. 9 (2017) 23654–23661.

https://doi.org/10.1021/acsami.7b04226.

[7] K. Dhara, R.M. Debiprosad, Review on nanomaterials-enabled electrochemical sensors for ascorbic acid detection, Anal. Biochem. 586 (2019) 113415. https://doi.org/10.1016/j.ab.2019.113415.

[8] A. Mahajan, S. Banik, D. Majumdar, S.K. Bhattacharya, Anodic Oxidation of Butan-1-ol on Reduced Graphene Oxide-Supported Pd–Ag Nanoalloy for Fuel Cell Application, ACS Omega. 4 (2019) 4658–4670. https://doi.org/10.1021/acsomega.8b03561.

[9] Z. Tao, Q. Zhang, X. Xi, G. Hou, L. Bi, A strategy of tailoring stable electrolyte material for high performance proton-conducting solid oxide fuel cells (SOFCs), Electrochem. Commun. 72 (2016) 19–22. https://doi.org/10.1016/j.elecom.2016.08.019.

[10] N. Fujiwara, S. Yamazaki, Z. Siroma, T. Ioroi, K. Yasuda, Direct oxidation of l-ascorbic acid on a carbon black electrode in acidic media and polymer electrolyte fuel cells, Electrochem. Commun. 8 (2006) 720–724. https://doi.org/10.1016/j.elecom.2006.02.021.

[11] D. Sebastián, A. Serov, I. Matanovic, K. Artyushkova, P. Atanassov, A.S. Aricò, V. Baglio, Insights on the extraordinary tolerance to alcohols of Fe-N-C cathode catalysts in highly performing direct alcohol fuel cells, Nano Energy. 34 (2017) 195–204. https://doi.org/10.1016/j.nanoen.2017.02.039.

[12] D. Sebastián, A. Serov, K. Artyushkova, J. Gordon, P. Atanassov, A.S. Aricò, V. Baglio, High Performance and Cost-Effective Direct Methanol Fuel Cells: Fe-N-C Methanol-Tolerant Oxygen Reduction Reaction Catalysts, ChemSusChem. 9 (2016) 1986–1995. https://doi.org/10.1002/cssc.201600583.

[13] D.K. Ross, Hydrogen storage: The major technological barrier to the development of hydrogen fuel cell cars, Vacuum. 80 (2006) 1084–1089. https://doi.org/10.1016/j.vacuum.2006.03.030.

[14] Z.M. Bhat, R. Thimmappa, M.C. Devendrachari, S.P. Shafi, S. Aralekallu, A.R. Kottaichamy, M. Gautam, M.O. Thotiyl, A Direct Alcohol Fuel Cell Driven by an Outer Sphere Positive Electrode, J. Phys. Chem. Lett. 8 (2017) 3523–3529. https://doi.org/10.1021/acs.jpclett.7b01418.

[15] O. Muneeb, E. Do, T. Tran, D. Boyd, M. Huynh, G. Ghosn, J.L. Haan, A direct ascorbate fuel cell with an anion exchange membrane, J. Power Sources. 351 (2017) 74–78. https://doi.org/10.1016/j.jpowsour.2017.03.068.

[16] B.R. Sathe, A scalable and facile synthesis of carbon nanospheres as a metal free electrocatalyst for oxidation of l -ascorbic acid: Alternate fuel for direct oxidation fuel cells, J. Electroanal. Chem. 799 (2017) 609–616. https://doi.org/10.1016/j.jelechem.2017.03.049.

[17] M. Choun, H.J. Lee, J. Lee, Positively charged carbon electrocatalyst for enhanced power performance of L-ascorbic acid fuel cells, J. Energy Chem. 25 (2016) 793–797. https://doi.org/10.1016/j.jechem.2016.05.006.

[18] S. Uhm, J. Choi, S.T. Chung, J. Lee, Electrochemically oxidized carbon anode in direct l-ascorbic acid fuel cells, Electrochim. Acta. 53 (2007) 1731–1736. https://doi.org/10.1016/j.electacta.2007.08.034.

[19] N. Fujiwara, S. Yamazaki, Z. Siroma, T. Ioroi, K. Yasuda, l-Ascorbic acid as an alternative fuel for direct oxidation fuel cells, J. Power Sources. 167 (2007) 32–38. https://doi.org/10.1016/j.jpowsour.2007.02.023.

[20] M.M. Hasan, R.H. Rakib, M.A. Hasnat, Y. Nagao, Electroless Deposition of

Silver Dendrite Nanostructure onto Glassy Carbon Electrode and Its Electrocatalytic Activity for Ascorbic Acid Oxidation, ACS Appl. Energy Mater. 3 (2020) 2907–2915. https://doi.org/10.1021/acsaem.9b02513.

[21] S. Kuss, R.G. Compton, Electrocatalytic detection of ascorbic acid using N,N,N',N'-tetramethyl-para-phenylene-diamine (TMPD) mediated oxidation at unmodified gold electrodes; reaction mechanism and analytical application, Electrochim. Acta. 242 (2017) 19–24. https://doi.org/10.1016/j.electacta.2017.05.003.

[22] Y. Zhao, J. Qin, H. Xu, S. Gao, T. Jiang, S. Zhang, J. Jin, Gold nanorods decorated with graphene oxide and multi-walled carbon nanotubes for trace level voltammetric determination of ascorbic acid, Microchim. Acta. 186 (2019) 17. https://doi.org/10.1007/s00604-018-3138-2.

[23] C.-L. Sun, C.-T. Chang, H.-H. Lee, J. Zhou, J. Wang, T.-K. Sham, W.-F. Pong, Microwave-Assisted Synthesis of a Core–Shell MWCNT/GONR Heterostructure for the Electrochemical Detection of Ascorbic Acid, Dopamine, and Uric Acid, ACS Nano. 5 (2011) 7788–7795. https://doi.org/10.1021/nn2015908.

[24] J.N. Tiwari, V. Vij, K.C. Kemp, K.S. Kim, Engineered carbon-nanomaterial-based electrochemical sensors for biomolecules, ACS Nano. 10 (2016) 46–80. https://doi.org/10.1021/acsnano.5b05690.

[25] M.A. Zahed, S.C. Barman, R.M. Toyabur, M. Sharifuzzaman, X. Xuan, J. Nah, J.Y. Park, Ex Situ Hybridized Hexagonal Cobalt Oxide Nanosheets and RGO@MWCNT Based Nanocomposite for Ultra-Selective Electrochemical Detection of Ascorbic Acid, Dopamine, and Uric Acid, J. Electrochem. Soc. 166 (2019) B304–B311. https://doi.org/10.1149/2.0131906jes.

[26] H. Bagheri, A. Hajian, M. Rezaei, A. Shirzadmehr, Composite of Cu metal nanoparticles-multiwall carbon nanotubes-reduced graphene oxide as a novel and high performance platform of the electrochemical sensor for simultaneous determination of nitrite and nitrate, J. Hazard. Mater. 324 (2017) 762–772. https://doi.org/10.1016/j.jhazmat.2016.11.055.

[27] B. Gadgil, P. Damlin, C. Kvarnström, Graphene vs. reduced graphene oxide: A comparative study of graphene-based nanoplatforms on electrochromic switching kinetics, Carbon N. Y. 96 (2016) 377–381. https://doi.org/10.1016/j.carbon.2015.09.065.

[28] S. Kellici, J. Acord, J. Ball, H.S. Reehal, D. Morgan, B. Saha, A single rapid route for the synthesis of reduced graphene oxide with antibacterial activities, RSC Adv. 4 (2014) 14858. https://doi.org/10.1039/c3ra47573e.

[29] H. Xu, Q. Li, L. Wang, Y. He, J. Shi, B. Tang, C. Fan, Nanoscale optical probes for cellular imaging, Chem. Soc. Rev. 43 (2014) 2650–2661. https://doi.org/10.1039/c3cs60309a.

[30] S. Tourani, A.M. Rashidi, A.A. Safekordi, H.R. Aghabozorg, F. Khorasheh, Synthesis of Reduced Graphene Oxide-Carbon Nanotubes (rGO–CNT) Composite and Its Use As a Novel Catalyst Support for Hydro-Purification of Crude Terephthalic Acid, Ind. Eng. Chem. Res. 54 (2015) 7591–7603. https://doi.org/10.1021/acs.iecr.5b01574.

[31] H. Ye, Y. Li, J. Chen, J. Sheng, X.Z. Fu, R. Sun, C.P. Wong, PdCu alloy nanoparticles supported on reduced graphene oxide for electrocatalytic oxidation of methanol, J. Mater. Sci. 53 (2018) 15871–15881. https://doi.org/10.1007/s10853-018-2759-5.

[32] J. Jiang, X. Du, Sensitive electrochemical sensors for simultaneous determination of ascorbic acid, dopamine, and uric acid based on Au@Pd-reduced graphene oxide nanocomposites, Nanoscale. 6 (2014) 11303–11309. https://doi.org/10.1039/C4NR01774A.

[33] M. Abu Zahed, S.C. Barman, M. Sharifuzzaman, X. Xuan, J.S. Nah, J.Y. Park, Ex Situ Synthesis of Hexagonal NiO Nanosheets and Carboxyl-Terminated Reduced Graphene Oxide Nanocomposite for Non-Enzymatic Electrochemical Detection of H2O2 and Ascorbic Acid, J. Electrochem. Soc. 165 (2018) B840–B847. https://doi.org/10.1149/2.0621816jes.

[34] Z. Li, X. Dai, K. Du, Y. Ma, M. Liu, H. Sun, X. Ma, X. Zhang, Reduced Graphene Oxide/O-MWCNT Hybrids Functionalized with p-Phenylenediamine as High-Performance MoS2 Electrocatalyst Support for Hydrogen Evolution Reaction, J. Phys. Chem. C. 120 (2016) 1478–1487. https://doi.org/10.1021/acs.jpcc.5b09523.

[35] D.E. Bayraktepe, Z. Yazan, M. Önal, Sensitive and cost effective disposable composite electrode based on graphite, nano-smectite and multiwall carbon nanotubes for the simultaneous trace level detection of ascorbic acid and acetylsalicylic acid in pharmaceuticals, Talanta. 203 (2019) 131–139. https://doi.org/10.1016/j.talanta.2019.05.063.

[36] X. Jiang, Y. Wu, X. Mao, X. Cui, L. Zhu, Amperometric glucose biosensor based on integration of glucose oxidase with platinum nanoparticles/ordered mesoporous carbon nanocomposite, Sensors Actuators B Chem. 153 (2011) 158–163. https://doi.org/10.1016/j.snb.2010.10.023.

[37] A. Bin Yousaf, M. Imran, A. Zeb, X. Xie, K. Liang, X. Zhou, C.Z. Yuan, A.W. Xu, Synergistic effect of graphene and multi-walled carbon nanotubes composite

supported Pd nanocubes on enhancing catalytic activity for electro-oxidation of formic acid, Catal. Sci. Technol. 6 (2016) 4794–4801. https://doi.org/10.1039/C5CY02217G.

[38] J. Hu, Z. Zhao, J. Zhang, G. Li, P. Li, W. Zhang, K. Lian, Synthesis of palladium nanoparticle modified reduced graphene oxide and multi-walled carbon nanotube hybrid structures for electrochemical applications, Appl. Surf. Sci. 396 (2017) 523–529. https://doi.org/10.1016/j.apsusc.2016.10.187.

[39] T. Sun, Z. Zhang, J. Xiao, C. Chen, F. Xiao, S. Wang, Y. Liu, Facile and Green Synthesis of Palladium Nanoparticles-Graphene-Carbon Nanotube Material with High Catalytic Activity, Sci. Rep. 3 (2013) 2527. https://doi.org/10.1038/srep02527.

[40] D. Larcher, J.-M. Tarascon, Towards greener and more sustainable batteries for electrical energy storage, Nat. Chem. 7 (2015) 19–29. https://doi.org/10.1038/nchem.2085.

[41] I.E.L. Stephens, J. Rossmeisl, I. Chorkendorff, Toward sustainable fuel cells, Science (80-.). 354 (2016) 1378–1379. https://doi.org/10.1126/science.aal3303.

[42] H. Huang, S. Yang, R. Vajtai, X. Wang, P.M. Ajayan, Pt-Decorated 3D Architectures Built from Graphene and Graphitic Carbon Nitride Nanosheets as Efficient Methanol Oxidation Catalysts, Adv. Mater. 26 (2014) 5160–5165. https://doi.org/10.1002/adma.201401877.

[43] F. Yang, J. Wang, Y. Cao, L. Zhang, X. Zhang, A highly sensitive ascorbic acid sensor based on carbon-supported CoPd nanoparticles, Sensors Actuators B Chem. 205 (2014) 20–25. https://doi.org/10.1016/j.snb.2014.08.050.

[44] G. Wu, Y. Wu, X. Liu, M. Rong, X. Chen, X. Chen, An electrochemical ascorbic

acid sensor based on palladium nanoparticles supported on graphene oxide, Anal. Chim. Acta. 745 (2012) 33–37. https://doi.org/10.1016/j.aca.2012.07.034.

[45] X. Zhang, Y. Cao, S. Yu, F. Yang, P. Xi, An electrochemical biosensor for ascorbic acid based on carbon-supported PdNinanoparticles, Biosens. Bioelectron. 44 (2013) 183–190. https://doi.org/10.1016/j.bios.2013.01.020.

[46] A. Uzunoglu, D.A. Kose, E. Gokmese, F. Gokmese, Electrochemical Glucose Detection Using PdAg Nanoparticles Anchored on rGO/MWCNT Nanohybrids, J. Clust. Sci. 31 (2020) 231–239. https://doi.org/10.1007/s10876-019-01641-5.

[47] D. Rajesh, P. Indra Neel, A. Pandurangan, C. Mahendiran, Pd-NiO decorated multiwalled carbon nanotubes supported on reduced graphene oxide as an efficient electrocatalyst for ethanol oxidation in alkaline medium, Appl. Surf. Sci. 442 (2018) 787–796. https://doi.org/10.1016/j.apsusc.2018.02.174.

[48] O. Muneeb, I. Chino, A. Saenz, J.L. Haan, An ascorbate fuel cell with carbon black nanoparticles as anode and cathode, J. Power Sources. 413 (2019) 216–221. https://doi.org/10.1016/j.jpowsour.2018.12.042.

[49] Y. Li, X. Lu, H. Wang, C. Xie, G. Yang, C. Niu, Growth of Ultrafine SnO 2 Nanoparticles within Multiwall Carbon Nanotube Networks: Non-Solution Synthesis and Excellent Electrochemical Properties as Anodes for Lithium Ion Batteries, Electrochim. Acta. 178 (2015) 778–785. https://doi.org/10.1016/j.electacta.2015.08.078.

[50] Y. She, Z. Lu, W. Fan, S. Jewell, M.K.H. Leung, Facile preparation of PdNi/rGO and its electrocatalytic performance towards formic acid oxidation, J. Mater. Chem. A. 2 (2014) 3894. https://doi.org/10.1039/c3ta14546h.

[51] K.V. Sankar, R.K. Selvan, R.H. Vignesh, Y.S. Lee, Nitrogen-doped reduced

graphene oxide and aniline based redox additive electrolyte for a flexible supercapacitor, RSC Adv. 6 (2016) 67898–67909. https://doi.org/10.1039/C6RA11521G.

[52] M.M. Hasan, Y. Nagao, Christmas-Tree-Shaped Palladium Nanostructures Decorated on Glassy Carbon Electrode for Ascorbic Acid Oxidation in Alkaline Condition, ChemistrySelect. 6 (2021) 5885–5892. https://doi.org/10.1002/slct.202100974.

[53] C. Lu, W. Guan, T.K.A. Hoang, Y. Li, T.N.L. Doan, H. Zhao, A novel synthetic strategy for pd3sn nanoparticles loaded reduced graphene oxide as electrocatalyst for the ethanol-tolerant oxygen reduction reaction, Int. J. Electrochem. Sci. 10 (2015) 5077–5085.

[54] C. Luhrs, M. Moberg, A. Maxson, L. Brewer, S. Menon, IF-WS2/Nanostructured Carbon Hybrids Generation and Their Characterization, Inorganics. 2 (2014) 211–232. https://doi.org/10.3390/inorganics2020211.

[55] F. Du, J. Yuan, M. Zhang, J. Li, Z. Zhou, Z. Li, M. Cao, J. Chen, L. Zhang, X. Liu, A. Gong, W. Xu, Q. Shao, Nitrogen-doped carbon dots with heterogeneous multi-layered structures, RSC Adv. 4 (2014) 37536. https://doi.org/10.1039/C4RA06818A.

[56] N. Jha, P. Ramesh, E. Bekyarova, M.E. Itkis, R.C. Haddon, High Energy Density Supercapacitor Based on a Hybrid Carbon Nanotube-Reduced Graphite Oxide Architecture, Adv. Energy Mater. 2 (2012) 438–444. https://doi.org/10.1002/aenm.201100697.

[57] P.K. Sahoo, B. Panigrahy, D. Li, D. Bahadur, Magnetic behavior of reduced graphene oxide/metal nanocomposites, J. Appl. Phys. 113 (2013) 17B525.

https://doi.org/10.1063/1.4799150.

[58] M.A. Hasnat, M.M. Hasan, N. Tanjila, M.M. Alam, M.M. Rahman, pH dependent kinetic insights of electrocatalytic arsenite oxidation reactions at Pt surface, Electrochim. Acta. 225 (2017) 105–113. https://doi.org/10.1016/j.electacta.2016.12.055.

[59] D.F. Silva, A.O. Neto, E.S. Pino, M. Linardi, E. V. Spinacé, Preparation of PtSn/C electrocatalysts using electron beam irradiation, in: Stud. Surf. Sci. Catal., 2010: pp. 555–558. https://doi.org/10.1016/S0167-2991(10)75107-7.

[60] A.A. Rafati, A. Afraz, A. Hajian, P. Assari, Simultaneous determination of ascorbic acid, dopamine, and uric acid using a carbon paste electrode modified with multiwalled carbon nanotubes, ionic liquid, and palladium nanoparticles, Microchim. Acta. 181 (2014) 1999–2008. https://doi.org/10.1007/s00604-014-1293-7.

[61] T. Soboleva, X. Zhao, K. Malek, Z. Xie, T. Navessin, S. Holdcroft, On the Micro-, Meso-, and Macroporous Structures of Polymer Electrolyte Membrane Fuel Cell Catalyst Layers, ACS Appl. Mater. Interfaces. 2 (2010) 375–384. https://doi.org/10.1021/am900600y.

[62] O. Muneeb, E. Do, D. Boyd, J. Perez, J.L. Haan, PdCu/C anode catalysts for the alkaline ascorbate fuel cell, Appl. Energy. 235 (2019) 473–479. https://doi.org/10.1016/j.apenergy.2018.10.073.

Chapter 5

General Conclusion

5.1 Conclusion

We have developed metal catalysts for AA electrooxidation. The improvement of AA electrooxidation leads to the construction of the environment-friendly AA-based fuel cell system (DAAFC). Therefore, there is a significant deal of relevance in this sector in designing and developing sustainable electrocatalytic materials. Because of this, novel techniques have been developed to design and manufacture highly active AA electrooxidation catalysts to establish the DAAFC system.

In summary, all these chapters were focused on the same goal: to develop a simple and cost-effective process for creating various metal catalysts to find suitable anode catalysts for the DAAFC. Firstly, Chapter 1 gives an overview of the AA and different hierarchical metal-based electrocatalysts. It also provides an outline of the mechanism for AA electrooxidation, catalysts synthesis process, and potential applications for DAAFC systems. A comprehensive summary of the literature is provided, with a focus on the evolution of techniques for designing and constructing metal-based electrocatalysts and various fuel cell systems. This chapter provides a discussion of possible electrocatalyst design methods for achieving a) large surface area, b) strong electrocatalytic activity, c) high stability during AA electrooxidation, and d) metal nanoparticles (NPs) integrated carbon-based catalyst for DAAFC.

Before DAAFC development, we have explored the detailed reaction mechanisms for the electron transfer process during AA electrooxidation by hierarchical

silver dendrite nanostructures in chapter 2. The dendrite nanostructures were deposited as a full growth state having primary and secondary branches with leaves on the glassy carbon electrode (GCE) by a simple one-step electroless deposition technique (Figure 5.1). The silver dendrite nanostructures showed high electrocatalytic activity as well as good stability for AA electrooxidation. The kinetic study revealed the dependency of electrons transfer on the scan rate. The kinetic study helps us to understand more about the electrons transfer process.

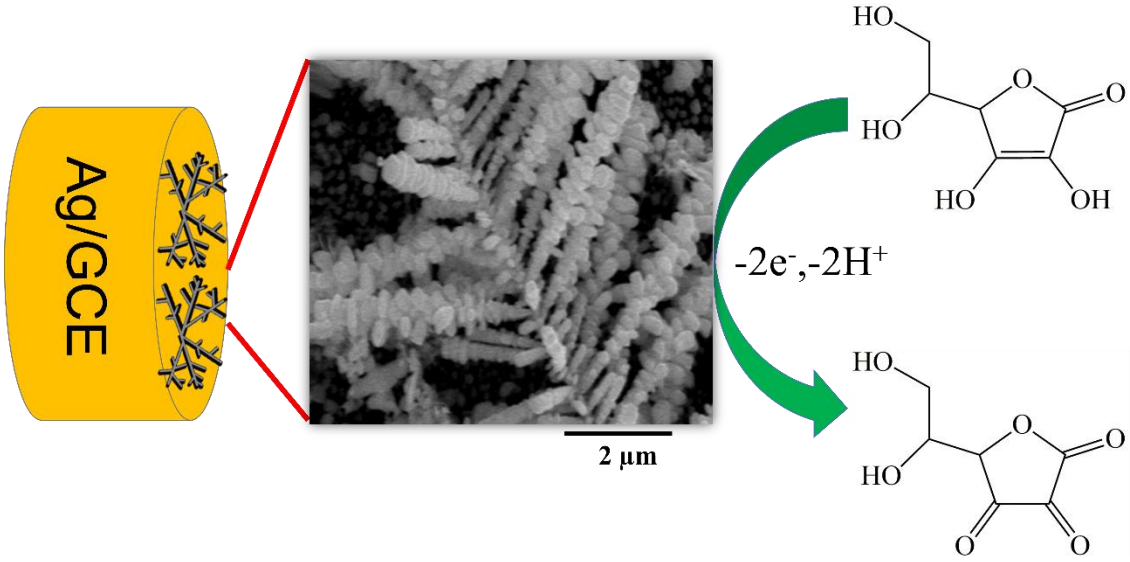

Figure 5.1 Silver dendrite nanostructures for ascorbic acid electrooxidation.

Chapter 3 described the excellent catalytical activity of unique Christmas-Tree-Shaped Pd nanostructures for AA electrooxidation in the alkaline medium. The hierarchical Pd nanostructures were deposited on the GCE by a one-step electrodeposition technique without using any additives. This chapter showed the potential use of Pd anode catalyst for DAAFC. The Pd metal showed high sensitivity and excellent electrocatalytic activity for AA electrooxidation in the alkaline solution. This strategy entails developing and implementing a simple technique that provides Pd-based

materials with very high catalytic activity for AA electrooxidation (Figure 5.2). The selectivity of Pd metals for the AA electrooxidation makes it a potential candidate for the anode catalyst for the DAAFC system, which has been discussed in chapter 4.

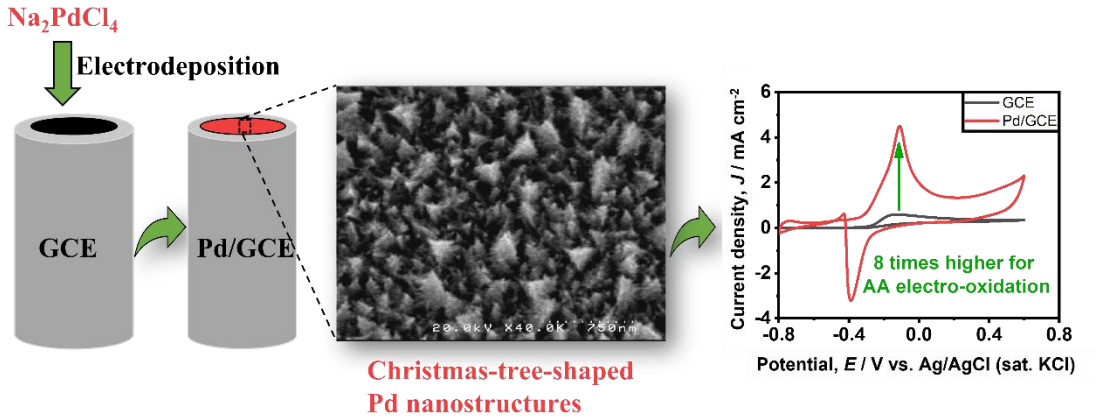

Figure 5.2 Christmas-Tree-Shaped Pd nanostructures showed excellent ascorbic acid electrocatalytic activity in alkaline solution.

We have further developed a DAAFC system using Pd nanoparticles incorporated rGO/MWCNT carbon materials for the first time. Chapter 4 describes the power generation of a single cell DAAFC system using Pd NPs incorporated rGO and MWCNT (Pd/rGO/MWCNT) system. The Pd/rGO/MWCNT catalyst was synthesized by a simple chemical reduction process where small Pd NPs (9 nm) were homogeneously distributed into the rGO and MWCNT system. The catalyst showed very high electrocatalytic activity for AA electrooxidation in alkaline solution (Figure 5.3). The maximum power generation was 9.54 mW/cm^2 at 60 °C by a single cell DAAFC system. This indicates the possible use of an environment-friendly DAAFC system for energy harvesting. This leads to one step forward in achieving sustainable development goals.

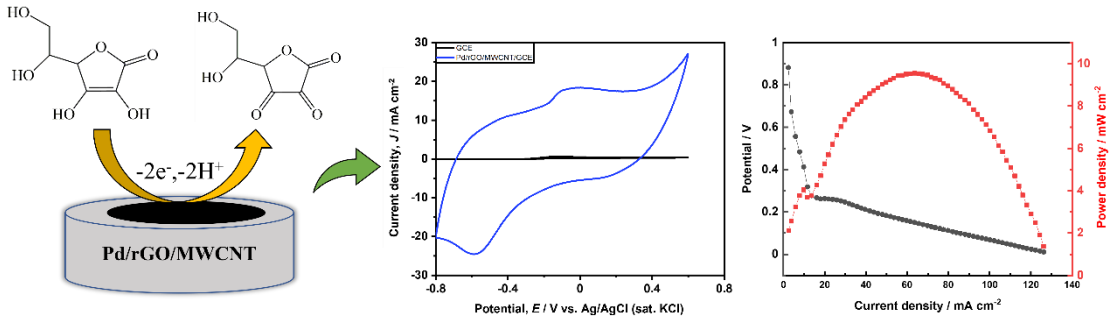

Figure 5.3 Pd/rGO/MWCNT showed very high ascorbic acid electrocatalytic activity in alkaline solution, and the voltage-current plots for DAAFC using Pd/rGO/MWCNT anode catalyst.

5.2 Future Scope

The current study has demonstrated different metal electrocatalysts preparation for AA electrooxidation. Based on the current investigations, the following are probable areas for improvement.

1. Synthesis of alloy materials for the further improvement of AA electrooxidation. For the development of the high catalytic active catalyst, appropriate non-precious low-cost metals such as Cu, Ag, etc. might be combined with Pd metal.
2. The different forms of hierarchical Pd metal catalysts like Pd hollow, Pd nanothorns, etc. could be synthesized and applied for AA electrooxidation.

Acknowledgments

I would like to convey my heartfelt thanks to Associate Professor Yuki Nagao, my Ph.D. supervisor, for his insightful advice, competent supervision, encouraging words, and unwavering support while I pursued my doctorate studies.

I also deeply acknowledge Professor Noriyoshi Matsumi for providing me the opportunity to proceed with my minor research project under his supervision. I am also grateful to Senior Lecturer Rajashekar Badam of Matsumi lab for his support during my minor research. His suggestive encouragement and discussion helped me to widen my knowledge. I have also grateful to Mr. Asai for his kind supports during my minor research.

I express my thanks to Professor Tatsuo Kaneko for being my second supervisor. I would like to thank Associate Professor Shun Nishimura and Dr. Le Dinh Son for supporting the measurement of atomic absorption spectrometry (AAS). I express my sincere gratitude to Professor Kazuaki Matsumura for supporting differential scanning calorimetry (DSC) measurement. I also like to thank Dr. Zhongping Li for supporting Brunauer-Emmett-Teller (BET) measurement. I would like to thank Professor Mitsuru Higa, Assistant Professor Nobutaka Endo, and Dr. Yuriko Kakihana from Yamaguchi University for the fuel cell measurement.

I also deeply express my sincere gratitude to all referees including Professor Tsuyohiko Fujigaya (Kyushu University), Professor Noriyoshi Matsumi (JAIST), Professor Tatsuo Kaneko (JAIST), Associate Professor Eijiro Miyako (JAIST) for taking the time to review my thesis and for thoughtful comments and suggestions on the improvement of the quality of this dissertation.

I would like to thank the former and present students of Nagao laboratory for their kind support and beneficial discussion with me.

Finally, I profoundly appreciate the support, sacrifice, and encouragement from my family members, and all of my friends.

Md Mahmudul Hasan

School of Materials Science

Japan Advanced Institute of Science and Technology

March 2022

Achievements

Journals:

Main publications:

1. **Md. Mahmudul Hasan**, Riad Hussain Rakib, Mohammad Abul Hasnat, Yuki Nagao, *Electroless deposition of silver dendrite nanostructure onto glassy carbon electrode and its electrocatalytic activity for ascorbic acid oxidation,* ACS Applied Energy Materials, 2020, 3, 2907-2915.
2. **Md. Mahmudul Hasan**, Yuki Nagao, *Christmas-tree-shaped palladium nanostructures decorated on glassy carbon electrode for ascorbic acid oxidation in alkaline condition,* ChemistrySelect, 2021, 6, 5885–5892.
3. **Md. Mahmudul Hasan**, Nobutaka Endo, Yuriko Kakihana, Mitsuru Higa, Zhongping Li, Yuki Nagao, *Palladium Nanoparticles Decorated on Reduced Graphene Oxide and Multiwall Carbon Nanotubes Hybrid nanocomposite for Alkaline Ascorbic Acid Fuel Cell Application* (In Preparation).

Other publications:

1. Md. Fahamidul Islam, Md. Tarikul Islam, **Md. Mahmudul Hasan**, Mohammed M. Rahman, Yuki Nagao, Mohammad A. Hasnat, *Facile fabrication of GCE/Nafion/Ni*

composite, a robust platform to detect hydrogen peroxide in the basic medium via oxidation reaction, Talanta, 2022, 240, 123202.

2. A.F. Fuzlin, M.A. Saadiah, **Md. M. Hasan**, Y. Nagao, I.I. Misnon and A.S. Samsudin, *Involvement of ethylene carbonate on the enhancement H+ carriers in structural and ionic conduction performance on alginate bio-based polymer electrolytes*, International Journal of Hydrogen Energy, 2022, 47, 7846-7860.
3. Lipeng Zhai, Yuze Yao, Baiwei Ma, **Md. Mahmudul Hasan**, Yuxi Han, Liwei Mi, Yuki Nagao, Zhongping Li, *Accumulation of Sulfonic Acid Groups Anchored in Covalent Organic Frameworks as an Intrinsic Proton-Conducting Electrolyte*, Macromolecular Rapid Communications, 2021, 2100590.
4. Anim Dutta, **Md. Mahmudul Hasan**, Md. Rezwan Miah, Yuki Nagao, Mohammad A. Hasnat, *Efficient sensing of hydrogen peroxide via electrocatalytic oxidation reactions using polycrystalline Au electrode modified with controlled thiol group immobilization*, Electrochimica Acta, 2021, 395, 139217.
5. Yuwei Zhang, Chunzhi Li, Zhaohan Liu, Yuze Yao, **Md. Mahmudul Hasan**, Qianyu Liu, Jieqiong Wan, Zhongping Li, He Li, and Yuki Nagao, *Intrinsic proton conduction in 2D sulfonated covalent organic framework through the post-synthetic strategy*, CrystEngComm, 2021, 23, 6234-6238.

6. Md Fazle Shabik, **Md. Mahmudul Hasan**, Khalid A Alamry, Mohammed M. Rahman, Yuki Nagao, Mohammad A. Hasnat, *Electrocatalytic oxidation of ammonia in the neutral medium using Cu_2O.CuO film immobilized on glassy carbon surface,* Journal of Electroanalytical Chemistry, 2021, 897, 115592.
7. Md Tarikul Islam, **Md. Mahmudul Hasan**, Md Fazle Shabik, Fahadul Islam, Yuki Nagao, Mohammad A Hasnat, *Electroless deposition of gold nanoparticles on a glassy carbon surface to attain methylene blue degradation via oxygen reduction reactions,* Electrochimica Acta, 2020, 360, 136966.
8. Zhongping Li, He Li, Dongjin Wang, Athchaya Suwansoontorn, Gang Du, Zhaohan Liu, **Md. Mahmudul Hasan**, Yuki Nagao, *A simple and cost-effective synthesis of ionic porous organic polymers with excellent porosity for high iodine capture,* Polymer, 2020, 204, 122796.
9. Zhongping Li, Zhaohan Liu, He Li, **Md. Mahmudul Hasan**, Athchaya Suwansoontorn, Gang Du, Dongjin Wang, Yuwei Zhang, Yuki Nagao, *Sulfonated Triazine-Based Porous Organic Polymers for Excellent Proton Conductivity,* ACS Applied Polymer Materials, 2020, 2, 3267-3273.
10. Zhongping Li, Yuze Yao, Dongjin Wang, **Md. Mahmudul Hasan**, Athchaya Suwansoontorn, He Li, Gang Du, Zhaohan Liu, Yuki Nagao, *Simple and universal*

synthesis of sulfonated porous organic polymers with high proton conductivity, Materials Chemistry Frontiers, 2020, 4, 2339-2345.

Conferences:

1. **Md. Mahmudul Hasan**, Yuki Nagao, *Hierarchical palladium nanostructures for ascorbic acid electrooxidation in alkaline condition*, Hokuriku CSJ conference, JAIST, Nomi, Ishikawa, Japan, 12 November 2021. (Poster Presentation)
2. **Md. Mahmudul Hasan**, Yuki Nagao, *Hierarchical metal catalysts for ascorbic acid electrooxidation*, Excellent Core Student Symposium 2021, JAIST, Nomi, Ishikawa, Japan, 1 November 2021. (Poster Presentation)
3. **Md. Mahmudul Hasan**, Yuki Nagao, *Hierarchical Metal Nanostructures: Synthesis, Characterizations, and Electrocatalysis*, Nanotechnology Malaysia Annual Symposium (NANOSYM 2021), Malaysia, 11-13 October 2021. (Oral presentation)
4. **Md. Mahmudul Hasan**, Riad Hussain Rakib, Mohammad Abul Hasnat, Yuki Nagao, *Electrocatalytic oxidation of ascorbic acid by electroless deposition of silver dendrite nanostructure onto the glassy carbon electrode*, 3rd Symposium on Industrial Science and Technology (SISTEC 2021), Malaysia, 25-26 August 2021. (Oral presentation)

5. **Md. Mahmudul Hasan**, Yuki Nagao, *Electro-catalytic Oxidation of Ascorbic Acid by Ag Nanoparticles Supported on Glassy Carbon Electrode*, JAIST Japan-India Symposium on Advanced Science 2019, Nomi, Ishikawa, Japan, 7 March 2019. (Poster Presentation)
6. **Md. Mahmudul Hasan**, Yuki Nagao, *Electrochemical oxidation of effective ascorbic acid by self-deposited silver dendrite nanostructure supported onto the glassy carbon electrode*, Hokuriku CSJ conference, Kanazawa, Ishikawa, Japan, 29 November 2019. (Poster Presentation)

Awards:

1. Student's Selection Award in JAIST International Research Center for Silent Voice Sensing (Excellent Core) Student Symposium 2021, Japan (November 2021).
2. Director's Active Audience Award in JAIST International Research Center for Silent Voice Sensing (Excellent Core) Student Symposium 2021, Japan (November 2021).
3. Best Student Paper Award in NANOSYM 2021 Conference, Malaysia (October 2021).
4. Recognized as one of the most discussed articles in ChemistrySelect in the top 5% of all research outputs scored by Altmetric (July 2021).

Abstract of Minor Research

Abstract:

A novel organic/inorganic hybrid catalyst is successfully developed for oxygen evolution reaction (OER) using TiO_2 nanotube (TNT) as a template. The as-synthesized IrO_2 nanoparticles into the Poly(BIAN-Thiophene)/IrO_2 electrode exhibits quite stability in the strongly acidic solution during OER experiments. The post characterizations of the modified electrode are also investigated and found no change in the morphology as well as the oxidation state of the IrO_2. The simple cost-effective synthetic scheme could help to design alternative carbon-based catalyst for OER.

Keywords: BIAN-Thiophene, OER, TiO_2 nanotube, IrO_2.